UNIVERSITY OF SOUTHAMPTON

Effects of asymmetry on electron spin dynamics in gallium arsenide quantum wells

by

Peter Stephen Eldridge

A thesis submitted for the degree of

Doctor of Philosophy

School of Physics and Astronomy

May 2009

UNIVERSITY OF SOUTHAMPTON

ABSTRACT

FACULTY OF ENGINEERING, SCIENCE & MATHEMATICS
SCHOOL OF PHYSICS AND ASTRONOMY

Doctor of Philosophy

Effects of asymmetry on electron spin dynamics in gallium arsenide quantum wells

Peter Stephen Eldridge

This work presents optical studies of electron spin dynamics in gallium arsenide (GaAs) quantum wells, focusing on the effect of inversion asymmetric confinement potentials on spin lifetimes in quantum wells grown on (110)-oriented substrates. Inversion asymmetry in the presence of the spin-orbit interaction offers the possibility of complete control of electron spin dynamics in GaAs quantum wells. Symmetry arguments predict any inversion asymmetric two dimensional potential will reduce spin lifetimes via the Dyakonov-Perel spin relaxation mechanism. One aim of this work has been to make a comparison of the effect produced by an electric field to that from alloy engineering.

The suppression of the Dyakonov-Perel spin relaxation mechanism in (110) quantum wells makes them ideal candidates for measuring increases in spin relaxation due to asymmetry. To measure temporal spin dynamics, the time-resolved Kerr rotation technique was adapted in order to compensate for reduced rotational symmetry in the (110) crystallographic direction. An investigation into the effect of a transverse electric field on electron spin lifetimes was conducted. By combining spin lifetime with electron scattering time measurements it was possible to provide the first direct measurement of the Rashba coefficient. There is good agreement with k.p theory at low temperatures; however there is an unexplained increase with temperature.

Spin dynamics measurements were carried out on quantum wells with asymmetric alloy composition. Through the combination of electron spin lifetime and electron scattering time measurements it was shown that the effect of alloy engineering on electron spin dynamics is very small. This is consistent with theoretical predictions and highlights the importance of considering both conduction and valence band potentials for the understanding of the effect of asymmetry on electron spin dynamics in quantum wells.

Contents

List of Figures

List of Tables

Declaration of Authorship

I, Peter Stephen Eldridge, declare that this thesis titled, 'Effects of asymmetry on electron spin dynamics in gallium arsenide quantum wells' and the work presented in it are my own. I confirm that:

- This work was done wholly or mainly while in candidature for a research degree at this University.
- Where any part of this thesis has previously been submitted for a degree or any other qualification at this University or any other institution, this has been clearly stated.
- Where I have consulted the published work of others, this is always clearly attributed.
- Where I have quoted from the work of others, the source is always given. With the exception of such quotations, this thesis is entirely my own work.
- I have acknowledged all main sources of help.
- Where the thesis is based on work done by myself jointly with others, I have made clear exactly what was done by others and what I have contributed myself.

Signed: _____

Date: _____

Acknowledgements

Most importantly I would like to thank Richard Harley, for providing me with excellent supervision and guidance during my PhD. studies in Southampton. I thank Pavlos Lagoudakis for valuable discussions and exhausting squash games. For the calculations he conducted on my samples, I would like to thank Tim Liew. Finally, I would like to thank all those I worked in the lab with, especially Stefan Rohrmoser and Soontorn Chanyawadee. Without their ideas, humour and help in the lab, this PhD. thing would have been a lot less enjoyable.

This thesis is dedicated to my family.

Chapter 1

Introduction

This thesis represents a study of non-equilibrium electron spin dynamics in gallium arsenide (GaAs) quantum wells. This chapter addresses the motivation for studying spin dynamics in GaAs quantum wells and provides an overview of the subsequent chapters.

1.1 Electrons in semiconductors

Electrons are of fundamental importance in semiconductors, as it is the electronic properties of a material that determines whether it is an insulator, metal or semiconductor. As a consequence, most semiconductor physics involves studying the dynamics of electrons in response to a perturbation, normally a magnetic, electric or optical field. Many of the interesting properties of semiconductors stem from the tunability of their electronic properties through the introduction of impurity atoms. This element of control combined with advances in semiconductor physics has helped make semiconductors the backbone of technologies based on the control of electron charge motion, with silicon (Si) firmly at the heart of the electronics industry.

The advent of growth techniques capable of producing semiconductor layers a few nanometres in width renewed interest in semiconductor physics as the realisation of semiconductor devices with reduced dimensionality gave rise to new interesting physics. In addition to novel physics, the ability to confine electrons and holes to a thin layer of semiconductor, such as in quantum wells (see section 2.3), has allowed important testing and development of fundamental quantum mechanics. For when particles are confined spa-

tially in one or more dimensions on the order of the de Broglie wavelength quantum mechanical phenomena appear as momentum and consequently energy are quantised.

Semiconductor nanostructures have also found considerable applications in optoelectronics. As an excited non-equilibrium state relaxes it has to lose energy and quite often this happens through the emission of a photon. As the energy of the electrons and holes in confined structures depend upon the extent of the confinement, the wavelength of the emitted light can be easily tuned. This ability to select the wavelength of photons radiated or absorbed has been an important motivation in the development of semiconductor nanostructured devices that emit, detect and control light.

There is always an interest in overcoming foreseeable limitations in current technology and making it more versatile. Low power electronics is attractive, not just from the viewpoint of more responsible use of the Earth's limited resources, but also the power consumption of everything electronic from personal gadgets to communication systems on space probes. Many optoelectronic devices are limited by the recombination time of electrons which is typically a few nanoseconds, making high frequency operation difficult. There is also interest in polarisation control in optoelectronic devices, including light emitting diodes (LEDs) and lasers. A possible solution is to utilise spin, an intrinsic property of the electron which until recently has been ignored in most electronic and optoelectronic technology.

1.2 Electron spin

In addition to elementary charge, electrons possess an intrinsic angular momentum ($\frac{1}{2}\hbar$[1]), known as spin. The spin of an electron can have different alignments or values (-$\frac{1}{2}$ or +$\frac{1}{2}$), providing an extra degree of manipulation. This ability to align spin also means that contrary to charge information, spin information can be lost in an electron population without the recombination or diffusion of electrons.

The study of spin dynamics involves the creation of a spin alignment in either an ensemble or a single particle, then after a period of time the spin alignment of the state (or particle) is measured. By modifying the environment, for example applying an electric field, or changing the temperature,

[1] where $\hbar$ is the reduced Planck constant

the effect of the new environment on spin dynamics can be studied.

One method for producing an electron spin alignment in a semiconductor is by using light, as first demonstrated by Lampel[1] in ^{29}Si. This method, known as optical orientation, requires polarised light as it is the transfer of a photon's angular momentum to an electron spin via the spin-orbit interaction that produces the spin alignment. It is also possible to inject spin aligned electrons from a ferromagnetic source into a semiconductor, however the different conductivities of ferromagnetic metals and semiconductors makes this difficult[2]. Another option is to use magnetic semiconductors, like gallium manganese arsenide (GaMnAs), however, the highest Curie temperature observed to date is 180 K[3], ruling out room temperature operation.

Many semiconductor spintronic devices analogous to electronic and optoelectronic devices have been proposed, for example a spin field effect transistor (FET)[4], a spin amplifier[5], a spin based optical switch[6] and a spin-LED[7]. The gating of electron spin in a spin-FET potentially requires less energy than a charge based FET and could open the door to low power electronics. The spin based optical switch offers gating times of light in the region of tens of picoseconds with potential applications in high frequency optical networks. In addition, electron spin is a candidate for storing quantum information the field of quantum computation[7]. For such applications to be realised material systems have to be developed into which not only is the injection and detection of spin aligned carriers possible, but also the manipulation. Also once injected the spin information must live long enough so that it is still present when the device executes. It would be practical for spintronic devices to work at room temperature, currently making silicon and gallium arsenide more favourable materials than GaMnAs for mass market spintronic devices.

1.3 Silicon vs. gallium arsenide

The ideal material for semiconductor spintronic devices would be one which has large spin diffusion lengths and long but controllable electron spin lifetimes. A natural choice of material is silicon, as implementing new technologies based on current electronics would be relatively easy. There has been interest in silicon spintronic devices for many years however successful injec-

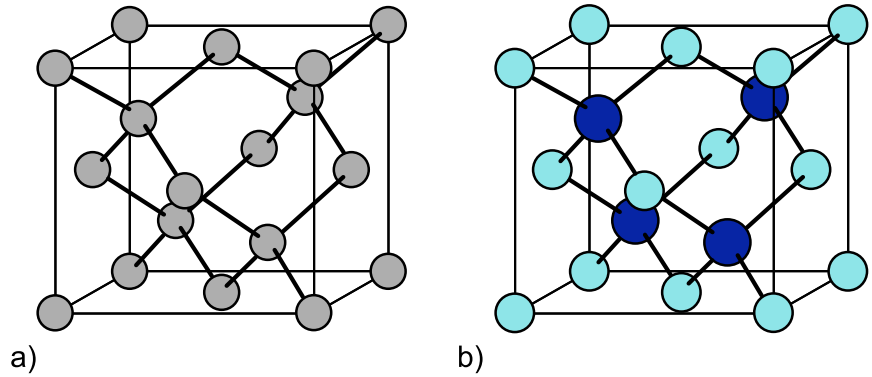

Figure 1.1: a) The diamond cubic crystal lattice structure of silicon with atomic number Z=14. b) The zincblende crystal lattice of gallium arsenide. The gallium atoms (Z=31) are represented by the light blue spheres and the arsenic atoms (Z=33) by the dark blue spheres.

tion of highly spin polarised carriers and their transport has only recently been demonstrated[8]. One reason for this is that the indirect electronic band structure of silicon results in silicon only weakly interacting with light so efficient optical injection and measurement of spin polarised carriers in silicon is difficult.

The interaction between the electron's spin and orbital motion, the spin-orbit interaction, is relatively weak in silicon as atoms possess small ionic cores (atomic number Z=14). This is illustrated in the measured valence band spin-orbit gap energy (Δ_{SO}) that is 0.044 eV for silicon whilst for germanium (Z=32) Δ_{SO}=0.29 eV. The inversion symmetry of silicon's diamond crystal lattice (figure 1.1a) produces a two-fold spin degenerate conduction band giving rise to the observed long spin lifetimes for both conduction and bound electrons at low temperatures (3 μs[9] and 60 ms respectively[10] below 10 K). The temperature dependence of the spin relaxation mechanism in silicon means that at room temperature, where future spintronic devices would ideally operate, spin lifetimes are considerably shorter $\sim$ 20 ns [11]. However, the weak spin-orbit interaction that gives rise to these long times makes manipulation of electron spin difficult, with magnetic fields being the principle method used.

The direct electronic band structure of gallium arsenide means unlike silicon it interacts strongly with light enabling efficient optical production and measurement of spin polarised carriers. The gallium (Z=31) and arsenic

(Z=33) ionic cores produce a larger spin-orbit interaction than in silicon with a valence band spin-orbit energy gap of Δ_{SO}=0.34 eV. The inversion asymmetry of the zincblende crystal lattice (figure 1.1b) results in a spin-splitting in the conduction band and consequently shorter spin lifetimes ($\sim$ 100 ps at room temperature[12]). The shorter lifetimes are compensated for as the strong spin-orbit interaction allows manipulation of electron spin alignments using electric fields[13] and strain[14]. Careful quantum well engineering has resulted in spin lifetimes of 22 ns at room temperature in n-modulation doped (110) GaAs quantum wells[15] comparable to that in silicon. The relative ease with which spin alignments can be produced, manipulated and then measured has made GaAs a very attractive and practical material for the study of electron spin dynamics.

1.4 Recent work

Research on spin dynamics in bulk and nanostructured GaAs systems has already been fruitful. There have been observations of the suppression of Dyakonov-Perel spin relaxation in (110) quantum wells[16], the spin galvanic effect in a GaAs two dimensional electron gas (2DEG)[17], the spin Hall effect in thin films of n-doped GaAs[18] and the predicted in-plane spin relaxation anisotropy in asymmetric quantum wells grown on (100) substrates[19]. Much of the research focuses on controlling electron spin through effective magnetic fields emanating from the spin-orbit interaction in the presence of asymmetry. Inversion asymmetry in the bulk crystal produces an effective magnetic field known as the Dresselhaus or bulk inversion asymmetry (BIA) field whilst asymmetry in the confinement potential of a two-dimensional system produces a field known as the Rashba or structural inversion asymmetry (SIA) field. In quantum wells, the dependence of the Dresselhaus field on the confinement size[20] and the effect of a Rashba field resulting from asymmetric doping have been studied[21]. There is also interest in developing techniques to measure the relative strengths of the two effective magnetic fields[19, 22, 23]. Recently techniques from other areas of research have been applied to measure spin lifetimes in GaAs quantum wells, for example the spin noise spectroscopy technique[24].

Although GaAs quantum wells display many of the properties required for building spintronic devices, it is unlikely that GaAs quantum wells will

be suitable for all applications. The ease at which spin lifetimes can be controlled in quantum wells[25] combined with the high mobilities obtainable in modulation doped quantum wells[26] make GaAs quantum wells strong candidates for applications that require the transport and manipulation of spin. As it is the effective magnetic fields in GaAs quantum wells that dominate electron spin physics, an understanding of these fields is essential. However, until now there has not been a direct measurement of the strength of the SIA effective magnetic field in GaAs quantum wells and consequently no comparison to that expected from theory. Once there is an improved understanding of what determines the strength of this effective field, spintronic devices that require precise control of electron spin can be realised.

1.5 Overview of thesis

This work is a study of electron spin dynamics in GaAs quantum wells, with particular focus on the effect of inversion asymmetric confinement potentials on spin lifetimes. The theory of optical alignment of electron spin in GaAs quantum wells and mechanisms that cause spin relaxation are covered in chapter 2. The chapter also contains a discussion on the role of crystallographic growth direction of quantum wells in producing desirable spintronic properties.

The experimental methods used in this work are introduced in chapter 3. The most important technique is the time-resolved Kerr rotation pump-probe technique which allows measurement of spin alignments in photo-excited conduction band electron ensembles. The ability to time-resolve the relaxation of spin alignments allows direct measurements of the spin lifetime in quantum wells under different conditions.

The majority of this work considers temporal electron dynamics in quantum wells grown on (110) substrates, this is because the electron spin lifetime in such quantum wells is an order of magnitude greater than in (100) quantum wells. When the time-resolved Kerr rotation pump-probe technique was used in this work on (110) quantum wells, an additional rotation of the probe was observed. Chapter 4 is an investigation into this optical anisotropy in two different (110) multiple quantum well samples and the origin of this anisotropy is discussed.

As a result of spin-orbit coupling, an electric field applied perpendicular

to a quantum well will produce an effective magnetic field in which spin relaxation occurs. This ability to control the spin relaxation rate is at the heart of many proposed spintronic devices. Chapter 5 is a study into the effect of an electric field on spin dynamics in (110) quantum wells, offering both the possibility of long spin memory and the control of spin relaxation. The results here were combined with mobility measurements to obtain the first measurement of the strength of the effective magnetic field as function of the applied electric field, known as the Rashba coefficient.

The work in chapter 5 allows prediction of the effect of an electric field on spin lifetimes, however symmetry arguments predict that any confinement potential that lacks inversion symmetry will increase spin relaxation. So in order understand the effect on electron spin relaxation of an asymmetric potential that isn't the result of an electric field, spin dynamics in quantum wells with asymmetric alloy composition were studied and the results are presented in chapter 6.

Chapter 7 brings this thesis to a close, highlighting the important points made in each of the chapters and discusses the implications of the results. Future experimental investigations which will further the understanding of electron spin dynamics in semiconductor quantum wells are also considered.

Chapter 2

Background Physics

This chapter covers the physics essential for understanding the experimental procedures and results presented in this thesis. A logical starting point is the physics of non-equilibrium electron populations in semiconductors, in particular gallium arsenide (GaAs).

2.1 Carriers in bulk

As atoms combine to form a solid, the discrete energy levels associated with the atomic states merge to form energy bands. In equilibrium, semiconductors have a characteristic energy gap between the filled states (valence band) and unfilled states (conduction band) known as the band gap (E_G). The energy of carriers in these bands varies with their quasi-momentum ($\mathbf{p} = \hbar\mathbf{k}$) or wavevector ($\mathbf{k} = \mathbf{p}/\hbar$). The periodic nature of a crystal lattice potential produces a periodic in $\mathbf{k}$ energy quasi-momentum relation in a crystalline semiconductor and so only needs to be solved for a particular wavevector range, known as the Brillouin zone[27].

In the process of interband absorption, a valence electron is promoted to the conduction band through the absorption of a photon with energy greater than E_G producing a positively charged hole in the valence band. As a photon of band gap energy has a comparatively small wavevector, the conservation of momentum requires that optical transitions only occur between states with the same wavevector. For a direct band gap material, where the maximum of the valence band occurs at the same wavevector as the minimum of the conduction band, resonant interband absorption can

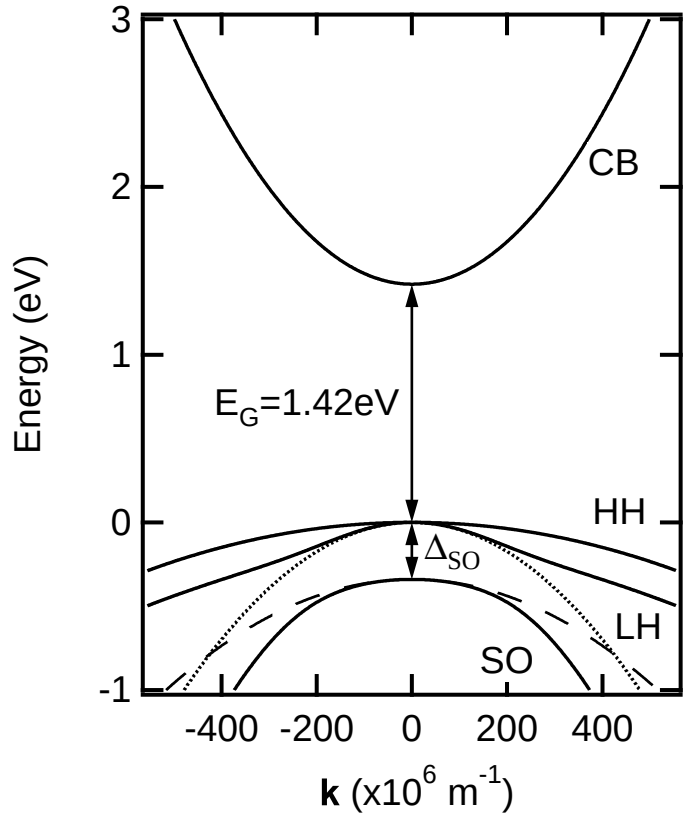

Figure 2.1: The band structure for bulk GaAs at T=300 K. CB is the conduction band, HH is the heavy hole valence band, LH is the light hole valence band and SO is the split-off valence band. Ignoring the interaction between the SO band and the LH band, there would be a crossing of the bands (dashed lines), however higher order terms in the Hamiltonian result in an anticrossing.

easily occur to produce an excited non-equilibrium state. When the band gap is misaligned in wavevector-space (indirect band gap), a photon with energy E_G alone will not suffice for promotion of an electron into the conduction band because the process will not conserve momentum (or wavevector). In order to satisfy momentum conservation an additional wavevector, typically from a vibrational mode of the crystal lattice (phonon) is required. As such a process is more complicated and therefore less probable, indirect band gap semiconductors interact weakly with light resonant with the band gap energy.

Gallium Arsenide (GaAs) is a III-V semiconductor with a zincblende

crystal lattice. The electronic band structure is depicted in figure 2.1. Near the Brillouin zone centre ($\mathbf{k} = 0$) the valence band states have p-character ($l = 1$)[1] and the conduction band states are s-like ($l = 0$). Ignoring spin-orbit effects originating from the inversion asymmetry of the zincblende crystal lattice, the conduction band has two-fold spin degeneracy and the valence band is made up of three bands each doubly degenerate, the heavy hole, the light hole and the split-off band. At the zone centre, the heavy and light hole bands are degenerate in energy whilst the split-off band lies an energy Δ_{SO}=0.34 eV below as a result of the spin-orbit interaction (see section 2.1.2). Away from the zone centre the heavy and light hole bands become non-degenerate and their dispersion is described to a first approximation by different effective masses. It can be seen from figure 2.1 that GaAs is a direct band gap semiconductor and so interacts strongly with light at the band gap energy. This allows non-equilibrium populations of carriers to be produced optically in both the conduction and valence bands at all temperatures. As the carriers are non-equilibrium they have a finite lifetime; the electron and hole will eventually recombine through either the emission of a photon (radiative recombination) or a phonon (non-radiative recombination).

2.1.1 Excitons

The photoexcited negatively charged electron and the positively charged hole experience an attraction due to the Coulomb interaction. This attraction can lead to the formation of bound states, where the electron and hole motion are correlated. These bound states are similar to the electron states in a hydrogen atom, with each state having a binding energy and an effective Bohr radius. In bulk GaAs, the effective Bohr radius is around 15 nm and the binding energy is 4.2 meV[28]. This small binding energy means that exciton effects are more important at low temperatures, where thermal excitations of the lattice (phonons) do not have sufficient energy to cause ionisation of the exciton (at 11 K, k_BT=1 meV). Therefore in order to study electron spin dynamics, measurements in this work were carried out at high temperatures (80-300 K), where excitons are rapidly ionised as they reach thermal equilibrium. Accordingly, the rest of this section will focus on the dynamics of free electrons and holes.

[1] Where l is the orbital angular momentum quantum number of the state

2.1.2 The spin-orbit interaction

As a consequence of electrons possessing an intrinsic spin angular momentum and associated magnetic moment, there is an interaction between the electron and its orbital motion. For carriers moving with velocity $\mathbf{v}$, an electric field $\mathbf{E}$ appears as a magnetic field $\mathbf{B}$ given by [29]

$$\mathbf{B} = \left(\frac{1}{c^2}\right)\mathbf{E} \times \mathbf{v} \tag{2.1}$$

where c is the speed of light. The spin magnetic moment ($\boldsymbol{\xi}$) of an electron is given by [30]

$$\boldsymbol{\xi} = -g\frac{e}{2m_0}\mathbf{s} \tag{2.2}$$

where g is the electron g-factor, m_0 is the electron mass, e is the elementary charge and $\mathbf{s}$ is the spin vector. As the energy associated with an electron's magnetic moment in a magnetic field is given by $-\boldsymbol{\xi} \cdot \mathbf{B}$, there will be different spin-orbit coupling energies for states with different spin alignments.

Considering only the radial Coulomb potential from the innermost region of the atomic cores, equation (2.1) becomes a function of the angular momentum of the state ($\mathbf{l}$) and the resulting spin-orbit interaction energy has the form $\mathbf{l}.\mathbf{s}$[29]. For conduction band states where $\mathbf{l} = 0$ there is no additional spin-orbit energy, however in the valence band ($\mathbf{l} = 1$) there is a difference in energy for states with different total angular momentum ($\mathbf{j} = \mathbf{l} + \mathbf{s}$). Therefore in diamond cubic and related crystal structured semiconductors, the heavy and light hole bands ($j = 3/2$) are separated from the split-off band ($j = 1/2$) by an energy Δ_{SO} at Brillouin zone centre. As this spin-orbit gap energy is produced by the atomic electric field, semiconductors with light nuclei have a smaller spin-orbit gap ($(\Delta_{SO})_{Si} = 0.044$ eV) than those with heavier nuclei ($(\Delta_{SO})_{Ge} = 0.29$ eV and $(\Delta_{SO})_{GaAs} = 0.34$ eV[31]).

Now considering the electric field from the bulk crystal, the symmetry of the crystal lattice becomes important. For crystal structures without an inversion centre (for example zincblende), conduction and valence bands exhibit a spin-splitting away from the Brillouin zone centre[32]. This spin-splitting increases with wavevector and produces an effective magnetic field that will induce spin relaxation[33] (see section 2.2.3). As diamond cubic semiconductors (Si, Ge) have an inversion centre this spin-splitting is absent

and therefore spin lifetimes tend to be longer.

Although limiting spin lifetimes is somewhat undesirable, the spin-orbit interaction is extremely useful in the study of spin physics as its presence allows both optical[34] and current induced[35] alignment of electron spin.

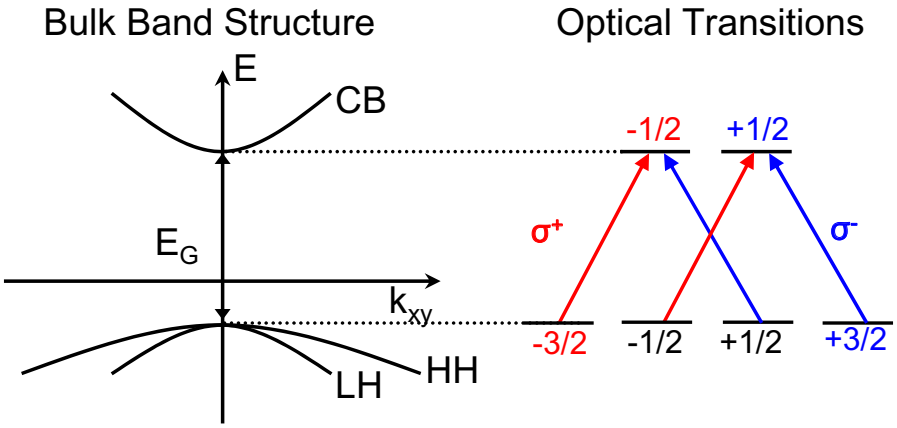

Figure 2.2: The electronic dispersion and optical transitions for band gap energy photons in bulk GaAs. Circular polarised light injects carriers from both the heavy hole (HH) ($\pm 3/2$) and light hole (LH) ($\pm 1/2$) valence bands. The numbers correspond to the component of the total angular momentum along the propagation direction of the incident light.

2.1.3 Optical alignment of spin in bulk

In the process of interband absorption, the electron and hole orbital momenta are equal to the angular momentum of the absorbed photon. The lifting of degeneracy between the SO and the LH and HH valence bands due to the spin orbit interaction makes it possible to produce a spin alignment of both electrons and holes. This is achieved using circular polarised light resonant with the heavy/light hole valence to conduction band transition to inject spin polarised carriers. As photons of σ_+ (σ_-) polarised light possess an angular momentum equal to +1 (-1) along the direction of propagation, the resulting carriers' spin become polarised in order to conserve the total angular momentum. Transitions from the HH and the LH valence bands produce opposite spin alignments (see figure 2.2), but as the transitions have unequal probabilities a net spin polarisation of 25% in the photoexcited carriers can be produced[36].

2.2 Spin relaxation in III-V semiconductors

Such a photoexcited spin alignment of electrons and holes is a non-equilibrium phenomenon and therefore has a finite lifetime. For holes in bulk GaAs, the degeneracy of the LH and HH valence bands produces a strong coupling between the hole's angular and quasimomentum[37] and so the spin orientation of holes in bulk is lost on a sub-picosecond timescale[38]. For conduction electrons, such a strong coupling does not exist and the lifetime of an electron spin alignment is longer.

To quantify spin relaxation, it is useful to define a spin relaxation time τ_s, that is the time for the aligned population to decay by a factor 1/e. In bulk III-V semiconductors there are three main mechanisms through which electron spin coherence can be lost. Each mechanism is named after the scientists that first proposed it.

2.2.1 Bir-Aronov-Pikus (BAP) mechanism

The fast spin relaxation of holes results is a spin polarised ensemble of electrons surrounded by a sea of unpolarised holes. These unpolarised holes can cause spin relaxation of electrons via the exchange interaction[39, 40]. The probability of spin relaxation via the exchange interaction is proportional to the density of unpolarised holes. Therefore this mechanism is found to dominate in p-doped samples, where there is a large background of equilibrium unpolarised holes.

2.2.2 Elliot-Yafet (EY) mechanism

Due to the spin-orbit interaction, conduction band states become coupled to valence band states. As a consequence, an electron can undergo a spin-flip when it scatters from a phonon or an impurity, and so each scattering event randomises the spin of the electrons and causes spin relaxation[41, 42]. The spin relaxation time τ_s is proportional to the transport scattering time τ_p and therefore becomes more dominant when there are more impurities. The fact that it is a consequence of the coupling between the conduction and valence band states means that the EY mechanism becomes important in narrow band gap semiconductors.

2.2.3 Dyakonov-Perel (DP) mechanism

As first predicted by Dresselhaus[32], in semiconductor crystal lattices lacking inversion symmetry, conduction band spin degeneracy is lifted away from the Brillouin zone centre. This is a consequence of the spin-orbit interaction resulting from the inversion asymmetry and hence electric field from the crystal lattice (see section 2.1.2). The result is the appearance of an extra term in the Hamiltonian for an electron in the conduction band[36]

$$\hat{H} = \frac{\hbar^2 k^2}{2m_e} + \frac{\hbar}{2}\boldsymbol{\sigma} \cdot \boldsymbol{\Omega}(\mathbf{k}) \tag{2.3}$$

where $\boldsymbol{\sigma}$ is the Pauli vector, m_e is the electron effective mass and $\boldsymbol{\Omega}$ is a vector dependent on the electron wavevector. The extra (second) term in the Hamiltonian (equation 2.3) is equivalent to the potential energy of a magnetic moment in a magnetic field. In fact, the last term describing the spin-splitting can be understood as wavevector dependent effective magnetic field, where $\boldsymbol{\Omega}$ is a spin precession vector. This effective magnetic field causes spin precession for spin components perpendicular to $\boldsymbol{\Omega}$. As shown by Mikhail Dyakonov and Vladimir Perel [33, 34], this extra term can induce spin relaxation. For when an electron scatters, the change in $\mathbf{k}$ causes $\boldsymbol{\Omega}$ to change therefore altering the spin precession. So at the heart of the spin relaxation mechanism is the spin precession that occurs between scattering that is randomised with each scattering event. There are two different regimes to consider.

When there is weak scattering $\Omega\tau_p^* >> 1$, where τ_p^* is the mean time between scattering events[2] and Ω is now the precession frequency, an initially spin aligned ensemble will undergo many rotations before a scattering event. The spin information eventually is lost as a result of the distribution of electron momenta and hence Larmor precession frequencies.

When there is strong scattering $\Omega\tau_p^* << 1$, each scattering event randomises the spin precession resulting in a spin relaxation rate τ_s^{-1}[37]

$$\frac{1}{\tau_s} = \langle \Omega_\perp^2 \rangle \tau_p^* \tag{2.4}$$

where $\langle \Omega_\perp^2 \rangle$ is the thermal average of the component of the spin precession

[2]Which can be different from τ_p as electron-electron scattering only weakly affects τ_p but can strongly affect τ_p^*[43].

vector squared that is perpendicular to the spin alignment. As can be seen in the above equation, increased scattering results in a smaller spin relaxation rate and therefore longer spin lifetime. From equations (2.3) and (2.4), it can be seen that the relaxation rate is proportional to the square of the energy.

In a III-V semiconductor lacking inversion symmetry, where x, y, z correspond to [001],[010],[100], $\mathbf{\Omega}$ has the form[36]

$$\Omega_x = \gamma k_x (k_y^2 - k_z^2) \tag{2.5}$$

where γ is a constant and Ω_y, Ω_z can be obtained through cyclic permutation of the indices. It can be seen from the equation above that in bulk $\mathbf{\Omega}$ is always perpendicular to $\mathbf{k}$. The Dyakonov-Perel spin relaxation is important in undoped semiconductors which lack an inversion centre in the crystal lattice. Importantly it is the dominant spin relaxation mechanism in both undoped bulk GaAs[37] and undoped GaAs quantum wells[12].

2.3 Carriers in quantum wells

When a thin layer of semiconductor material is sandwiched between two layers of a larger band gap semiconductor, conduction and valence band discontinuities can result in carriers preferentially residing in the smaller band gap material. If the width of the smaller band gap material becomes of the order of the de Broglie wavelength ($\lambda_b = h/(2m_eE)^{1/2} \sim 30$ nm for electrons in GaAs)[3], electron and hole wavevectors in the confinement direction become quantised. This situation is known as a type I quantum well and the energy due to the confinement can be calculated by solving the Schrödinger equation for a square well potential.

2.3.1 Envelope function approximation

In addition to the conduction and valence band offsets discussed above, the quantum well potential also includes the periodic potential from the ionic cores in the quantum well that act on the electron or hole wavefunctions. Bloch's theorem[44] states that the wavefunction of a particle in periodic

[3]Assuming room temperature thermal energy (E) and an effective mass m_e=0.067m_o

potential can be split into two parts, a quickly oscillating periodic Bloch function and a slowly varying function known as the envelope function.

When perturbations (electric or magnetic fields) that vary slowly on the length scale of the lattice constant act on carriers confined to a quantum well, the envelope function approximation[45] can be used to simplify calculations. Within the approximation, as the effect of a slowly varying potential on the fast oscillating Bloch function will be small, the potential is assumed to act only on the envelope function of the wavefunction.

The envelope part of the wavefunction (ψ_n) for a carrier in a quantum well can be calculated by approximating the well to an infinite square well of width l with the origin at the centre of the well. The solutions are

$$\langle z \,|\psi\rangle = \psi_n = \begin{cases} \sqrt{2/l}\cos(\frac{\pi n z}{l}) & \text{n odd} \\ \sqrt{2/l}\sin(\frac{\pi n z}{l}) & \text{n even} \end{cases} \tag{2.6}$$

where z is the confinement direction and n is the index of the band. The confinement energy of a given subband, that is the energy of an electron or hole state above the band edge is given by

$$E_n = \frac{\hbar^2 \pi^2 n^2}{2m^* l^2} \tag{2.7}$$

where m^* is the effective mass for electrons or holes. For an 8 nm GaAs quantum well, the confinement energy of an electron in the $n = 1$ state would be $E_{n=1} = 0.1$ eV. In reality the confinement energy is smaller than in equation 2.7 as the energy barriers are not infinitely high and therefore there is penetration of the wavefunction into the larger band gap material. From equation 2.7 it can be seen that the different masses for the heavy and light hole states give rise to different confinement energies.

2.3.2 Optical spin alignment in quantum wells

The confinement of carriers in the z-direction lifts the degeneracy of the heavy hole and light hole valence bands at the Brillouin zone centre[46](see figure 2.3). This allows optical excitation resonant with only the HH valence to conduction band transition. For normal incidence excitation, σ_+ (σ_-) polarised light excites electrons from the m_z=-3/2 (+3/2) valence band state

to the m_z=-1/2 (+1/2) conduction band state.[4] Such transitions produce a 100% spin polarised electron ensemble in the conduction band. Therefore quantum wells allow more efficient injection of spin polarised conduction electrons than in bulk GaAs. The ability to optically produce a 100% spin polarised conduction band electron ensemble is an important feature of quantum wells which simplifies the study of their spin dynamics compared to bulk material.

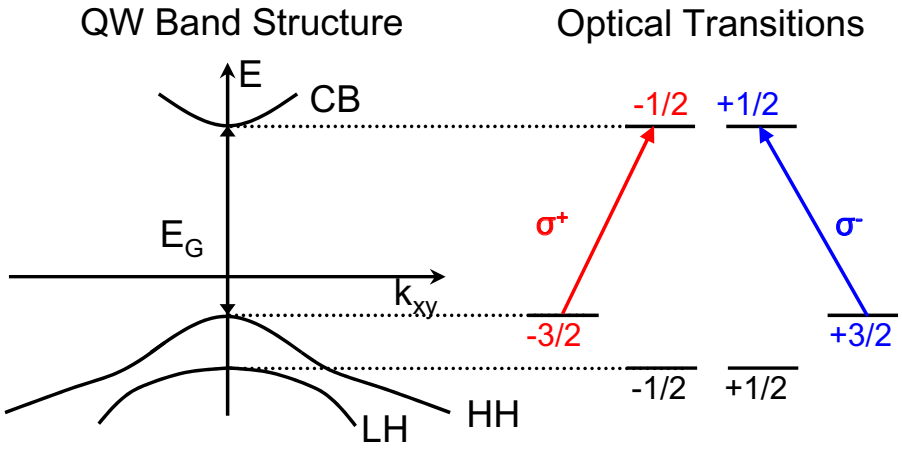

Figure 2.3: The electronic dispersion in GaAs quantum wells (QW) for the n=1 subbands and the resulting optical selection rules. The confinement lifts the heavy/light hole degeneracy at the Brillouin zone centre allowing for optical injection of 100% spin polarised conduction electrons. The numbers correspond to the component of the total angular momentum along the z (growth) direction.

2.4 Spin relaxation in quantum wells

The change in dimensionality not only changes the electronic band structure, but also the nature of the spin relaxation. For holes, the HH and LH valence bands are no longer degenerate and are therefore decoupled at $\mathbf{k}$=0. Consequently the relaxation of spin is not as rapid for a thermal equilibrium population at low temperatures as in bulk. However at higher temperatures, the holes obtain additional thermal energy and populate higher momentum states. Away from $\mathbf{k}$=0, there is a mixing of the HH and LH states and this leads to hole spin relaxation within a few picoseconds above 50 K[47].

[4] where m_z is the component of total angular momentum along the z direction.

For electrons in quantum wells, the spin relaxation mechanisms already discussed are modified by the two-dimensional confinement. As the EY mechanism only dominates in narrow band gap semiconductors, the important mechanisms for GaAs quantum wells are the BAP and DP mechanisms. Recent calculations suggest that the DP mechanism is an order of magnitude bigger in undoped quantum wells, and comparable in p-doped narrow quantum wells to the BAP mechanism[48]. As this work focuses on undoped quantum wells, this section will focus on the DP spin relaxation mechanism.

The process of confinement modifies the electron wavevector and introduces additional sources of inversion asymmetry. These asymmetries combined with the spin-orbit interaction to produce an additional spin-splitting of the conduction band that can cause DP spin relaxation.

There are three sources of inversion asymmetry in III-V semiconductor quantum wells, natural interface asymmetry (NIA), structural inversion asymmetry (SIA) and bulk inversion asymmetry (BIA). The effective magnetic field that results from all three sources can be written as[49]

$$\mathbf{\Omega} = \mathbf{\Omega_{NIA}} + \mathbf{\Omega_{SIA}} + \mathbf{\Omega_{BIA}}. \tag{2.8}$$

This allows for interference of the different fields producing interesting effects such as in-plane spin relaxation anisotropy[19, 50] and even the possibility of total suppression of the DP mechanism for all spin alignments[51].

2.4.1 Natural interface asymmetry

When the quantum well material does not share a common atom with the barrier material and atomic layers in the interface plane are either cations or anions, there is an asymmetry in the chemical bonds at the interfaces. This asymmetry can cause a spin-splitting[52] and is known as either natural or native interface asymmetry (NIA). In quantum wells that share a common atom with the barrier material, such as GaAs/AlGaAs quantum wells, this term is zero. Also for (110) quantum wells, where the planes are a mixture of anions and cations, there is no natural interface asymmetry term.

2.4.2 Rashba spin-orbit interaction (SIA)

Symmetry arguments of Rashba[13] indicate that when the potential profile of the quantum well lacks inversion symmetry an additional spin-splitting

becomes possible. As this is a result of the spin-orbit interaction it is commonly known as the Rashba spin-orbit interaction. To first order any variation in the potential of the quantum well can be represented by an electric field and the Rashba spin-orbit interaction can be written as[53]

$$\mathbf{\Omega_{SIA}} = \alpha(e/\hbar)\boldsymbol{\epsilon} \times \mathbf{k} \tag{2.9}$$

where α is known as the Rashba coefficient[5] and $\boldsymbol{\epsilon}$ is the electric field. For a quantum well with an electric field applied perpendicular to the quantum well plane, the spin precession vector has the form

$$\mathbf{\Omega_{SIA}} = \begin{pmatrix} \Omega_x \\ \Omega_y \\ \Omega_z \end{pmatrix} = \alpha(e\langle\epsilon_z\rangle/\hbar) \begin{pmatrix} k_y \\ -k_x \\ 0 \end{pmatrix} \tag{2.10}$$

where $\langle\epsilon_z\rangle$ is the expectation value of the electric field. It is important to note here that the SIA effective magnetic field spin precession vector is always in the plane of the quantum well for a transverse electric field regardless of the crystallographic growth direction of the quantum well.

2.4.3 Implications of Ehrenfest's theorem

The expectation value of the conduction (valence) band electric field is given by the expectation value of the gradient of the conduction (valence) band profile. For electrons in the conduction band

$$m\frac{d^2}{dt^2}\langle\mathbf{z}\rangle = \frac{d\langle\mathbf{p_z}\rangle}{dt} = -\langle\nabla V^c(\mathbf{z})\rangle = \langle F\rangle \tag{2.11}$$

where V^c is the potential in the conduction band and F is the force experienced by the state. This is known as Ehrenfest's theorem[54] and is a quantum mechanical equivalent of Newton's second law. For a bound state, where $\langle\mathbf{z}\rangle$ is not time dependent, the net force on the state must be zero. As a consequence, the expectation value of the gradient of the conduction band

[5]In this work the Rashba coefficient is defined as the constant of proportionality between the magnitude of the spin precession vector and the electric field and wavevector. Other conventions include incorporating the electric field into the coefficient[23] and also defining the coefficient from the Hamiltonian and Pauli spin matrices[49, 51]. Although these definitions will result in different values of and units for the Rashba coefficient, all conventions are equivalent as the coefficient always determines the spin-splitting produced at a given wavevector in the presence of structural inversion asymmetry.

potential and the conduction band electric field ($\langle\psi|\,\epsilon_z^c\,|\psi\rangle$) must be zero. This was first pointed out by Ando[55] and suggests at first sight, based on equation 2.10, that any Rashba spin-splitting must be very small.

This apparent contradiction with experimental observations was solved by Lassnig[56] and Winkler[57] by showing that it is the electric field in the valence band ($\langle\epsilon_z^v\rangle \neq 0$) averaged over the conduction band wavefunction, that should appear in equation 2.10 and so therefore Ehrenfest's theorem does not apply (see appendix A).

2.4.4 BIA in (100) quantum wells

For electrons in quantum wells, the conduction band spin splitting resulting from the asymmetry of the zincblende crystal lattice and the effective magnetic field were calculated by Dyakonov and Kachorovskii[58]. The precession vector (equation 2.5) in quantum wells depends on the crystallographic growth direction and the confinement energy. Even though the actual mechanism of spin relaxation is the same, that is spin precession in an effective magnetic field, the DP spin relaxation mechanism in quantum wells is commonly referred to as the Dyakonov-Perel-Kachorovskii (DPK) mechanism.

For (100) quantum wells, using the same axes as for bulk, terms in equation 2.5 containing k_z are replaced with the expectation value of the wavevector $\langle k_z\rangle$ determined from the momentum operator,

$$\langle p_z\rangle = \langle\psi| - i\hbar\frac{d}{dz}\,|\psi\rangle\,. \tag{2.12}$$

For carriers bound to a quantum well the expectation value for the z-component of the quasimomentum ($\hbar\langle k_z\rangle$) must be zero whereas $\langle k_z^2\rangle \neq 0$[6]. So all the k_z terms in equation 2.5 become zero and all terms with k_z^2 are replaced with $\langle k_z^2\rangle$. Assuming $\langle k_z^2\rangle >> k_x^2, k_y^2$,[7] the spin precession vector in a (100) quantum well has the form

$$\mathbf{\Omega_{BIA}}^{100} = \begin{pmatrix}\Omega_x\\ \Omega_y\\ \Omega_z\end{pmatrix} = \gamma\begin{pmatrix}k_x(k_y^2-k_z^2)\\ k_y(k_z^2-k_x^2)\\ k_z(k_x^2-k_y^2)\end{pmatrix} = \gamma\langle k_z^2\rangle\begin{pmatrix}-k_x\\ k_y\\ 0\end{pmatrix}. \tag{2.13}$$

[6] Although generally true, it can be shown easily for an infinite well as follows;
$\langle k_z\rangle = \langle\psi_1| - i\hbar\frac{d}{dz}\,|\psi_1\rangle = (-i\hbar\pi/l)\int_{-l/2}^{l/2}\cos(\pi x/l)\sin(\pi x/l)dx = 0$,
$\langle k_z^2\rangle = \langle\psi_1|\,(-i\hbar\frac{d}{dz})^2\,|\psi_1\rangle = (\pi\hbar/l)^2\langle\psi_1\,|\psi_1\rangle = (\pi\hbar/l)^2$

[7] For a 10nm GaAs QW at 200K, $k_x^2 = k_y^2 \simeq 10^{16}m^{-2}$ whilst $\langle k_z^2\rangle = (\pi/l)^2 \simeq 10^{17}m^{-2}$

The leading term in the effective magnetic field is linear in **k** and depends upon the square of the average quantum mechanical value of k_z which is proportional to the confinement energy. The spin precession vector is in the x-y plane (see figure 2.4a), so causes spin relaxation for electron spin aligned perpendicular to the plane. It can also cause spin relaxation for electron spin aligned in the plane with a non-zero perpendicular component of the spin precession vector. A dependence of the spin relaxation time on the quantum well width was observed in GaAs quantum wells, with a variation of the spin lifetime from 20-70 ps[59]. For an electric field applied normal to a quantum well, equation 2.10 shows the resulting spin precession vector is in the plane (as shown in figure 2.4b). The electron spin would see an effective magnetic field that is the resultant of the bulk inversion asymmetry and the structural inversion asymmetry fields. This effective field can have in-plane anisotropy which would manifest itself through in-plane spin relaxation anisotropy[60]. This has been observed in quantum wells with asymmetric potentials by Averkiev et al.[19].

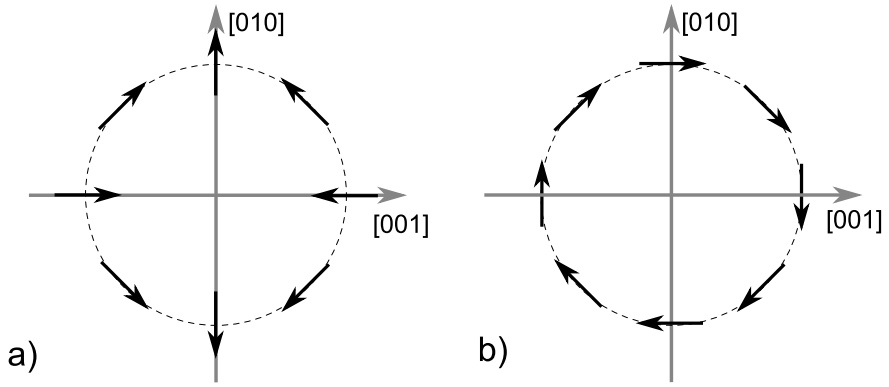

Figure 2.4: The a) Dresselhaus and b) Rashba effective fields in a (100) quantum well. As can be seen by the black arrows that represent the spin precession vector, the resulting combined in-plane field will be anisotropic.

2.4.5 BIA in (110) quantum wells

In order to calculate $\mathbf{\Omega}$ for a (110) quantum well, it is sensible to choose a new set of axes denoted by x', y', z'. A convenient choice is to keep z the quantisation direction and therefore set, x', y', z' to $[\bar{1}10][001][110]$(figure 2.5). This can be done by applying a rotation matrix to the original vector (equation 2.5). Using the 'x-convention' the three parameters that char-

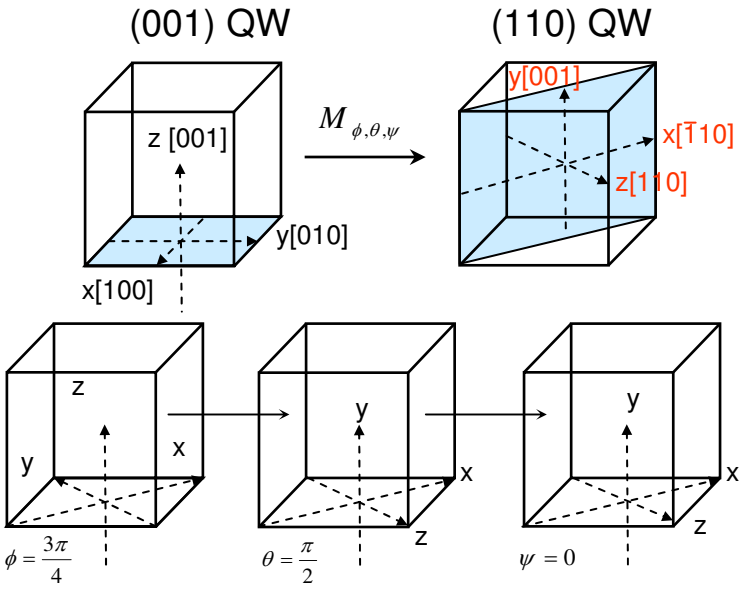

Figure 2.5: (Top) The axes for (100) quantum wells (left) and the axes for (110) quantum wells. (Bottom) The transformation broken down into steps.

acterise the rotation are anticlockwise rotations[8] about the z-axis (ϕ), the x-axis (θ) and the z-axis (ψ). Applying the rotation matrix to rotate the precession vector $\mathbf{\Omega}$ into a new set of axes $\mathbf{\Omega}'$ yields

$$\mathbf{\Omega}'(\mathbf{k}) = M_{\phi\theta\psi}\mathbf{\Omega}(\mathbf{k}). \tag{2.14}$$

However to get $\mathbf{\Omega}'$ in terms of $\mathbf{k}'$ we need to apply the rotation matrix to the wavevector from the initial set of coordinates. Therefore applying the rotation matrix to both $\mathbf{\Omega}$ and $\mathbf{k}$ with the angles $\phi = 3\pi/4$, $\theta = \pi/2$ and $\psi = 0$ (see figure 2.5) and as before assuming $\langle k_z^2 \rangle >> k_x^2, k_y^2$ one obtains

$$\mathbf{\Omega_{BIA}}^{110} = \gamma \langle k_z'^2 \rangle \begin{pmatrix} 0 \\ 0 \\ \frac{k_x'}{2} \end{pmatrix}. \tag{2.15}$$

That is the effective magnetic field is perpendicular to the quantum well plane. This means there is a suppression of the Dyakonov-Perel spin relaxation mechanism for spin aligned normal to the quantum well plane. This

[8] As viewed by an observer facing towards the origin.

was experimentally confirmed by Ohno et al. [16] where measured spin lifetimes in GaAs quantum wells were of the order of nanoseconds. Currently the mechanism limiting the spin lifetime in (110) quantum wells is not clear.

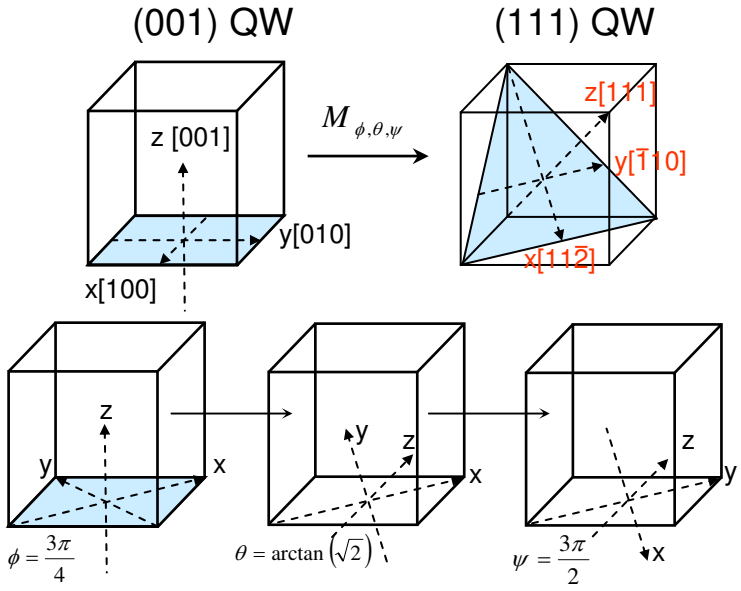

Figure 2.6: (Top) The axes used for (100) quantum wells (left) and (111) quantum wells (right). (Bottom) The transformation broken down.

2.4.6 BIA in (111) quantum wells

For (111) quantum wells, we choose yet another set of axes (see figure 2.6) and for consistency set z' to the quantisation direction [111] and x', y' to [11$\bar{2}$][$\bar{1}$10] directions respectively. This is done by applying the rotation matrix with the angles $\psi = \frac{3\pi}{4}, \theta = \arctan(\sqrt{2})$ and $\phi = \frac{3\pi}{2}$ to equation 2.5

$$\mathbf{\Omega_{BIA}}^{111} = \gamma \frac{2}{\sqrt{3}} \langle k_z'^2 \rangle \begin{pmatrix} k_y' \\ -k_x' \\ 0 \end{pmatrix}. \tag{2.16}$$

The effective magnetic field is in the plane and as in (100) quantum wells permitting the interference of the BIA and SIA effective magnetic fields. The form of equation 2.16 is identical to 2.10 opening up the exciting possibility of engineering (111) quantum wells which have equal SIA and BIA strengths but opposite signs. The result would be quantum wells where the

spin-splitting disappears for all values of electron momenta[51]. However, experimental verification of this interesting effect is still lacking. Quantum wells grown on (111) substrates were grown during the course of this project, however initial measurements suggested poor quantum well growth and consequently no time-resolved spin studies were conducted.

2.5 Underlying ideas of the project

As illustrated in this chapter, the combination of electric fields, built-in or applied, and careful selection of the quantum well growth direction allows complete control of the spin precession vector. As the spin precession vector drives Dyakonov-Perel spin relaxation, quantum wells provide an exciting medium for spin physics in which different asymmetries compete and provide the possibility of gate controlled spin lifetimes. This competition and control owe to the existence of the spin-orbit interaction. Many of the exciting spin-orbit induced phenomena in semiconductor quantum wells are still to be explored whilst those that have raise further questions that need to be addressed.

One of those questions is on the magnitude of the spin-orbit induced conduction band spin-splitting due to asymmetry from alloy engineering (figure 2.7a) and electric fields (figure 2.7b). Unfortunately the symmetry arguments used by Rashba [61, 13] to show that a confinement potential lacking inversion symmetry will lift conduction band spin-degeneracy do not permit predictions of the magnitude of SIA effective magnetic fields in quantum wells from different sources. Although measurements have been made of the effect of alloying engineering[19] and an external electric field[25] on spin dynamics, a comparison between their magnitudes is not possible because it was not possible to measure the induced spin-splitting directly.

In (100) quantum wells both the BIA and the SIA (Rashba) effective magnetic field precession vectors are in the quantum well plane (figure 2.7c). Therefore, when a quantum well potential is inversion asymmetric, electron spin aligned normal to the quantum well will experience the effect of both the BIA and the SIA. Averkiev et al.[19] measured the magnitude of the relative strengths of the SIA and BIA effective magnetic fields in alloy engineered (100) quantum wells (figure 2.7a). Obtaining a ratio of 1 : 4 and they assumed that the SIA contribution to the spin-splitting was bigger than the

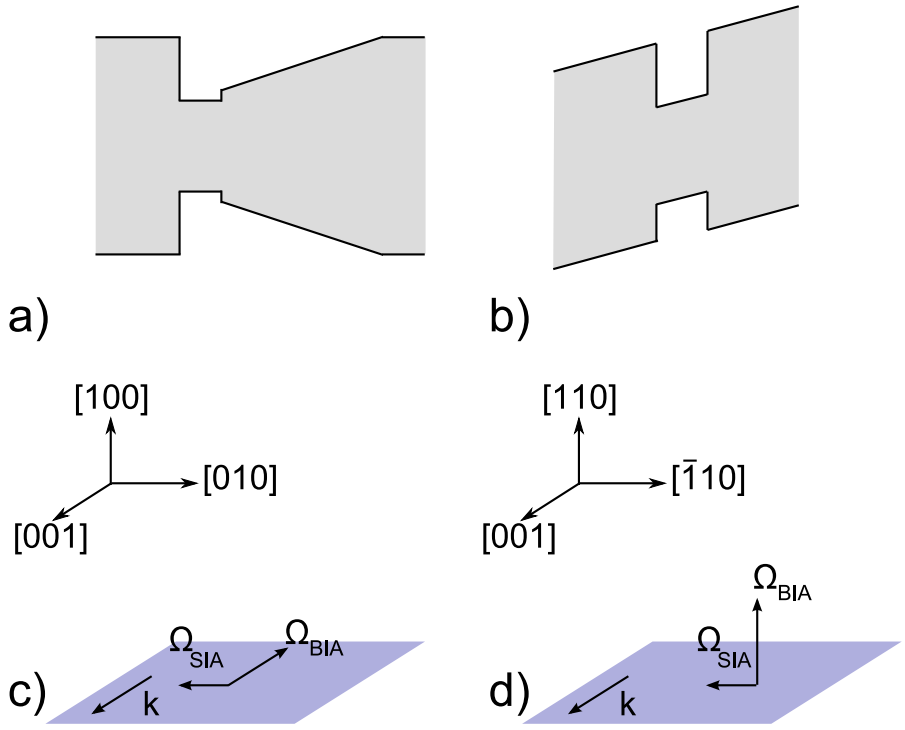

Figure 2.7: a) The asymmetric potential produced by alloy engineering used in [19]. b) An asymmetric potential resulting from an electric field. c) and d) show effective magnetic fields for an electron with a wavevector **k** parallel to [001] in a (100) and (110) quantum well respectively. The structural inversion asymmetry (SIA) field is in the quantum well plane for both cases, whilst the bulk inversion asymmetry (BIA) field is in the plane for the (100) and normal to the plane for the (110).

BIA contribution. As it was a measure of the relative strengths it is not possible to determine the size of the SIA spin-splitting, or indeed, which effective field is the larger of the two.

In (110) quantum wells (figure 2.7d), the BIA effective magnetic field precession vector is normal to the quantum well plane, whilst any SIA precession vector will be in the quantum well plane. For spin aligned normal to an asymmetric (110) quantum well, the only effective field that can cause Dyakonov-Perel spin relaxation is the SIA. This was utilised in the work of Karimov et al.[25] to isolate the effect of the SIA effective magnetic field from the BIA and demonstrate successful control of the spin relaxation using a variable electric field applied normal to the quantum well plane. However,

the Dyakonov-Perel spin relaxation rate in the presence of strong scattering (equation 2.4) is given by the product of both the thermal average of the spin-splitting squared and the electron scattering time. So without measuring of the electron scattering time it is not possible to determine the strength of the Rashba spin-orbit interaction, it can only be inferred.

The aim of this work was to compare the effect of asymmetry from an electric field on spin dynamics to asymmetry from alloy engineering. The effect of the SIA effective field on spin lifetime was isolated from the BIA through the use of (110) quantum wells. Then by combining measurements of the electron spin relaxation rate and the electron scattering time, the structural inversion asymmetry spin-splitting was measured (equation 2.4).

The first stage was to conduct a study of the time-resolved Kerr rotation technique for (110) quantum well (chapter 4) in order to accurately measure electron spin relaxation times in (110) quantum wells. The next stage was to measure the Rashba coefficient in equation 2.10 by studying the effect of an electric field on spin dynamics at different temperatures (chapter 5). The final stage of this work presented in chapter 6, was a study of electron spin dynamics at different temperatures for quantum wells with asymmetry as used by Averkiev et al[9](figure 2.7a). By time-resolving the spin relaxation in (110) alloy engineered wells, it was possible to directly measure the effect of the asymmetry on spin lifetimes. Then combining the determined spin relaxation rate with measurements of the electron scattering time, the spin-splitting in the presence of both forms of asymmetry was calculated.

[9]The profile was the same but our samples contained a higher fraction of aluminium (x=0.4 compared to x=0.28) in the barriers.

Chapter 3

Experimental Methods

The experimental techniques used in this work are explained and discussed in this chapter. The samples were grown by Professor Mohamed Henini at the University of Nottingham via molecular beam epitaxy (MBE). Techniques are introduced chronologically, starting with measurements to characterise the quality of a new sample followed by investigation of spin dynamics.

3.1 Photo-Luminescence (PL)

The quality of the quantum well sample was assessed by optically exciting carriers in the sample and then measuring the resulting light emission (photoluminescence or PL). The light emission consisted of bulk luminescence from the GaAs substrate and shorter wavelength emission from the quantum well states. The position and width of the n=1 heavy and light hole PL peaks were used to determine the confinement energy in the quantum wells and the variation in the width of the quantum well(s) within the sample.

A standard set up for PL at variable temperature (4.2 K to 300 K) was used as illustrated in figure 3.1. Samples were excited by a continuous wave (CW) light source of power 0.5 mW, using either a Helium Neon laser (HeNe) or the CW output of a Ti:Sapphire laser (Coherent © MIRA 900). The collected luminescence was collimated and coupled to the spectrometer via an optical fibre. Various spectrometers were used, for example an OceanOptics © USB spectrometer (HR2000) with a 2048-pixel CCD linear image sensor and a SPEX monochromater in combination with a photomultiplier tube (PMT) with an S20 photocathode. Typical energy resolutions

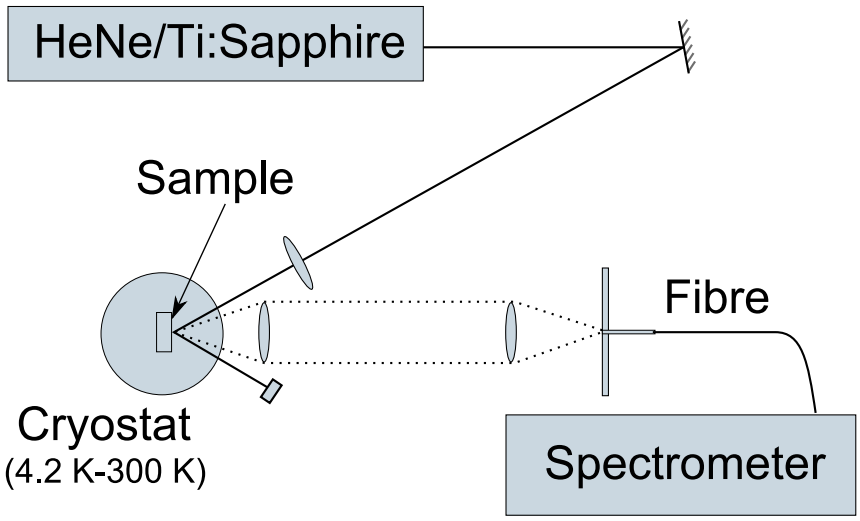

Figure 3.1: The typical photoluminescence set up. Laser light with energy above the band gap of GaAs was used to inject carriers into the conduction band. Over time the carriers recombine emitting light that was collimated and fibre coupled into a spectrometer.

(FWHM) were 0.8 meV and 0.2 meV respectively. The position of the PL peak at different temperatures was required to determine the photon energy for spin dynamics measurements resonant with the HH transition.

Figure 3.2a shows spectra for a typical (110)-oriented quantum well sample at various temperatures. At low temperature only the HH peak is observed but at higher temperatures both the HH and the LH peaks are detected. The width of the HH peak at low temperature was used to assess the quality of the samples.

Figure 3.2b shows a comparison of a good quality (100)-oriented MBE grown multiple quantum well (MQW) sample with a nominally similar sample grown on (110) and (111)B substrates. As the optimum growth conditions for (100) quantum wells are well established PL measurements on (100) samples typically had narrow PL peaks (figure 3.2b). The optimum growth conditions for (110) quantum wells require lower substrate temperatures and are less readily achieved. The low temperature PL peak from (110) samples typically had a larger width. The PL of the (111)-oriented sample indicates that the growth conditions did not produce a quantum well structure in this case. Table 3.1 gives details of the PL for the samples studied in this work.

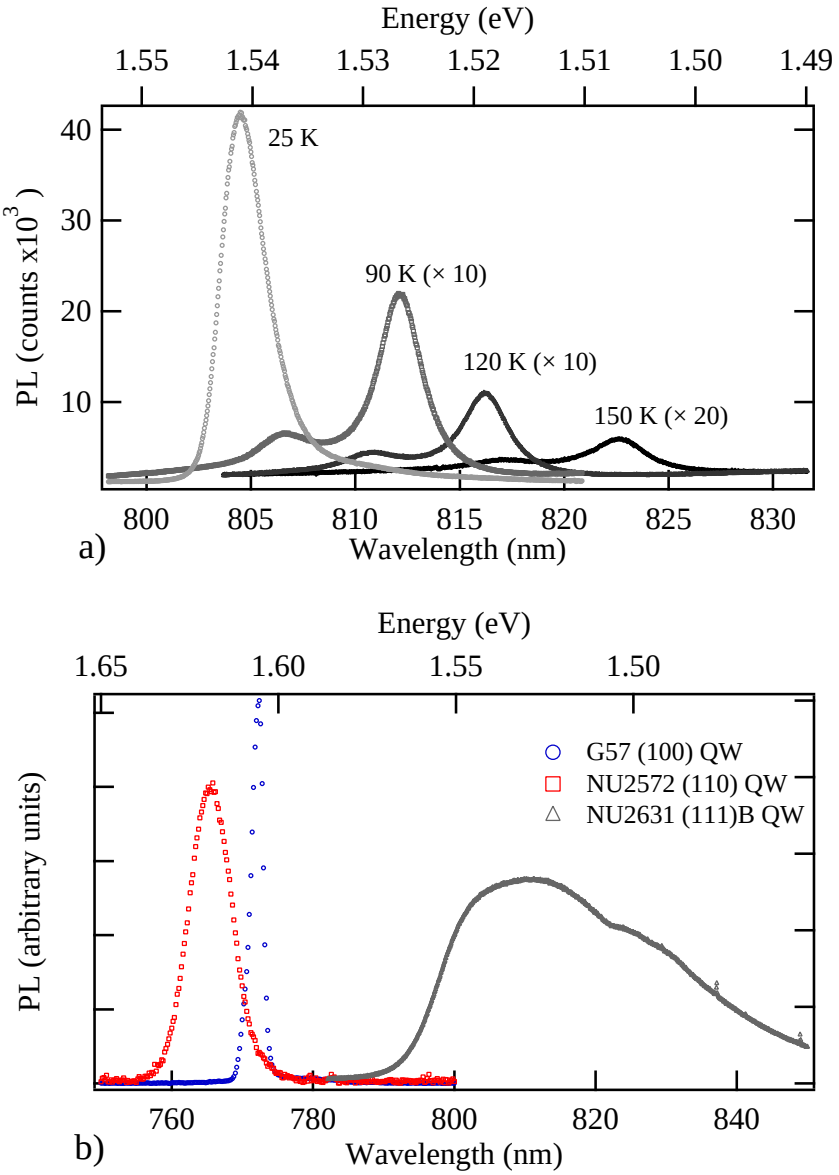

Figure 3.2: a) PL from a (110) multiple quantum well (MQW) sample (NU2618) at different temperatures. With increasing temperature the PL peak shifts to longer wavelengths as a result of the band gap decreasing with temperature[62]. b) Low temperature ($\leq$ 25 K) PL for samples on three different orientated substrates. The PL from all (111) samples grown were similar to that of sample NU2631 and therefore no spin dynamics measurements were taken on (111) quantum well samples.

Sample	Description	T(K)	PL_{peak}(eV)	PL_{width}(meV)	W*(nm)
G57	(100) 6.0nm S	5	1.61	3.0	5.5
NU2281	(100) 7.5nm S	5	1.57	1.9	8.0
NU2284	(110) 7.5nm S	5	1.58	6.5	7.5
NU2307	(110) 7.5nm S	170	1.54	12.9	7.0
NU2572	(110) 7.5nm S	10	1.62	15.2	5.0
NU2631	(111) 7.5nm S	25	1.53	800	10.5
NU2618	(100) 8nm AS	25	1.54	5.0	10.5
NU2620	(110) 8nm AS	25	1.55	5.6	10.5
NU2621	(110) 8nm AS	25	1.55	4.7	10.5
NU2654	(110) 8nm AS	25	1.55	3.1	10.5
NU2662	(100) 8nm AS	25	1.55	3.6	10.5

Table 3.1: A summary of PL measurements at different temperatures for the samples studied in this work. The first six samples have symmetric (S) abrupt variation of the alloy composition whilst the last five are asymmetric (AS) quantum wells with one abrupt and one graded interface (see figure 2.7a). The W* corresponds to an estimate of the actual well width from the position of the PL peak.

3.2 Pump-probe Kerr rotation

The time-resolved Kerr rotation pump-probe technique developed by our group in Southampton[63], was used to study temporal spin dynamics in GaAs quantum wells. The present set-up is indicated in figure 3.3. An argon-ion CW laser was used to pump a mode-locked Ti:Sapphire laser (Coherent © MIRA 900) operating in picosecond (ps) mode with a repetition frequency of 76 MHz. The wavelength of the MIRA could be tuned from $\sim$ 700-900 nm and pulses typically had 2-3 ps temporal width corresponding to a spectral resolution of about 0.3 meV. The initially linear polarised beam was split into two beams using a polarising beam splitter (PBS1), one becoming the pump beam, the other becoming the probe beam. The relative intensities of the two beams could be controlled through adjustment of the half-wave plate ($\lambda/2$) immediately after the output of the MIRA or through variable neutral density filters (not shown in figure 3.3). The pump beam made a single pass of a corner cube (CC1) and then passed through a Soleil-Babinet compensator (SBC) in order to produce circular polarised light (σ_- or σ_+). The circular polarised pump then passed through the outer teeth of a dual frequency optical chopper (OC) wheel to modulate the beam at a frequency

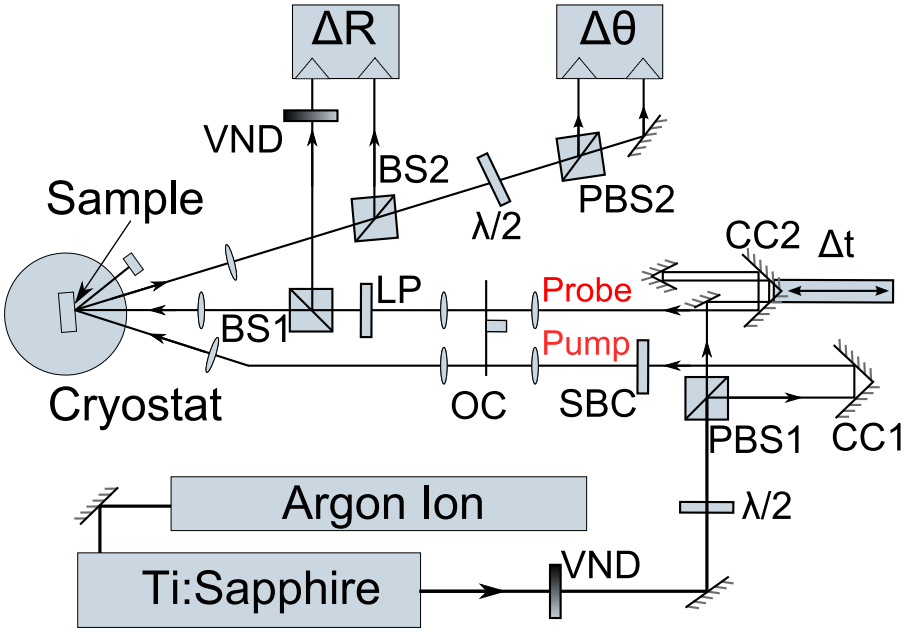

Figure 3.3: The time-resolved Kerr rotation pump-probe set-up (see the text for an explanation of all the abbreviations used). Pulses from a Ti:Sapphire were split between pump and probe beams. The pump was circular polarised using a Soleil-Babinet compensator (SBC) whilst the probe was linearly polarised using a linear polariser (LP). With the use of a translation stage a time delay (Δt) was introduced in the probe relative to the pump. The pump induced change in the reflectivity (ΔR) and the change in the polarisation ($\Delta\theta$) of the probe were monitored as a function of time delay(Δt).

(f_1 =1.1 kHz).

The probe beam was directed to a corner cube (CC2) mounted on a motorised mechanical stage allowing the introduction of a variable delay (Δt) relative to the pump beam. The probe beam made a double pass of the translation stage allowing maximum delay of up to 4 ns relative to the pump. Then it passed through the inner teeth of the optical chopper (OC), modulating the beam at a different frequency to the pump (f_2=1.8 kHz). The probe beam then passed through a linear polariser (LP), to ensure the polarisation of the probe was parallel to the optical bench. Both beams were then focused onto the sample, typical spot sizes were 45 μm (pump) and 20 μm (probe). Typical excitation power of the pump was 0.5 mW and the probe was 25 μW, corresponding to a power density ratio of around 4 : 1. The total power of the pump and probe beams could be changed using a

variable neutral density (VND) filter at the output of the MIRA.

3.2.1 Setting of the pump polarisation

The settings on the Soleil-Babinet compensator (SBC) to give circular polarisation were determined using a rotating linear polariser in combination with a photodiode. The photodiode was placed in the path of the pump beam with a motor driven rotating linear polariser placed just before. With the aid of a lock-in amplifier to monitor the output of the photodiode, the variation in the light intensity was minimised using the Soleil-Babinet compensator. To determine the helicity, combinations of quarter-wave plates with linear polarising sheets were used to maximise the transmitted light. Once the settings for both circular polarisations were determined the rotating polariser and photodiode were removed from the beam path.

3.2.2 Balanced detection

The pump-induced change in the reflectivity (known as ΔR) and polarisation (known as $\Delta\theta$) of the probe were monitored through the use of the balanced detection technique. The balanced detectors consisted of two identical photodiodes connected in opposition, the current from the one being used as a reference being subtracted from the current output of the other. The current difference was amplified into a voltage using a transimpedance amplifier. The main advantage of balanced detection is the rejection of common-mode noise. For example power fluctuations in the laser intensity. This allows measurements of ΔR and $\Delta\theta$ signals to approach the limit set by shot noise.

In order to monitor the change in the reflectivity, a fraction of the probe beam before it was focused onto the sample was steered onto one of the photodiodes via a variable neutral density filter using a non-polarising beam splitter (BS1). This was then balanced with a fraction of the probe beam taken after reflection from the sample using another non-polarising beam splitter (BS2). Through the use of the variable neutral density filter, the output voltage from the two photodiodes could be balanced exactly.

The change in the polarisation of the probe was monitored through analysing the polarisation of the reflected probe beam. The remaining fraction of the beam was passed through a half-wave plate ($\lambda/2$) then a polarising

beam splitter (PBS2). The two emerging beams were directed onto the two photodiodes. The detector was balanced by changing the orientation of the half-wave plate to produce equal currents from the photodiodes as viewed on an oscilloscope. Any rotation of the plane of polarisation of the probe beam would then produce an imbalance. In order to measure the pump-induced change in both the reflectivity and the polarisation of the probe, the detectors were balanced in the absence of the pump beam.

3.2.3 Lock-in detection

A major problem with measuring small pump-induced changes of ΔR or $\Delta\theta$ is the scattering of light from the pump beam into the detectors. This can be solved by chopping pump and probe beams at different frequencies and using lock-in detection at the sum of the two frequencies. Chopping the pump allows the effect of the pump-induced change in ΔR and $\Delta\theta$ to be detected. While chopping the probe allows the probe signal to be separated from pump light scattered into the detectors. The voltages from the balanced detectors were connected to the input channels of two lock-in amplifiers (Stanford Research Systems © SR830). The sum frequency $(f_1 + f_2)$ reference output of the optical chopper control unit was used as the reference signal for both lock-in amplifiers ensuring only pump induced changes of the probe would be detected.

The x, y and R channels of the lock-in amplifiers were recorded using a computer. Typically, a time constant of 1 s and a roll-off of 24 dB per octave were used. For the $\Delta\theta$, the typical noise level on the output of the lock-in amplifier was 1 μV and a maximum output of $\sim$ 2 V could be produced when the half-wave plate was rotated to unbalance the detectors. Therefore using the lock-in detection technique, the $\Delta\theta$ signal could be used to detect a rotation of $\sim 2.3 \times 10^{-5}$ degrees in the probe. This is a very small angle in comparison to the typical the pump induced rotation of the probe ($\sim 5 \times 10^{-2}$ degrees[63, 64]).

3.2.4 Cryostat system

To perform measurements at low temperatures, samples were placed into a continuous flow cryostat in which the sample is surrounded by cold flowing gas. This allowed precise control of temperature between 4 K and 300 K.

The sample was mounted at the end of a sample stick in the inner region of the cryostat thermally isolated by a high vacuum outer chamber evacuated to a pressure of $\sim 10^{-7}$ mbar. The inner region and sample were cooled by a continuous flow of either cold helium or nitrogen gas from a storage Dewar. The temperature was stabilised through careful control of the gas flow and a heating element in the inner region. A PID (proportionalintegralderivative) controller was used to monitor the temperature and adjust the heater accordingly. The cryostat had fused quartz windows that allowed optical access to the sample.

3.2.5 Application of voltages to samples

At the end of the sample stick was a chip carrier (see figure 3.4a) that enabled voltages to be applied to samples fabricated into p-i-n (or n-i-p) devices (figure 3.4b). The contacts at the base of the chip carrier were soldered onto wires that ran up the sample stick and out of the cryostat. For a sample in the chip carrier, sprung metallic pins made electrical contact with the chip allowing a voltage applied across different wires to produce a voltage between contacts on the sample. A Keithley © 238 source measure unit (SMU) was used to apply a constant voltage for spin measurements in an electric field and for measuring current-voltage characteristics a sample.

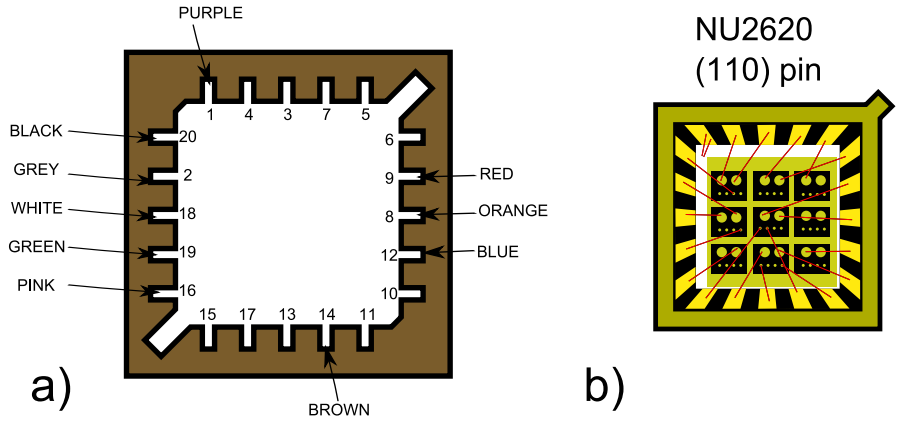

Figure 3.4: a) A schematic of the chip carrier and the colour of the wires connected to each contact. b) The connections on a p-i-n sample. The red lines correspond to wires that connect the p-i-n devices (gold circles) to metal contacts that run to the edge of the sample.

3.2.6 Measurements as a function of wavelength and delay

Typical ΔR and $\Delta\theta$ signals as a function of wavelength at fixed delay (typically $\sim$ 40 ps) and as a function of delay at fixed wavelength are shown in figure 3.5. To scan the wavelength at fixed delay the Lyot filter of the MIRA was driven by a stepper motor from a computer via a gear train. The PL measurements were used as a guide to set the MIRA wavelength to the HH absorption of the quantum well for the given temperature. The variation of ΔR and $\Delta\theta$ signals with wavelength are quite different, it being noticeable that the peak of the $\Delta\theta$ coincides approximately with a zero in ΔR. This is a common feature of the measurements in this work. It is a consequence of the fact that the ΔR results from the total phase-space filling (see section 3.2.7) whereas $\Delta\theta$ is produced by the differential phase-space filling with respect to polarisation.

The wavelength scans were used typically to identify conditions where measureable ΔR and $\Delta\theta$ signals could be recorded simultaneously in a delay scan. Since the optical components in the set-up showed some slight chromaticity, for delay scans taken at different wavelengths the detectors were rebalanced and the Soleil-Babinet compensator reset to give exact σ_- or σ_+ pump polarisation.

3.2.7 Interpretation of signals

Care had to be taken when interpreting the signals as many physical processes can induce changes in the reflected probe beam. The variations in the optical properties of quantum wells with wavelength near the quantum well absorption also means the following discussion is limited to the temporal evolution of the signals at a fixed wavelength. The interpretation used in this work was developed through studies of spin dynamics in undoped (100) quantum wells[12, 65, 66] where there are an equal number of electrons and holes. An additional rotation of the probe discovered in this work in (110) GaAs/AlGaAs quantum wells is not addressed here as it is discussed in chapter 4.

With the arrival of each pump pulse resonant with the n=1 HH to conduction band transition there was an injection of spin polarised excitons into the quantum well layer. In the temperature range studied in this work (80-300 K), these excitons were rapidly ionised predominately by LO phonons

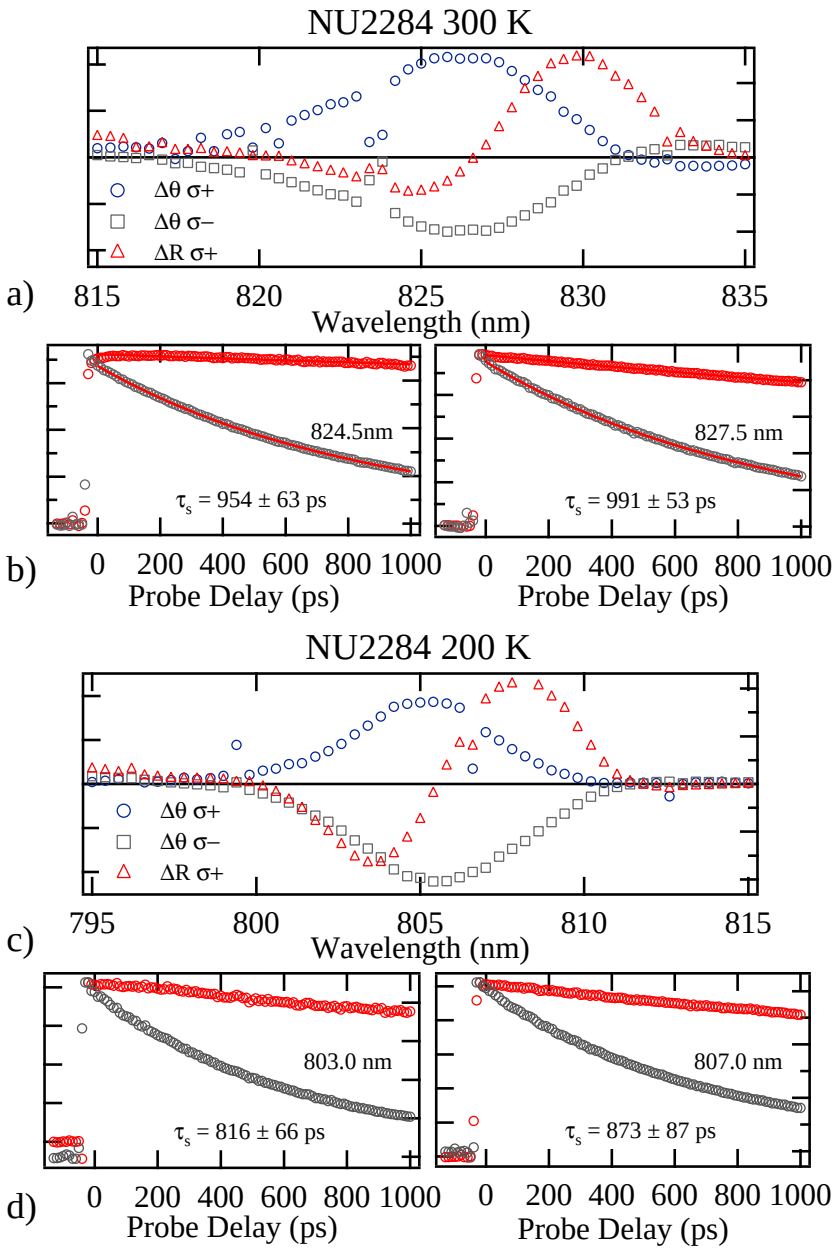

Figure 3.5: Measurements on NU2284. a) and c) The preliminary measurements taken before time-resolved measurements were taken at a fixed delay of 40 ps for 300 K and 200 K respectively. These measurements allowed wavelengths to be chosen to take the time-resolved measurements. b) and d) show the ΔR (red) and $\Delta\theta$ (grey) time-resolved for both long and short wavelengths at 300 K (b) and 200 K (d) and the calculated spin lifetimes.

within the first 0.4-10 ps[12] with the electrons and holes retaining their spin alignments. Therefore any changes in the reflectivity or polarisation of the probe after the first 10 ps were a result of free electrons and holes.

Concentrating on delay times greater than 10 ps, at a fixed wavelength the main mechanism in the change of reflectivity of the sample is phase-space filling[65] by free carriers. The pump induced excited population of carriers change the absorption coefficient and the refractive index. So for a fixed wavelength any change in ΔR in this work was assigned to the population of photoexcited holes and electrons. As the recombination rate of electron and hole populations would be the same the relaxation of the ΔR signal was used to calculate the relaxation time of the electron population. The recombination time was measured by fitting an exponential of the form $Ae^{-t/\tau}$, where A is a constant, to the ΔR signal and equating the calculated relaxation time to the recombination time of the electrons ($\tau = \tau_{\Delta R}$).

The dominant mechanism for change in the polarisation of the probe is due to phase-space filling resulting from the preferential injection of carriers with a particular spin alignment[65]. By considering the linear polarised probe as a combination σ_+ and σ_- it is possible to understand a rotation as a consequence of different refractive indices for the different circular components. In the presence of spin polarised carriers one would expect different absorption coefficients for the different polarisations and also different refractive indices. This would result in a change in the phase of the two components in the reflected beam and therefore a rotation (and elliptisation). The circular polarised pump injects 100% spin polarised carriers in both the conduction and valence bands. The spin alignment of the holes as described in section 2.4 above 50 K is lost within 5 ps[47]. Therefore any change in the polarisation of the probe in this work was assigned to the spin alignment of conduction electrons. Again, by fitting an exponential of the form $Ae^{-t/\tau}$ to the $\Delta\theta$ signal, it was possible to measure the relaxation time of the spin alignment in the quantum well ($\tau_{\Delta\theta}$).

The relaxation of the spin alignment can result from both the recombination of the carriers and the relaxation of the spin. Therefore, by measuring both the recombination time (ΔR) and the relaxation time of the spin alignment ($\Delta\theta$) it was possible to determine the spin relaxation rate τ_S^{-1},

$$\tau_S^{-1} = \tau_{\Delta\theta}^{-1} - \tau_{\Delta R}^{-1} \tag{3.1}$$

where τ_S will be referred to as the spin relaxation time.

3.3 Transient spin grating

The transient spin grating technique (see figure 3.6) was used to measure spin diffusion in undoped GaAs quantum wells. The measurements performed by Will Leyland and Jonathan Mar (University of Cambridge) were combined with the pump-probe Kerr rotation measurements in Southampton to calculate the electron mobility and thus the spin-orbit splitting (see section 2.5) in undoped GaAs quantum wells. A description of the spin-grating technique based on the description in Will Leyland's thesis [67] is included here for completeness.

Two pump beams giving coincident pulses from a modelocked Ti:Sapphire laser operating in femtosecond (fs) mode were focused onto the sample at equal incident angles. The two beams had crossed linear polarisation which produced no variation of intensity but a modulation in the polarisation of the optical field on the sample from linear, through to σ_+, to linear, to σ_- and back to linear. This modulation excited carriers with spin alignments that followed the polarisation modulation, creating a spatial modulation in the spin alignment (figure 3.6b) without modulation of the population. The temporal decay of the grating was monitored by measuring the intensity of a diffracted circular polarised probe beam for increasing time delay relative to the pumps. Measurements at different temperatures were made by mounting the sample in a cryostat similar to that used in the Kerr-rotation measurements.

3.3.1 Interpretation of signals

The decay of the diffracted probe gives directly the relaxation of the spin grating. The relaxation of a spin grating can result from recombination, carrier diffusion and spin relaxation. The decay rate of a grating is given by [68]

$$\Gamma = D_s \frac{4\pi^2}{\Lambda^2} + \tau_s^{-1} + \tau_r^{-1} \tag{3.2}$$

where D_s is the diffusion coefficient, Λ is the pitch of the grating and τ_r is the recombination time. The rapid dissociation of excitons and the fast spin relaxation of holes results in the spin grating becoming an electron spin

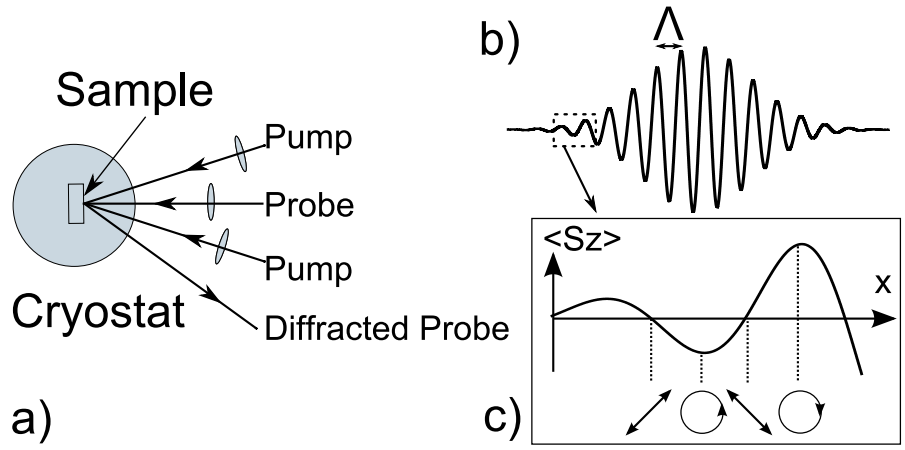

Figure 3.6: a) The transient spin grating method. Two crossed linear polarised pump beams were used to create a modulation in the polarisation of the light on the sample. This created a spin grating, which was monitored by measuring a third circular polarised probe beam diffracted from the grating. b) A schematic of the spin grating. c) The spatial modulation of the spin alignment ($\langle S_z \rangle$) and polarisation of the optical field (bottom).

grating after around 10 ps. This means the pump-probe Kerr rotation measurements of the electron spin relaxation rate (τ_s^{-1}) and the recombination rate ($\tau_r^{-1} = \tau_{\Delta R}^{-1}$) could be used in equation 3.2. Therefore by combining the transient spin grating measurement of Γ with the pump-probe Kerr rotation measurement of τ_s^{-1} and τ_r^{-1} the spin diffusion coefficient for electrons could be calculated.

The importance of using a spin-grating, where the total population of electrons and holes is spatially uniform, rather than an intensity grating, which gives a non-uniform population, is that in the former the electron diffusion is not influenced by the space charge of the holes. Population gratings give information on the combined self diffusion of electrons and holes which is generally limited by the (slower) hole diffusion.

In undoped quantum wells where there is typically a low concentration of electrons, interactions between electrons can be ignored and the spin diffusion coefficient can be equated to the electron diffusion coefficient ($D_s = D_e$). Following this assumption, for a Boltzmann distribution of electron energies, it is possible to calculate the mobility (μ) and hence the scattering

time (τ_p*) using Einstein's equation

$$\mu = \frac{e\tau_p^*}{m_e} = \frac{e}{k_B T} D_e \tag{3.3}$$

where k_B is the Boltzmann constant, T is the temperature and m_e is the electron effective mass.

Chapter 4

Optical Anisotropy in (110) GaAs Quantum Wells

The time-resolved Kerr rotation pump-probe technique was initially developed through studies of dilute magnetic semiconductor bulk layers[63] and heterostructures[69] grown on (100) zincblende semiconductor substrates. In this high rotational symmetry direction, the pump-induced change in the polarisation of the probe is assigned to the degree of spin alignment parallel to the beam. As quantum wells grown on (110) zincblende substrates only possess two-fold symmetry along the growth axis, the in-plane linear optical properties have been observed to be anisotropic[70, 71]. This chapter presents a study of a spin independent rotation of the probe in (110) GaAs quantum wells and describes how the time-resolved Kerr rotation technique was adapted for spin measurements in (110) quantum wells. The results of this chapter influenced the nature of the experimental procedure followed in the remainder of this work and have implications for optical studies of spin dynamics in systems along axes that are not high symmetry directions.

4.1 Determining orientations of samples

Two undoped quantum well samples grown via molecular beam epitaxy (MBE) by Mohamed Henini at the University of Nottingham were studied in this chapter. The first sample was NU2284 (figure 4.1a), comprising 20 repeats of a 12 nm $Al_{0.4}Ga_{0.6}As$ barrier and a 7.5 nm GaAs well deposited on a (110) oriented substrate. The position and width of the low temperature

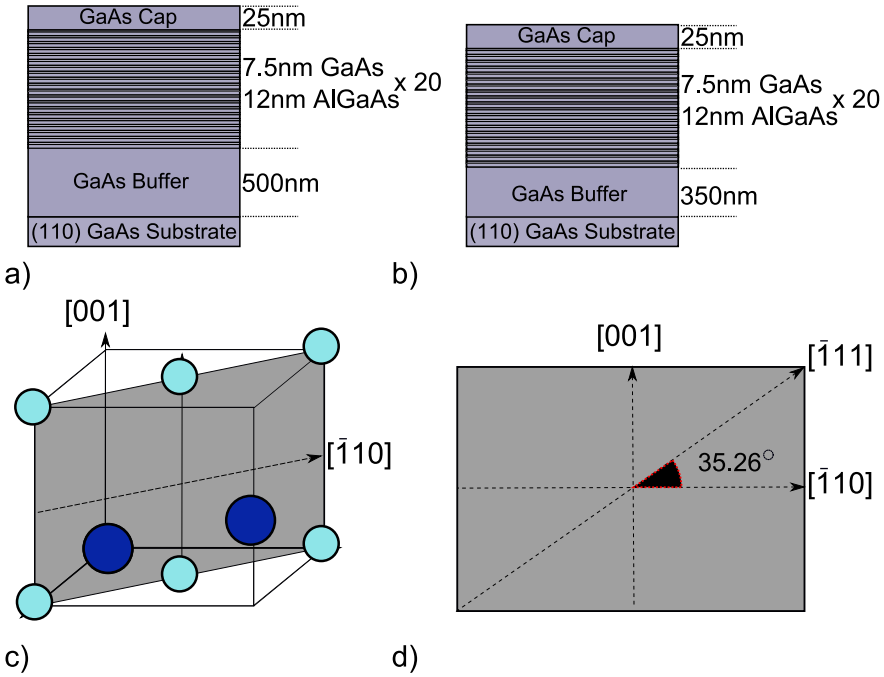

Figure 4.1: a) Sample NU2284. b) Sample NU2572. c) A schematic of the positions of the gallium (light blue) and arsenic (dark blue) atoms in the (110) crystal plane. d) The angles between different crystallographic directions in the (110) plane.

photoluminescence (PL) indicate successful quantum well growth with the expected confinement energy and therefore well width (see table 3.1). The design of the second sample NU2572 (figure 4.1b) was identical to NU2284 apart from a slightly thinner GaAs buffer layer (350 nm), however the position of the low temperature PL peak suggests the actual quantum wells grown were slightly narrower (5 nm).

The slight ionic component of the bonds in GaAs results in natural cleavage (breakage) in {110} planes[72]. Therefore a (110) quantum well will cleave along [001] producing a sample edge which is 90° to the plane of the sample. Whilst cleaving a (110) GaAs quantum well along the $[\bar{1}11]$ direction will leave an angle of 45° degrees to plane of the sample wafer. A study of both samples revealed at least two distinct cleaved edges along different crystallographic directions. From determination of two crystallo-

graphic directions it was possible to determine the angle between the plane of polarisation of the probe (parallel to the optical bench) and the principle crystallographic axes ($\langle 001 \rangle$ and $\langle \bar{1}10 \rangle$ directions).

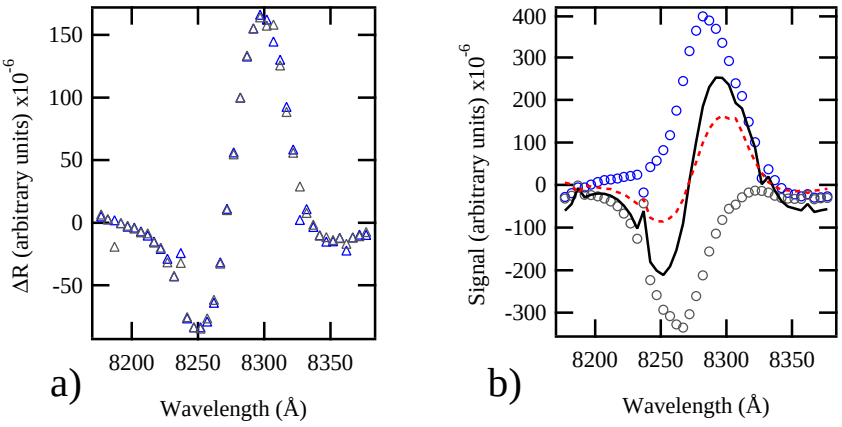

Figure 4.2: Measurements taken at a probe delay of 30 ps. a) ΔR for the two opposite circular polarisations of the pump (blue and grey) b) The $\Delta\theta$ for opposite polarisations of the pump (blue and grey circles), the sum of the two measurements (black line) and ΔR measurement (dashed red line).

4.2 Sample NU2284

4.2.1 Measurements at a fixed delay

Measurements of $\Delta\theta$ and ΔR were taken as a function of wavelength at a fixed probe delay of 30 ps as described in section 3.2.6. Figure 4.2a shows the variation in the ΔR signal for NU2284 as a function of wavelength ($\lambda = 8177 \rightarrow 8377$ Å) for two opposite circularly polarised pump beams at room temperature. The signals are identical consistent with the interpretation given in section 3.2.7, as the polarisation of the pump should not influence the number of excited carriers.

Figure 4.2b shows the $\Delta\theta$ signal as a function of wavelength for two opposite circular pumps. The change in the sign of the $\Delta\theta$ signal for opposite pump polarisations is a consequence of the different spin alignments resulting from the optical selection rules. However it can be seen the two signals peak at different wavelengths so they are not equal and opposite which means that a given population of σ_+ carriers produces a different probe rotation

from the same population of σ_- carriers.

Any non-identical nature to the $\Delta\theta$ measurements can be illustrated through the addition of the two signals (solid black line in 4.2b). This signal is non-zero and bears a striking resemblance to the ΔR signal (red dashed line) as would be expected for polarisation rotation induced by the photoexcited population.

A possible explanation of this effect is as follows. Since the sample has two-fold symmetry in the quantum well plane, it will have a birefringence in that plane. This would give rise to a rotation of the plane of polarisation of a reflected optical beam unless the incident polarisation coincides with one of the principle in-plane axes. Similarly, the effect of an excited population will be to induce a non-linear birefringence giving pump-induced rotation of the probe polarisation except when the probe plane coincides with one of the principle axes.

4.2.2 Rotational wavelength scans

To further explore this affect of the reduced rotational symmetry in the (110) plane, the sample was placed into a rotation mount, allowing the angle between crystal axes and the plane of polarisation of the probe to be changed. As before there was no difference between the ΔR measurements for opposite pump polarisations.

The $\Delta\theta$ measurements for the opposite pump polarisations as the sample was rotated are shown in Figure 4.3. The peak positions for the two polarisations vary with the angle and at certain angles the two $\Delta\theta$ measurements become (nearly) mirror images reflected in the $\delta\theta = 0$ line(4.3a and c). This can be seen through the variation in the sum $(\Delta\theta_{\sigma_+} + \Delta\theta_{\sigma_-})$ given by the black line; for certain angles the sum is nearly zero whilst at other angles the sum is large. As the sample was rotated beyond the angle where the black line is nearly zero ($87\,^\circ$) the signal returns but this time with the opposite sign (cf. figures 4.3b and d). These results confirm that this non-linear optical anisotropy is of crystallographic origin.

Measurements were taken on NU2284 for an entire revolution of the sample and of particular interest were the angles at which the sum of the two $\Delta\theta$ signals vanished. For at these angles the probe polarisation should coincide with the principle axes in the quantum well plane.

To determine the angles at which the two $\Delta\theta$ signals were identical, the

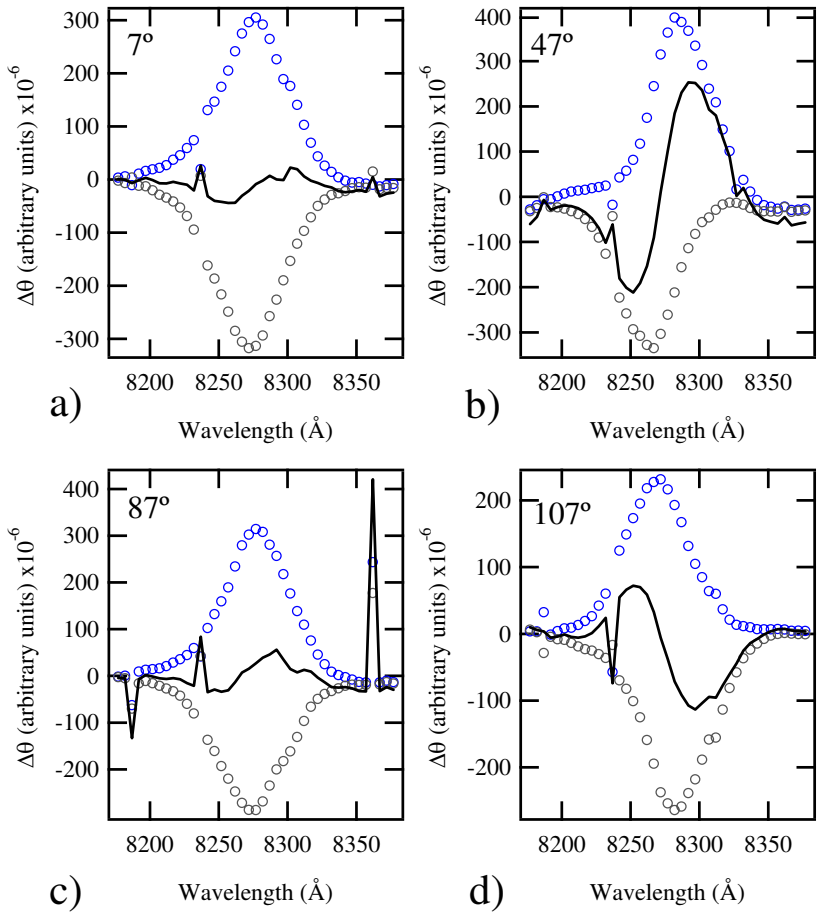

Figure 4.3: The $\Delta\theta$ measurements for opposite circular pumps (blue and grey) for NU2284 as the sample is rotated. The angles correspond to the orientations of the plane of polarisation of the probe to $\langle 001 \rangle$ and the black line is the sum of the two signals. The spikes in the signals are wavelengths where the modelocking of the MIRA was lost and started operating in CW.

position of the $\Delta\theta$ peak signal for both polarisations were calculated and the difference between the two is shown as points in figure 4.4 with a sinusoidal fit (solid line). As can be seen by where the fitted function goes to zero, the angles at which there is no spin-independent rotation of the probe do indeed correspond to when the polarisation of the probe beam is aligned with one of the principle crystallographic axes, the (001) or $(\bar{1}10)$.

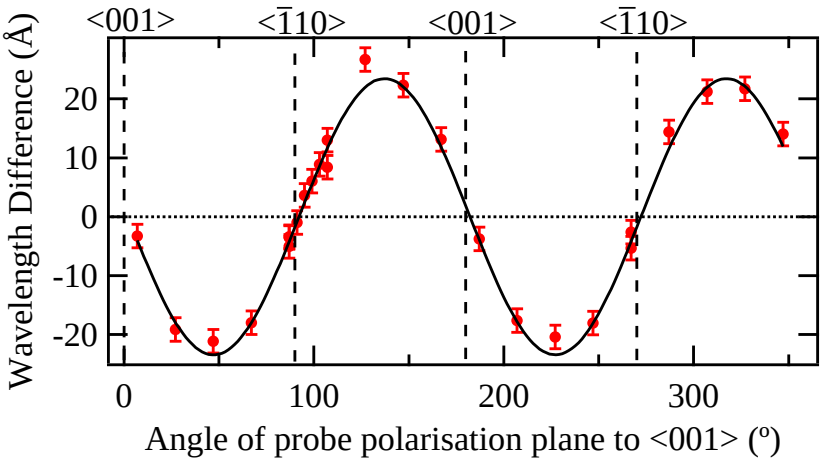

Figure 4.4: The difference in wavelength between the two $\Delta\theta$ peak positions for different rotations of the sample fitted with a $A\sin(fx+\phi)$ function.

4.3 Sample NU2572

In order to determine whether this phenomenon was a unique feature of a single (110) sample, a second (110) quantum well sample (NU2572) was investigated. As before, the sample was placed into a rotation mount and measurements were taken every 20 ° for an entire revolution of the sample.

4.3.1 Rotational wavelength scans

Figure 4.5 shows the $\Delta\theta$ measurements for different rotations of the sample. The variation in $\Delta\theta$ with wavelength is more complicated; this time the measurements contain both maxima and minima that shift with angle. As before the sum of the two $\Delta\theta$ signals (black line) varies in magnitude, going to zero at certain angles and then changing sign. As the variation in $\Delta\theta$ with wavelength was more complicated than in NU2284, a different approach was taken to locate the angles where the $\Delta\theta$ measurements for the opposite pump polarisations were equal and opposite.

As the sum signal $(\Delta\theta_{\sigma_+} + \Delta\theta_{\sigma_-})$ appears to imitate the ΔR signals the following procedure was adopted to identify the angle of the probe polarisation giving zero additional rotation. A computer code was written that first multiplied the sum signal by a constant and then subtracted an offset. The code then calculated the difference between this altered sum signal and the

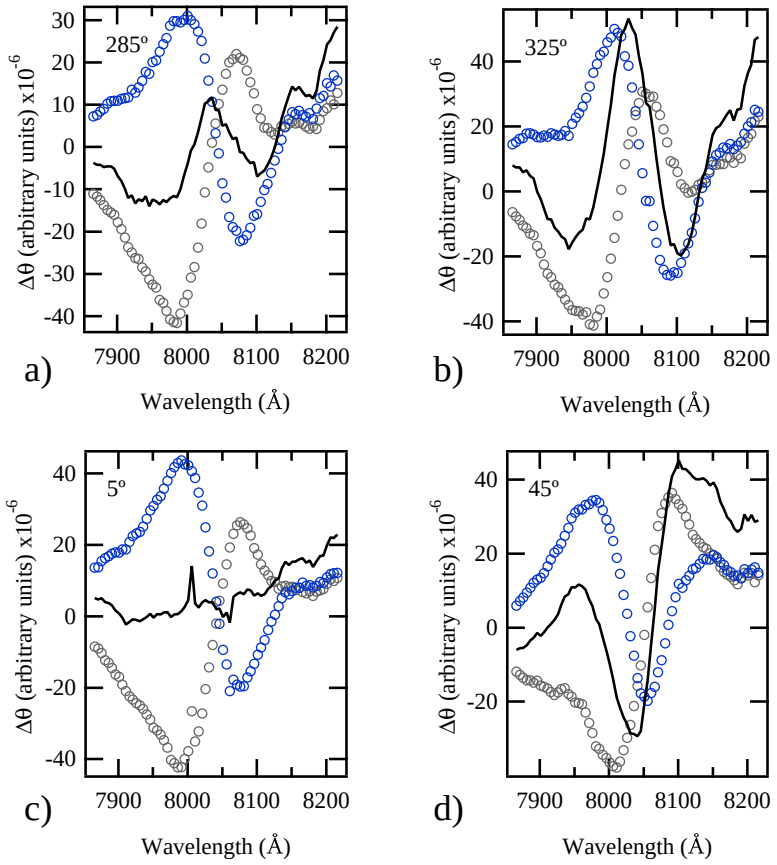

Figure 4.5: $\Delta\theta$ measurements (blue and grey) for different orientations (angles) of the plane of polarisation of the probe and the sum of the two signals (black) for NU2572.

ΔR at each wavelength and computed the sum of the absolute magnitudes of the differences to get a number representing how well the sum signal was fitted to the ΔR. The number determined for each value of multiplication and offset constants were recorded into a matrix with columns and rows of the matrix corresponded to the different values of constants.

Figure 4.6a shows the result of the fit for one angle and a 2D plot of the corresponding matrix. The red on the 2D plot corresponds to the low numbers in the matrix, and it can be quite easily seen that there is a minimum in the matrix corresponding to where the sum signal has been successfully fitted to the ΔR.

When there is no spin-independent rotation of the probe, the sum signal

will be very small, and the constant of multiplication (horizontal position of the minimum in figure 4.6b) will tend to infinity. Figure 4.6c shows the inverse of the multiplication constant for different angles with a $A\sin(fx+\psi)$ fitting function. Again, within the error the angles where there is no spin-independent rotation of the probe correspond to when the polarisation of the probe is aligned with one of the principle crystallographic axes. This result agrees with the conclusion from the first sample, NU2284.

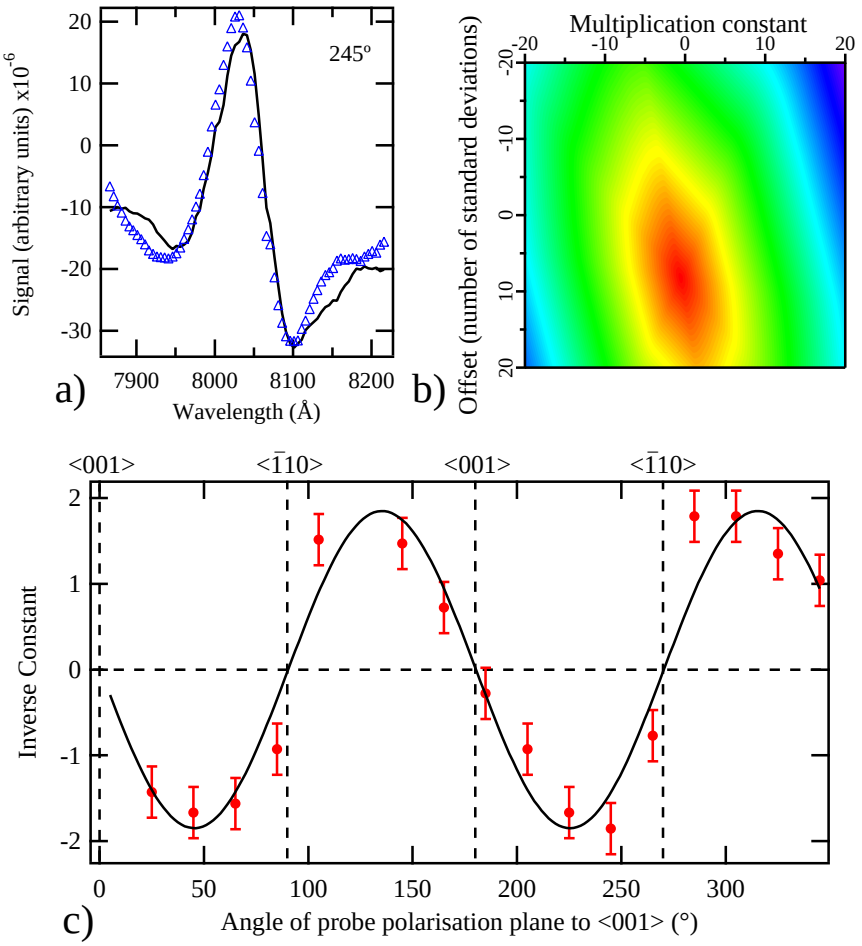

Figure 4.6: a) The fitting of the sum signal (black line) to the ΔR (blue triangles). b) The matrix in which each element corresponds to the difference between the ΔR and the fitted sum signal for different values of the constant and the offset. c) The reciprocal of the multiplication constant determined with the method described for different angles of the probe polarisation.

4.4 Measuring spin relaxation

An investigation into the effect of this optical anisotropy on measurement of the spin relaxation time was carried out on NU2284 at 300 K. Figure 4.7a shows normalised time-resolved ΔR measurements for the polarisation of the probe both parallel (open circles) and 45 ° (solid squares) to $\langle\bar{1}10\rangle$. The temporal evolution of the two measurements are identical, reconfirming the previous observation that the anisotropy does not affect the ΔR signal.

Figure 4.7b shows normalised time-resolved $\Delta\theta$ measurements taken with the probe polarisation parallel to (open circles) and at 45 ° to (open squares) $\langle\bar{1}10\rangle$. The two measurements clearly have different temporal dynamics, the $\Delta\theta$ measured with the polarisation parallel to $\langle\bar{1}10\rangle$ decaying more quickly. As the corresponding ΔR measurements decay at the same rate (figure 4.7a), the calculated spin relaxation times (equation 3.1) will be different. This presents a problem as aligning the probe polarisation to one of the principle crystallographic axes for every (110) sample will be difficult as samples do not always have two distinct cleaved edges along different crystallographic directions. Ideally a methodology should be developed that would allow accurate spin relaxation measurements to be taken at arbitrary orientations of the crystal axes.

Assuming the additional rotation of the probe is independent of the pump polarisation, it should be possible to remove the rotation by subtracting one $\Delta\theta$ from the other. The temporal dynamics for $(\Delta\theta_{\sigma_+} - \Delta\theta_{\sigma_-})$ measured with the probe 45 ° to $\langle\bar{1}10\rangle$ is shown by the solid grey circles in figure 4.7b. This signal matches the $\Delta\theta$ measurement taken when the probe polarisation was parallel to $\langle\bar{1}10\rangle$. The two decay times agree and therefore the calculated spin relaxation times will be the same.

In the same way as before, if the two $\Delta\theta$ measurements for opposite pump polarisations are summed together, the additional rotation of the probe can extracted. Figure 4.7c shows the two ΔR measurements for the two opposite pump polarisations with the probe polarisation 45 ° to $\langle\bar{1}10\rangle$. The sum of the $\Delta\theta$s for different pump polarisations (solid red circles) is also plotted on figure 4.7c. It is apparent that the population decay (ΔR) is very similar to decay of the sum signal and the two decay times are nearly identical. There is a slight discrepancy but large errors in decay times are not uncommon in data with long decay times. The evidence suggests that

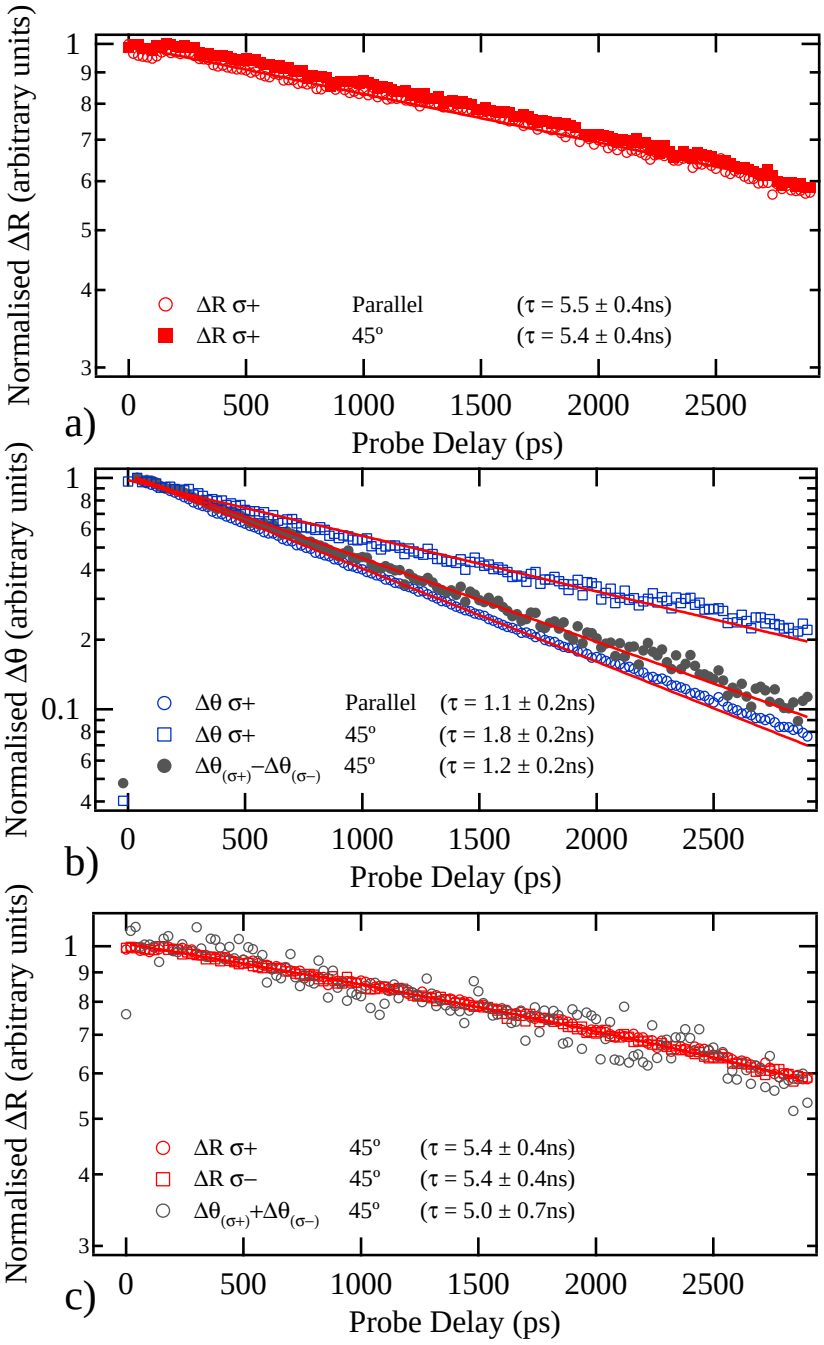

Figure 4.7: Time-resolved measurements for the plane of polarisation of the probe both parallel and 45 ° to $\langle \bar{1}10 \rangle$ normalised at zero delay. a) ΔR measurements. b) $\Delta\theta$ measurements and the time evolution of $\Delta\theta_{\sigma_+} - \Delta\theta_{\sigma_-}$. c) ΔR at the same angle for opposite pump polarisations compared with $\Delta\theta_{\sigma_+} + \Delta\theta_{\sigma_-}$.

the spin independent rotation of the probe decays at the same rate as the pump-induced population.

4.5 Interpretation

This spin independent rotation of the probe can be understood by considering the effect of crystal anisotropy on the polarisation of the reflected light. Quantum wells grown on (110) substrates have orthorhombic symmetry C_{2v} and the non-linear optical properties are in principle anisotropic. For a near-normal incident linear polarised beam with the plane of polarisation matching a principle crystallographic axes and the x, y, z axes to correspond to the [001],[$\bar{1}$10],[110], the refractive index for a given direction (i) can be calculated from the relative dielectric tensor

$$\epsilon = \begin{pmatrix} \epsilon_{001} & 0 & 0 \\ 0 & \epsilon_{\bar{1}10} & 0 \\ 0 & 0 & \epsilon_{110} \end{pmatrix} \tag{4.1}$$

using $n_i = \sqrt{\epsilon_i}$. CW experiments have measured different values for the dielectric function along the [001] and [$\bar{1}$10] directions[70, 71]. The resulting refractive index would mean in the absence of the pump, for a linearly polarised probe beam with an incident polarisation either [001] or [$\bar{1}$10] the reflected polarisation will be unchanged. For other incident orientations the reflected polarisation will be rotated and elliptised depending on the real and imaginary parts of the refractive indices for the [001] or [$\bar{1}$10] axes. In principle, with the pump present, the excited population will alter the refractive index components differently causing pump-induced changes in the polarisation and elliptisation. To a first approximation extra terms appear in the dielectric tensor that depend linearly on the photoexcited population n_{ex}, for example $n_{ex}(\partial\epsilon_{001})/(\partial n_{ex})$ and $n_{ex}(\partial\epsilon_{\bar{1}10})/(\partial n_{ex})$. These extra terms are not equal because $\epsilon_{001} \neq \epsilon_{\bar{1}10}$ and result in a pump induced change in the polarisation of the probe that goes away when the polarisation of the probe matches one of the crystallographic axes. These pump induced polarisation rotations, which are independent of the spin polarisation, have been shown to decay at the population decay rate, which is generally slower than the spin polarisation decay rate. Therefore, when the spin polarisation lifetime is considerably shorter than the population lifetime, the effect of the

pump-induced polarisation rotation on the $\Delta\theta$ signal will be very small.

4.6 Conclusion

The reduced symmetry of the (110) crystal plane results in an additional rotation of the probe not observed in (100) quantum wells. This additional rotation is caused by the pump induced population of carriers and decays at the same rate. Therefore using the traditional time-resolved Kerr rotation technique different spin relaxation times will be measured for different orientations of the sample. By adapting the time-resolved Kerr rotation technique to incorporate measurements with both circular polarisations, a reliable measure of the spin lifetime can be obtained. This technique was employed in the following two chapters where measurements of spin relaxation times in (110) quantum wells are presented.

Chapter 5

Effect of an Electric Field

The large spin-orbit interaction in GaAs allows measureable changes in electron spin dynamics to be produced when an electric field is applied normal to GaAs heterostructures[25, 73]. This chapter is a study into the effect of an electric field on electron spin relaxation in (110) GaAs quantum wells between 80-230 K. By combining the measured spin relaxation times with electron scattering times measurements it was possible to provide the first direct measurement of the strength of the Rashba spin-orbit interaction in GaAs quantum wells under the application of an electric field.

5.1 Determining the Rashba coefficient

The magnitude of the conduction band spin splitting in a heterostructure for a particular electric field is determined by the Rashba coefficient. In (100) GaAs quantum wells, the presence of the bulk inversion asymmetry (BIA) precession vector in the plane complicates the measurement of the Rashba spin-orbit interaction and only their relative sizes have been determined for such samples[17, 19, 23].

As shown in chapter 2, the BIA effective magnetic field in (110) GaAs quantum wells is perpendicular to the quantum well plane. This means for electron spin aligned normal to the plane; there will be no BIA induced Dyakonov-Perel spin relaxation[58]. Accordingly long spin lifetimes have been measured in (110) quantum wells that are no longer limited by the Dyakonov-Perel spin relaxation mechanism[16, 25, 74].

When an electric field is applied normal to a (110) quantum well, the

resulting SIA effective magnetic field is in the plane and for electron spin aligned perpendicular causes Dyakonov-Perel spin relaxation. The effective magnetic field produced by such an electric field is given by

$$\mathbf{\Omega_{SIA}} = \frac{e}{\hbar}\alpha\langle\epsilon_z^v\rangle \begin{pmatrix} k_y \\ -k_x \\ 0 \end{pmatrix} \tag{5.1}$$

where e is the electron charge, $\hbar$ is reduced Planck constant and $\langle\epsilon_z^v\rangle$ is the expectation value of the valence band electric field for conduction electrons (see section 2.4.2 where appropriate references are cited). The constant α is known as the Rashba coefficient. It has the dimensions of length squared (see appendix B) and a rough equivalence to the Landé g-factor. In the presence of strong scattering, the Dyakonov-Perel spin relaxation rate is

$$\frac{1}{\tau_s} = \langle\Omega_\perp^2\rangle\tau_p^*. \tag{5.2}$$

As there is no component of the BIA spin precession vector perpendicular to the spin alignment, one can substitute Ω_{SIA} into the equation above to give

$$\frac{1}{\tau_s} = \frac{e^2}{\hbar^2}\alpha^2\langle\epsilon_z^v\rangle^2\langle k_{xy}^2\rangle\tau_p^* \tag{5.3}$$

where $\langle k_{xy}^2\rangle$ is thermal average of the in-plane wavevector squared. For thermalised electrons in undoped quantum wells, this average can be estimated through assuming a Boltzmann distribution

$$k_BT = \frac{\hbar^2\langle k_{xy}^2\rangle}{2m_e}. \tag{5.4}$$

Rearranging this for $\langle k_{xy}^2\rangle$ and substituting into equation 5.3 gives

$$\frac{1}{\tau_s} = \frac{e^2}{\hbar^2}\alpha^2\langle\epsilon_z^v\rangle^2\left(\frac{2m_ek_BT}{\hbar^2}\right)\tau_p^* \tag{5.5}$$

$$\alpha = \frac{\hbar^2}{e\langle\epsilon_z^v\rangle}\frac{1}{(2m_ek_BT\tau_p^*\tau_s)^{1/2}}. \tag{5.6}$$

For a given electric field and temperature, if both the electron scattering and spin relaxation times are known the Rashba coefficient can be determined.

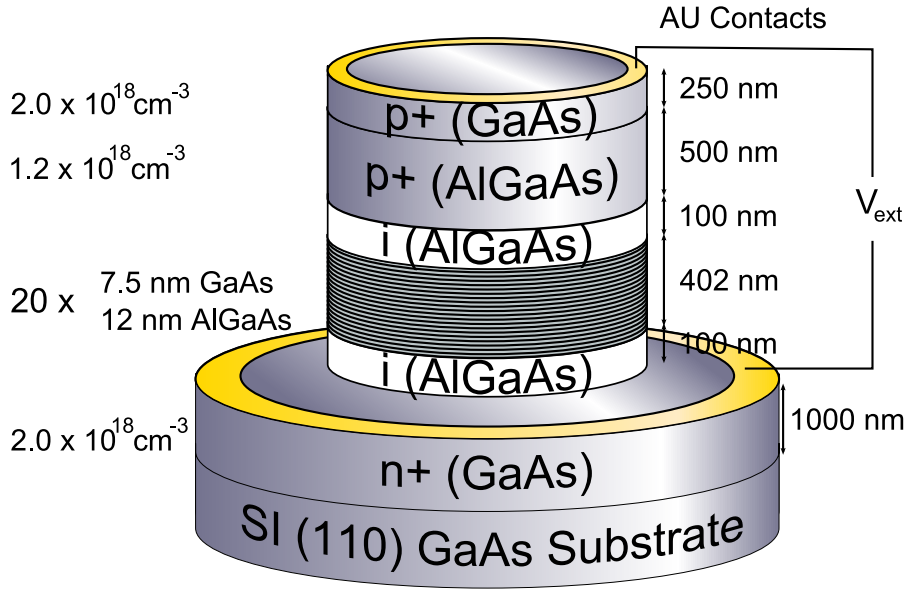

Figure 5.1: The processed p-i-n device studied (NU2307), where n^+ and p^+ signify degenerate semiconductor layers. The quantum wells were grown in the intrinsic region of the wafer. The electric field was applied by biasing the gold contacts located at the top and the bottom of the device.

5.2 Sample NU2307

The sample studied in this chapter was NU2307 (figure 5.1). The multi-quantum well region was made up of 20 repeats of a GaAs 7.5 nm quantum well and a 12 nm $Al_{0.4}Ga_{0.6}As$ barrier. The quantum wells were grown into the intrinsic (i) region of a p-i-n structure deposited onto a semi-insulating (SI) (110)-oriented GaAs substrate. The sample was fabricated into mesa devices 400 μm in diameter with annular gold contacts on the top and a gold grid at the base of each device. The top annular gold contact allowed optical access to the quantum wells. Optically injected carriers in the quantum wells could be subjected to an electric field through the application of a voltage (V_{ext}) across the top and bottom contacts.

5.2.1 Electric field calculation

The electric field experienced by carriers in the quantum wells was a result the built-in electric field arising from the doping ($\epsilon_{built-in}$) and the externally applied electric field (ϵ_{ext}) from the voltage (V_{ext}) across the contacts. The

built-in electric field can be calculated by from the difference of the Fermi energy (E_F) in the n-doped GaAs and the p-doped AlGaAs regions and their distance apart. The values of E_F relative to the energies of the conduction (E_C) and valence bands (E_V) for degenerate electrons and holes are[72]

$$E_F - E_C \simeq k_B T \left[\ln \frac{n}{N_C} + 2^{-3/2} \frac{n}{N_C} \right] \tag{5.7}$$

$$E_V - E_F \simeq k_B T \left[\ln \frac{p}{N_V} + 2^{-3/2} \frac{p}{N_V} \right] \tag{5.8}$$

where N_C, N_V are the effective density of states in the conduction and valence bands whilst p, n correspond to the doping concentrations in the p^+ and n^+ doped materials. The energy drop across the intrinsic region is given by (see appendix C)

$$\phi = E_G^{AlGaAs} - \Delta E_C + (E_F - E_C)^{GaAs} + (E_V - E_F)^{AlGaAs} \tag{5.9}$$

where ΔE_C is the AlGaAs/GaAs conduction band discontinuity. Once this energy has been calculated, the built-in field is given by the potential drop divided by the thickness of the intrinsic region (l) giving a total field ϵ_{total}

$$\epsilon_{total} = \epsilon_{built-in} - \frac{V_{ext}}{l} = \frac{\phi/e - V_{ext}}{l} \tag{5.10}$$

where the minus in front of the external voltage accounts for the fact that when in reverse bias the electric field increases. The temperature dependence of equations 5.7,5.8 and the band gap of AlGaAs will result in a variation of the built in electric field with temperature, being 30 kV/cm at 80 K and decreasing to 27 kV/cm at 300 K.

5.2.2 I-V measurements

Figure 5.2 shows a current voltage (I-V) measurement taken on the p-i-n device at 170 K shown in figure 5.1 both under illumination of 400 μW of laser light with wavelength of 806 nm (blue dots) and in the dark (black dots). In the dark the device exhibits typical diode behaviour with no current in reverse bias and an exponential increase in the current in forward bias. Under illumination there is an increase in the current with increasing reverse bias with a current of 1 μA at -3 V. It is important for interpretation

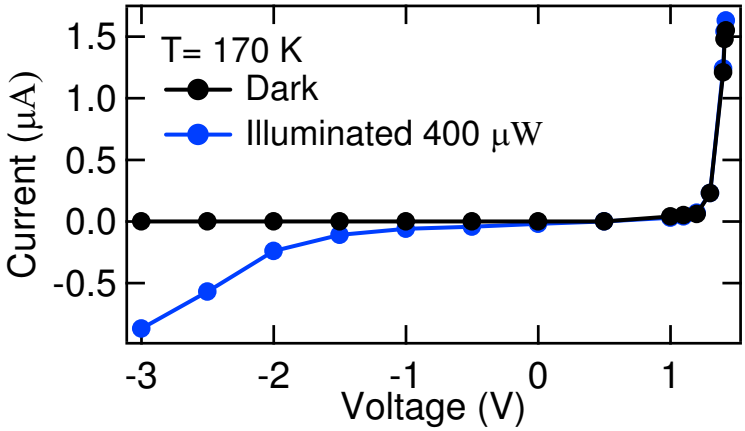

Figure 5.2: The current voltage measurement at 170 K. In the dark the p-i-n device behaves like a diode with an exponential increase in the current in forward bias and no current in reverse. Under illumination, the forward bias behaviour is very similar however in reverse bias there is an increase in the current.

of the time-resolved Kerr measurements that this current represents a small number of the total photoexcited carriers. The number of photoexcited carriers generated in the quantum well region per second under experimental conditions can be estimated with

$$N_{ex} = \frac{(1 - R_{glass})^6 (1 - R_{GaAs})(1 - e^{-\alpha x})P}{hf} \tag{5.11}$$

where R is the reflectance (for an incident angle of 7 ° R_{glass}=0.04 (for fused quartz) and R_{GaAs}=0.3 [75]), x is the optical path length in the quantum wells (∼0.4 μm), α is the absorption coefficient for GaAs quantum wells (α=10^4 cm^{-1}[76]), f is the frequency of the light and P is the power of illumination. The first term $(1 - R_{glass})^6$ takes into account the loss of power due to the reflection from each face of the three cryostat windows. Using this equation the number of carriers excited per second for laser light of power 0.4 mW and a wavelength of 806 nm is 2.9×10^{14}. The ratio of the number of carriers swept away in the leakage current (N_{lc}) to the number of excited carriers (N_{ex}) at -3 V is

$$\frac{N_{lc}}{N_{ex}} = \frac{1 \times 10^{-6}/1.6 \times 10^{-19}}{2.9 \times 10^{14}} = \frac{6.3 \times 10^{12}}{2.9 \times 10^{14}} = 0.021 \tag{5.12}$$

So the leakage current accounts for only 2% of the total number of optically injected carriers. At room temperature, where carrier confinement is not as strong, there was a significantly higher current in reverse bias that restricted spin measurements to the temperature range 80-230 K.

This calculation of the number of carriers escaping the wells is likely to be an overestimate as the shape of the I-V in reverse bias is suggestive of the avalanche effect. In the presence of high electric fields, electrons can be accelerated to sufficient kinetic energies to cause ionisation of atoms upon scattering releasing further electrons. As this would lead to the amplification of current the calculation above is an upper limit for the percentage of photoexcited carriers escaping the quantum wells.

5.3 Electric field effects

As spin relaxation times were measured for different applied voltages that were then converted to electric field (section 5.2.1), one would ideally like experimental verification of the electric field actually present. Two phenomena displayed by the sample provided the potential for this verification. These are the quantum confined Stark effect and resonant tunnelling between adjacent wells.

5.3.1 Quantum confined Stark effect

When an electric field is applied normal to a quantum well there should be a shift of the energy states in the quantum wells to lower energies as a consequence of the quantum confined Stark effect (QCSE)[77, 78, 79]. Figure 5.3 shows the change in the $\Delta\theta$ and the ΔR signals as a function of wavelength at a fixed delay of 20 ps for increasing applied voltage at 130 K. With increasing voltage both signals move to longer wavelengths, consistent with the effect of an electric field. The $\Delta\theta$ and the ΔR signals become smaller at higher electric fields as the electron and hole wavefunction overlap and therefore the absorption coefficient is reduced.

However, this change in absorption complicates the refractive index of the material and the ability to fit the shift in the peaks of the signals displayed in figures 5.3a and b to the conventional QCSE energy shift[80, 81]. As observed resonant tunnelling enabled verification of the electric field (see next section), the QCSE in reflection was not explored further in this work.

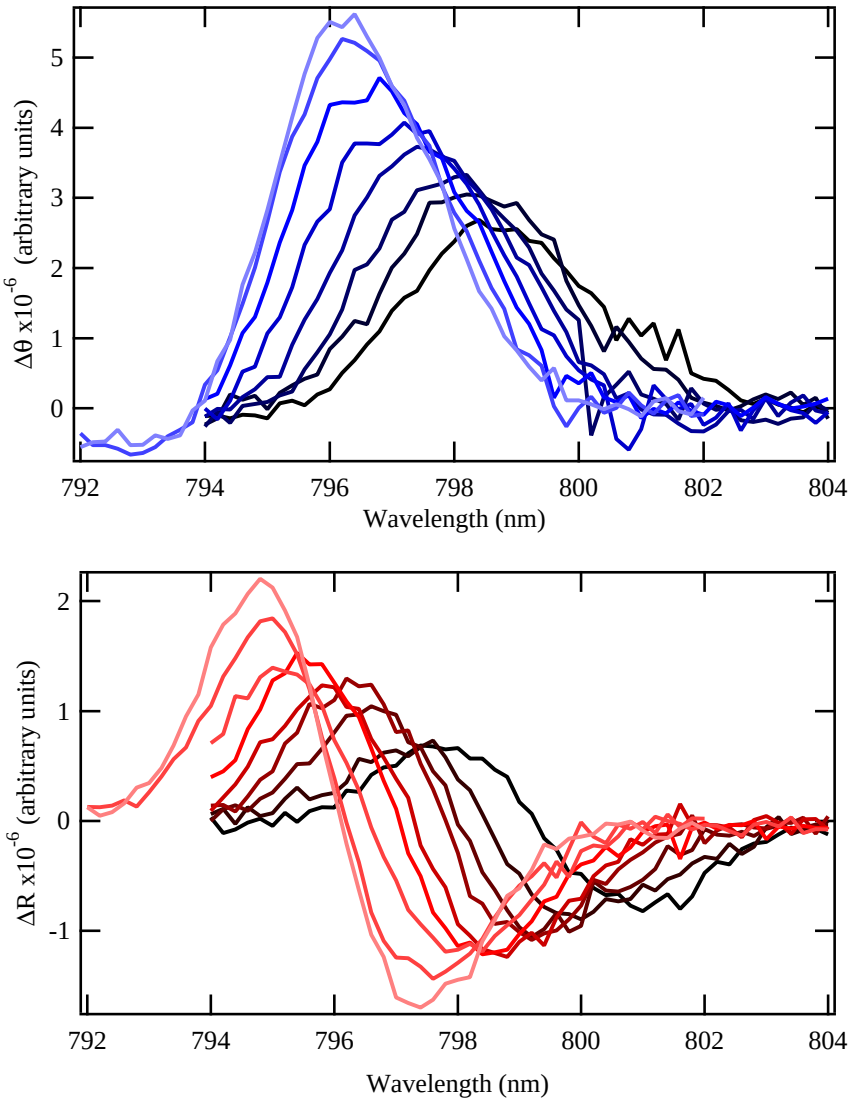

Figure 5.3: Measurements taken at 130 K and 20 ps delay. a) $\Delta\theta_{\sigma+} - \Delta\theta_{\sigma-}$ and b) $\Delta R_{\sigma+} + \Delta R_{\sigma-}$ as a function of wavelength for different applied voltages (0 V for lightest lines and 3 V for darkest). The shift to longer wavelengths with increasing voltage for both signals is consistent with the quantum confined Stark effect.

5.3.2 Resonant tunnelling

The eigenvalues of the Schrödinger equation for electrons and holes confined to a 7.5 nm GaAs/AlGaAs quantum well are shown schematically in figure 5.4a. The energy difference between the n=1 and n=2 conduction states is $E_{12} = 0.146$ eV. As the barriers between the wells have finite thickness, at a particular electric field the n=1 state will be resonant in energy with the n=2 state of a neighbouring well. When the states are resonant there is enhanced probability of an electron tunnelling from one well into the neighbouring well and depending on the barrier thickness this may be detectable in the I-V characteristic under illumination. The electric field at which this resonance occurs is for this particular sample given by

$$\epsilon_{tunnel} = \frac{E_{12}(eV)}{L_W + L_B} = \frac{0.146\ eV}{19.5 \times 10^{-9}\ m} = 7.5 \times 10^6\ V/m = 75\ kV/cm \quad (5.13)$$

where $L_W + L_B = 19.5$ nm and is the distance between the centres of two neighbouring wells. At this electric field there would be an increased number of electrons tunnelling towards the n-doped GaAs which would contribute to an increase in the current.

To search for such resonant tunnelling the following procedure was adopted. The p-i-n device was illuminated with light from the MIRA that was tuned from short to long wavelengths in 0.2 nm steps and for each wavelength the current was recorded for voltages from -4 V (94.4 kV/cm) to +1 V (11.4 kV/cm). The search covered a wavelength range centred on the PL peak at a given temperature. The data for 170 K is shown in figure 5.4b. The red area at high fields (90 kV/cm) is uniform across the different wavelengths; however between 75-80 kV/cm there is an increase in the current between 805-807 nm. This is strongly suggestive of resonant tunnelling of photoexcited carriers and to enhance the data the I-V measurement taken at the longest wavelength (810 nm) and thus furthest off optical resonance with the n=1 quantum well transition was subtracted from the other I-V measurements. The result plotted in figure 5.4c shows a clear increase in the current that is resonant in both wavelength and electric field. The peak occurs at 75 kV/cm and 805.4nm in excellent agreement with the electric field calculated in equation 5.2.1. The occurrence of the quantum tunnelling of electrons at the expected electric field 75 kV/cm provides experimental support that for other bias voltages the electrons experienced the electric

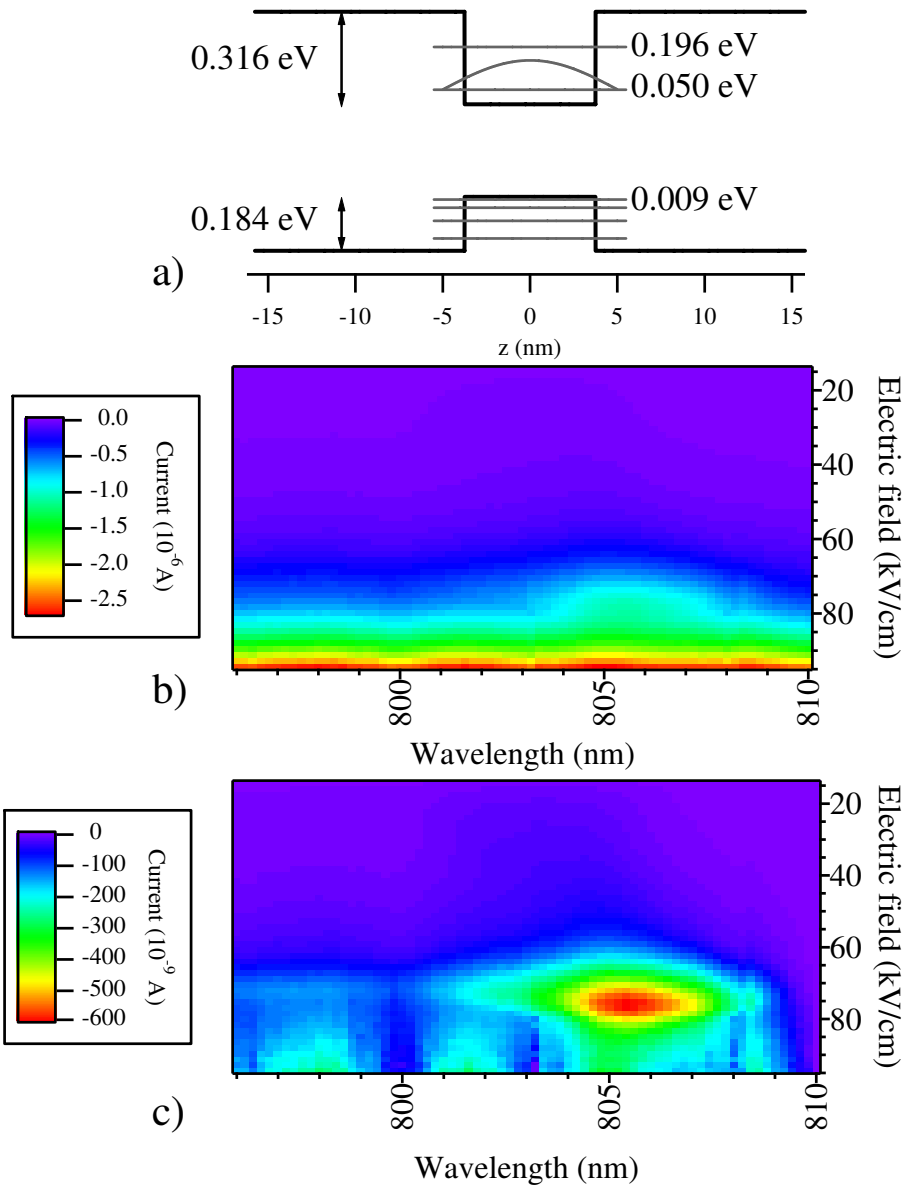

Figure 5.4: a) The energy levels in a 7.5 nm GaAs/AlGaAs quantum well, calculated by numerically solving the Schrödinger equation. b) I-V measurements at 170 K of the p-i-n device whilst under illumination of 300 μW of light for different wavelengths. c) As in b) but with the measurement taken at 810 nm used as a background and subtracted from the data to emphasise any resonance effects. The oscillatory variation of the current with wavelength at high electric fields is a residual result of variation in the output power of the MIRA with wavelength.

field calculated as in section 5.2.1.

In figure 5.4b, the current at the resonance of around 1.5 μA now corresponds to an upper limit of around 4% of the total photoexcited carriers. Although this is likely to be an overestimate due to the presence of avalanche multiplication, it is still a very small fraction. In the following section measured spin lifetimes at around 75 kV/cm are very short ($\sim$ 50 ps) whilst recombination times are around 2 ns. The carriers that tunnel most likely correspond to electrons that have already lost their spin polarisation and then subsequently recombine or are collected as current before the next laser pulse arrives (13 ns). Therefore it is assumed that this tunnelling will not affect the measured spin relaxation times at this electric field.

5.4 Measuring the Rashba coefficient

5.4.1 Spin lifetimes

Previous measurements[25] on NU2307 revealed a power dependence of the electron spin lifetime and also that at small electric fields the spin lifetime is limited by a mechanism other than electric field induced Dyakonov-Perel relaxation. Therefore to minimise the influence of other spin relaxation mechanisms, measurements were taken at low power (pump 400 μW and probe 20 μW) between $\sim$27-80 kV/cm where electron spin lifetimes are believed to be limited by electric field induced Dyakonov-Perel spin relaxation[82].

Time-resolved measurements of $\Delta\theta$ and ΔR at different applied voltages were taken whilst changing the wavelength to follow the energy shift of the signals (section 5.3.1). Figure 5.5a shows the effect of the applied voltage on the temporal dynamics of the $\Delta\theta$ signal at 200 K. All signals are monoexponential and there is a clear increase in the relaxation rate for increasing voltage. At -3 V (79 kV/cm) the $\Delta\theta$ lifetime is around 50 ps, and increases to 750 ps at 0V (28 kV/cm). This is consistent with an increase in the Rashba spin-splitting interaction with increasing electric field (equation 5.1).

Figure 5.5b shows the corresponding ΔR signals with different y-offsets for each measurement for clarity. All the ΔR measurements have decay times of over 2 ns indicating that the calculated spin lifetimes will be only slightly different from the $\Delta\theta$ decay times. There is little change in the ΔR decay time with applied field. For purely radiative recombination one would

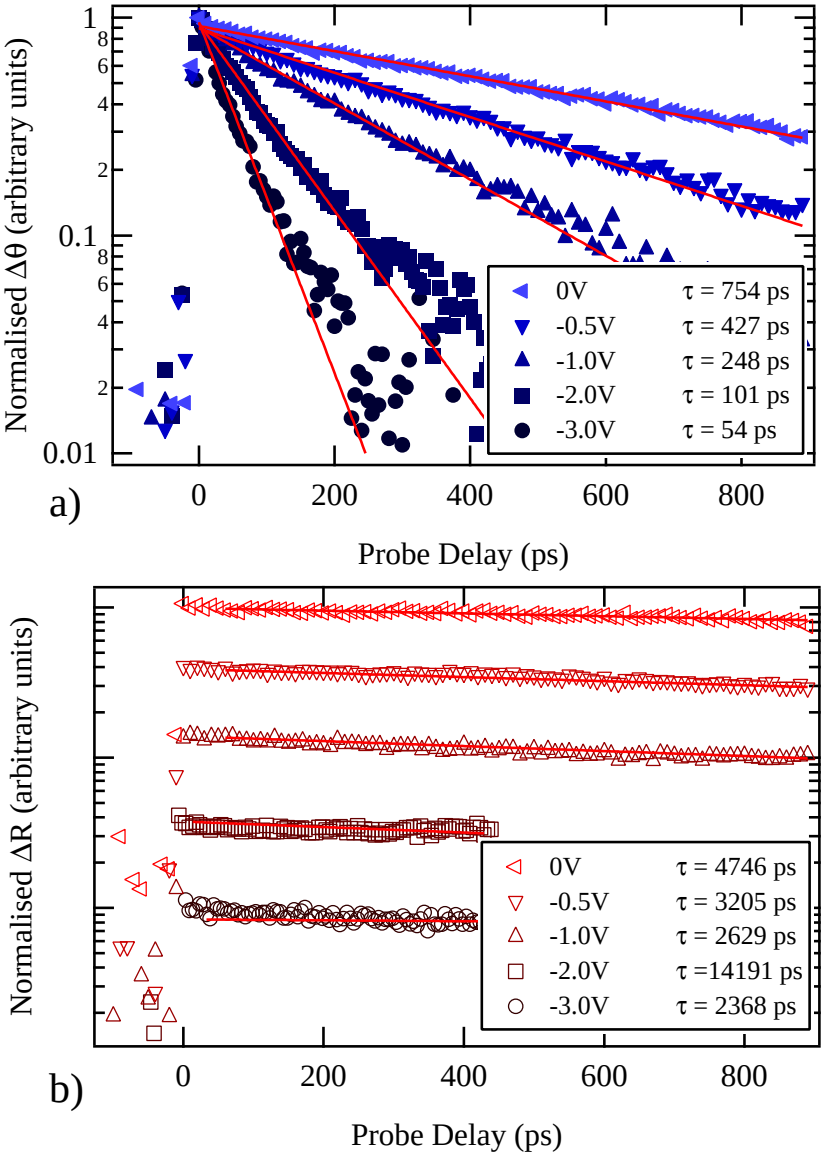

Figure 5.5: a) The variation in the time-resolved $\Delta\theta$ signal for different applied voltages at 200 K. There is a clear decrease in the decay time with increasing voltage. b) The corresponding ΔR measurements for 200 K for different voltages offset for clarity. There is no obvious change in the recombination time with increasing voltage. The ΔR decay time for each voltage is much longer than the $\Delta\theta$ decay time. Measurements at -3 V and -2 V were only taken up to 450 ps delay as the $\Delta\theta$ signal had fully decayed at this delay so further points at later delays were not necessary.

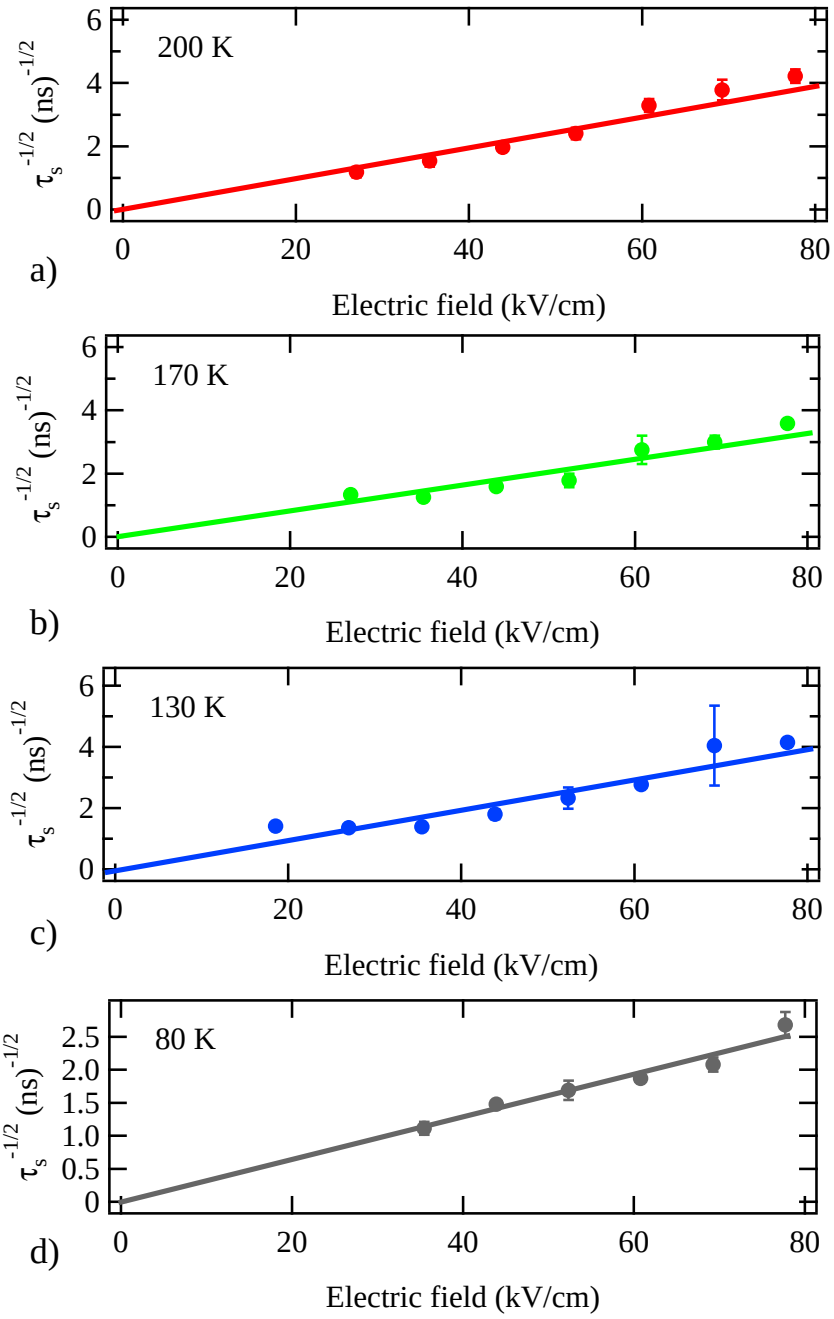

Figure 5.6: a) The spin lifetimes calculated by combining the $\Delta\theta$ and ΔR measurements at 200 K. The solid line is a straight line fit to the data. Measurements at lower temperatures are shown in b)-d).

expect a longer decay time at high fields due to the reduced electron and hole wavefunction overlap. The observed behaviour may therefore indicate the existence of a non-radiative decay pathway.

From equation 5.5 it can be seen that at a given temperature the spin relaxation rate should depend linearly on the electric field squared assuming that the electron mobility is field-independent. As verification, the square root of the spin relaxation rate at a range of temperatures is plotted against the calculated electric field in figure 5.6. The experimental points fit well to a straight line fit going through the origin. This indicates that it is indeed an increase in the Dyakonov-Perel spin relaxation mechanism that limits the spin lifetime at high electric fields. It also indicates that there is no field-independent component of spin-splitting which gives Dyakonov-Perel spin relaxation.

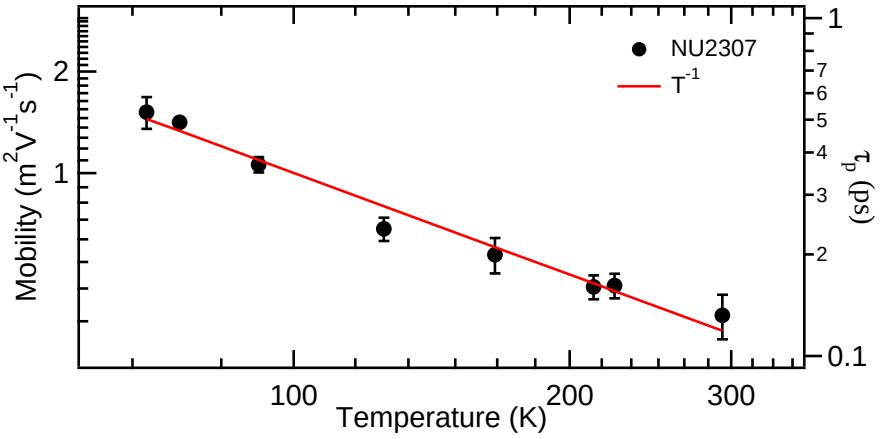

Figure 5.7: a) The calculated mobility and electron scattering times by combining the spin relaxation and transient spin grating measurements. The solid red line is the best fit with temperature.

5.4.2 Mobility

The second ingredient needed for determining the Rashba coefficient (equation 5.6) is the electron scattering time for each temperature. This was measured using a transient spin grating technique in Cambridge (see section 3.3). The sample studied was a piece of the NU2307 wafer that was not fabricated into p-i-n mesas and therefore the electron scattering time was

obtained at the built-in field ($\sim$ 28 kV/cm).

Figure 5.7 shows the mobility and corresponding electron scattering time across the temperature range. The variation with temperature is indicative of a mobility limited by phonon scattering. A two-dimensional electron system that is non-degenerate, would have a T^{-1} dependence on temperature [83]. The solid line is a best fit assuming a T^{-1} temperature dependence and clearly gives a very good representation of the data.

It is assumed that a transverse electric field will have little effect on the in plane mobility and electron scattering time. One mechanism by which the transverse electric field might alter the electron mobility is through increased contact with the interfaces at high electric fields which might increase defect scattering. This effect should be extremely small in the temperature range investigated since scattering has been observed to be predominantly due to phonons.

5.4.3 Combining the measurements

The Rashba coefficient was calculated using the straight line fit of the square root of the spin relaxation rate against the electric field for each temperature (figure 5.6). The best fit lines that go through the origin have the form $(\tau_s)^{-1/2} = \beta\epsilon_{ext}$, where β is the gradient. The Rashba coefficient is defined in section 5.1 in terms of the electric field in the valence band $\langle\epsilon_z^v\rangle$. It is related to the actual electric field $\langle\epsilon_{ext}\rangle$ by the relation (see appendix A)

$$\langle\epsilon_z^v\rangle = \left(1 - \frac{\Sigma_v}{\Sigma_c}\right)\langle\epsilon_{ext}\rangle = 1.67\langle\epsilon_{ext}\rangle \tag{5.14}$$

where Σ_v and Σ_c are the valence and conduction band offsets. Thus $(\tau_s)^{-1/2} = \beta\langle\epsilon_z^v\rangle/1.67$. Putting this into equation 5.6 gives

$$\alpha = \frac{\hbar^2}{e}\frac{\beta}{(1.67)(2m_e k_B T\tau_p^*)^{1/2}}. \tag{5.15}$$

The calculated values as a function of temperature are shown in figure 5.8. The values incorporate the experimentally observed change in the electron effective mass with temperature[84] which nonetheless has a minor effect on the data. Although the experimental uncertainties are significant there appears to be an increase of α with temperature.

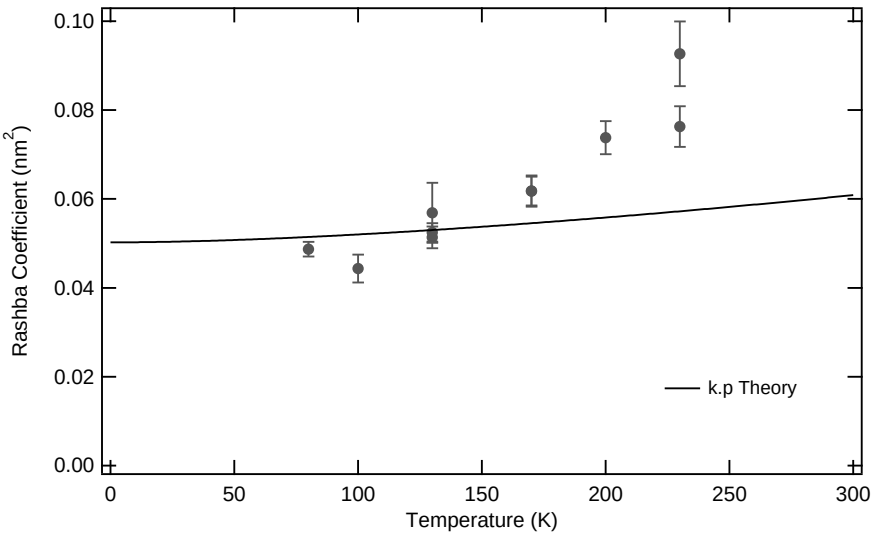

Figure 5.8: The values of the Rashba coefficient calculated by combining the electron spin relaxation and scattering time measurements. The solid line indicates the theoretical value of the coefficient given by equation 5.16.

5.4.4 Theoretical value

A theoretical value of the Rashba coefficient can by calculated using the k.p method as described in Roland Winkler's book[53]. Using eight band k.p theory the Rashba coefficient for bulk GaAs is given by

$$\alpha = \frac{P^2}{3}\left[\frac{1}{E_G^2} - \frac{1}{(E_G+\Delta_0)^2}\right] + \frac{P'^2}{3}\left[\frac{1}{(E_G-E'_G)^2} - \frac{1}{(E_G-E'_G-\Delta'_0)^2}\right] \tag{5.16}$$

where P is Kane's momentum matrix element, E_G is the band gap energy and Δ_0 is the spin-orbit energy gap for the p-bonding valence (Γ_{8v}). The primes indicate parameters for the s-antibonding (Γ_{6c}) and p-antibonding (Γ_{7c}) conduction bands. The parameters used in the calculation were those found in reference [53] combined with the temperature dependence of E_G given in reference [85]. The temperature dependence of E'_G was ignored. This should only have a very small effect as at 0 K the first term containing E_G is 50 times larger than the second containing E'_G.

The theoretical value shown by the solid black line has a slight temperature dependence owing to the variation in the band gap of GaAs with temperature. At low temperatures there is very good agreement in figure 5.8 between the theoretical (solid line) and measured (solid dots) values.

The agreement is less good at high temperatures as the experimental values show a stronger dependence on temperature than the theoretical value.

A theoretical value of the Rashba coefficient for quantum wells is derived in Winkler's book[53]. The theoretical value for the n=1 conduction band subband is similar to bulk (see appendix D), but as two-dimensional confinement removes the degeneracy of the heavy and light holes, the spin-orbit and band gap energies are replaced with the energy gap between the n=1 conduction and different subbands of the light hole and split-off bands. In addition to these terms in the denominator, optical matrix elements for subbands in the conduction, light hole valence and split-off valence bands appear in the numerator. As these terms are not known and need to be measured experimentally, the Rashba coefficient for bulk was used as an approximate theoretical value in this work. This approximation appears to be valid as there is good agreement between the theoretical line and experimental points, particularly at low temperature. Importantly, the Rashba coefficient for quantum wells should not contain any additional temperature dependence. This is because eigenenergies for different subbands do not change significantly with temperature. Any change in the energies between subbands for different electronic bands with temperature would result primarily from the change in the band gap.

5.4.5 Discussion of temperature dependence

Significant temperature dependence of the effective Landé g-factor for electrons have been observed[86, 87] and interpretation of this effect is controversial. Two different explanations based on k.p theory have been put forward.

One explanation suggested by Hubner et al.[88] was to incorporate the full measured temperature dependence of the band gap E_G in the k.p calculation and to allow the Kane's momentum matrix element P to decrease with temperature[88]. This paper presented evidence for a decrease in P^2 of 0.4% at 100 K and 1.6% at 300 K and some theoretical justification for this temperature dependence was given. However, a similar calculation for the Rashba coefficient including the temperature dependence of P^2 does not significantly improve the agreement between the experiment and theory in this case[82].

Secondly Zawadzki et al. [87] presented further measurements of the

variation and pointed out that it is only legitimate to incorporate the lattice dilation part of temperature dependence of the energy band gap into k.p calculations and they demonstrated that this reduction of the effective temperature dependence of E_G can explain all the temperature dependence of the g-factor without the need to assume a temperature dependence of P. In the case of the Rashba coefficient, incorporating a decrease in the band gap variation with temperature will not produce better agreement between theory and experiment.

Clearly the temperature variations of the g-factor and of the Rashba coefficient have different origin and it is therefore necessary to examine in detail the assumptions made in this chapter.

First assumption that should be discussed is that the mobility is independent of the perpendicular electric field. As the electric field is applied there are two effects to consider. One is the electron is pushed closer to the interface and so interface roughness will become more important, possibly causing more scattering. However, increased scattering would cause a decrease in the spin relaxation rate and an underestimation of the Rashba coefficient. Or alternately, the compression of the spatial extent of the wavefunction means that the electron is less likely to scatter with phonons. As there is a good agreement with the expected variation in the spin relaxation rate with electric field, any change in the mobility must be very small most likely too small to account for the temperature variation.

The last assumption to be considered here is that effects present at high fields such as the resonant tunnelling, the increased penetration of the electron wavefunction into the barrier material and the increase in the current do not have a significant effect on the spin relaxation rates. All of these effects are magnified at higher temperatures with an increase in the leakage current and electron wavefunctions penetrating further into the barriers as a consequence of the reduction in the effective mass with temperatures[84]. The higher leakage current suggests a greater movement of carriers in the quantum wells region that could give rise to a Hartree-like potential in the wells. The increased penetration of the wavefunction into barrier is not accounted for in the theoretical value, and could possibly alter the spin-splitting as AlGaAs will have a different Rashba coefficient.

To see if these effects could account for the measured increase in the Rashba coefficient with temperature, the spin relaxation rates above 60

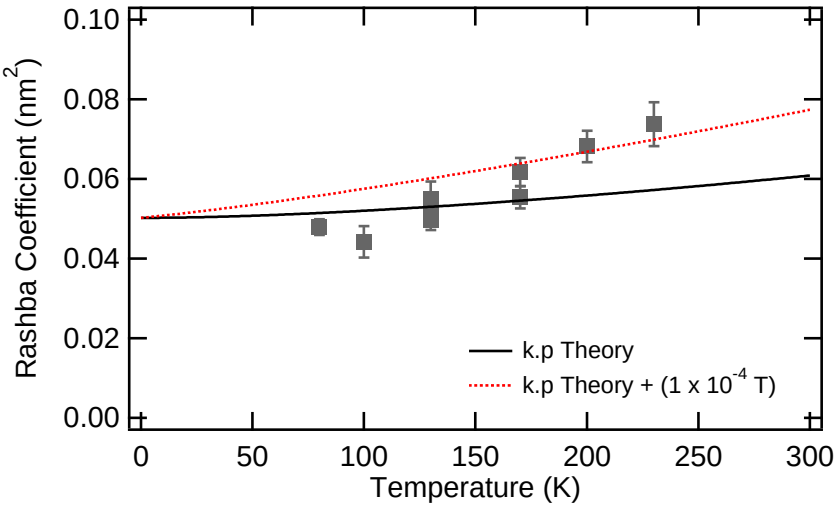

Figure 5.9: The calculated values of the Rashba coefficient using only spin relaxation times measured up to 60 kV/cm. The points still deviate from the theoretical value. The red line shows a linear dependence on temperature that fits quite well. Some data points from figure 5.8 could not be plotted on this graph as ignoring the spin relaxation rates at high field left insufficient data points for a fitting of the best fit line.

kV/cm (2 V) were ignored and the square root of the spin relaxation rate was fitted to the electric field again. Below 60 kV/cm considerably less current flows (see figure 5.4), and the electrons will spend more time in the quantum well region. The new gradients were used to calculate new values of the Rashba coefficient in figure 5.9. The data points at low temperatures are unaffected, whilst at higher temperatures there is a minor lowering of the points. This suggests that the effect of the increased current, wavefunction penetration and tunnelling on the spin dynamics is probably too small to account for the increase in the Rashba coefficient with temperature.

Another possible explanation is the influence of higher order terms in the Rashba spin-orbit interaction not previously considered in this chapter. Only recently higher order terms have been derived [89] however the sizes are unknown.

Interestingly, the red line that increases linearly with temperature in figure 5.9 fits well to the points suggesting the increase is linear with kinetic energy. This is similar to the observation made of the dependence of the Zeeman splitting on kinetic energy[90].

5.5 Conclusion

Through combining temporal and spatial spin dynamics measurements it was possible to measure the Rashba coefficient for GaAs quantum wells. There is a good agreement with k.p theory at low temperature. At higher temperatures there is a deviation from the theoretical value which seems to indicate the importance of higher order terms only recently derived and are thus usually neglected in calculation of the Rashba spin-splitting.

Chapter 6

Effect of Asymmetric Alloy Engineering

The work described in the last chapter directly demonstrated the Rashba spin-splitting for applied electric field and demonstrated that the effect is quite well described by k.p theory. It is thus now possible to predict the strength of the Rashba spin-orbit interaction for electric field. In general any asymmetry should generate a spin-splitting but no direct comparison has yet been made between asymmetry from an electric field and asymmetry from alloy engineering. Furthermore it is difficult to predict the Rashba spin-orbit interaction for alloy engineered asymmetric quantum wells. Accordingly in this chapter, electron spin dynamics are studied in alloy engineered quantum wells and by combining spin relaxation and electron scattering times it has been possible to compare the spin-splitting resulting from alloy engineering to that from an applied electric field.

6.1 Asymmetric p-i-n/n-i-p quantum well samples

The first approach in this work to obtain a comparison between built-in asymmetry and electric field was to apply an electric field to asymmetric (110) quantum wells. It was assumed that the effects of electric field and asymmetry might tend to cancel and through varying the applied field a minimum in Dyakonov-Perel spin relaxation rate would occur, thus giving a comparison of the built-in spin-splitting to that from an electric field.

In an attempt to achieve this, asymmetric (110) quantum well samples

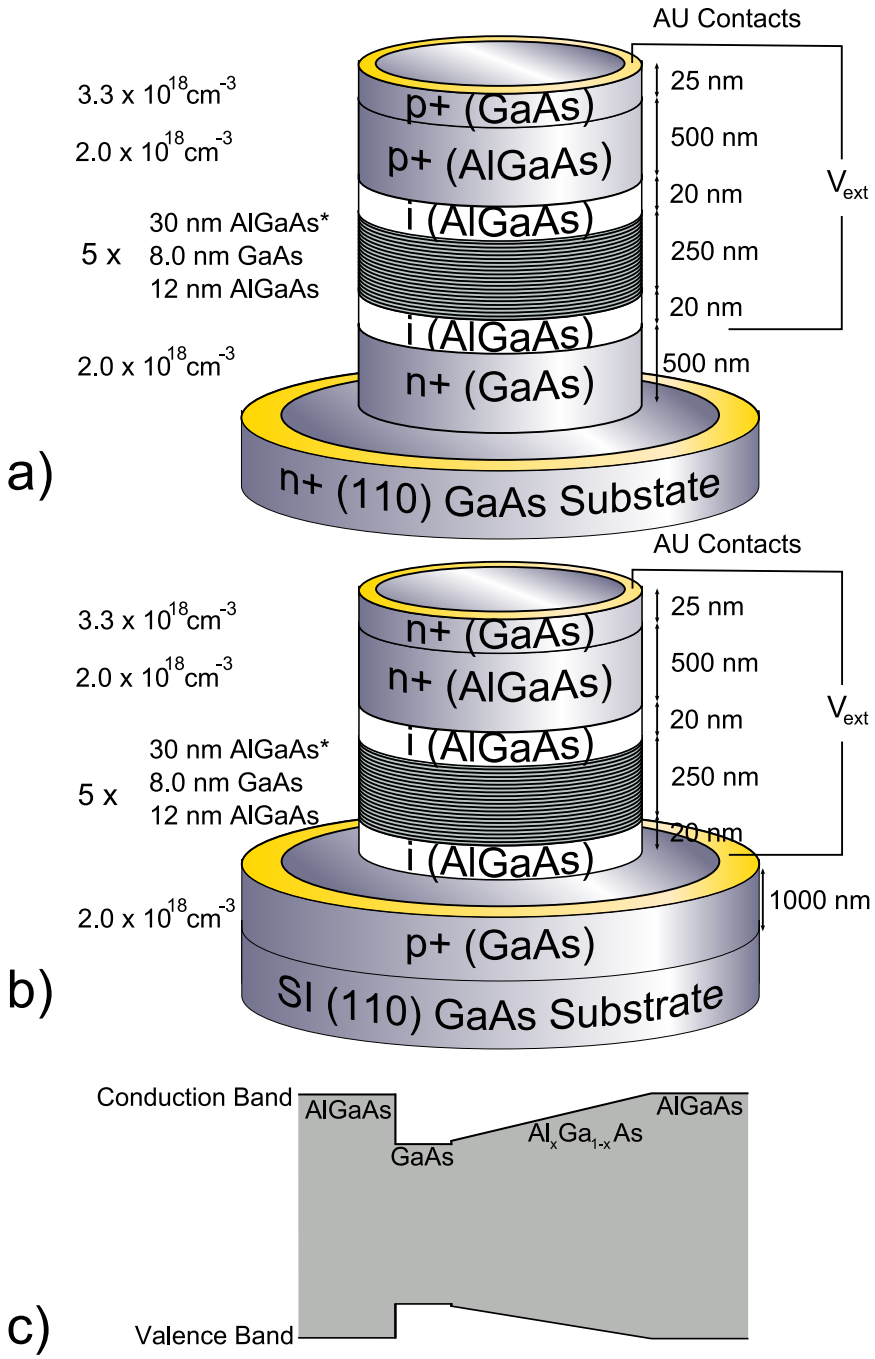

Figure 6.1: Schematics of the a) p-i-n (NU2620) and b) n-i-p (NU2621) samples studied in this chapter. AlGaAs* corresponds to a graded barrier where the aluminium fraction is increased from 0.04 to 0.4. Both samples had annular gold contacts that allowed optical access to the quantum well layers. c) A schematic of the asymmetric quantum well potential.

were grown to which electric fields could be applied (see figure 6.1). The quantum well regions comprised 5 repeats of a 12 nm $Al_{0.4}Ga_{0.6}As$ barrier, an 8 nm GaAs quantum well followed by a 30 nm $Al_xGa_{1-x}As$ layer where the aluminium fraction was varied from 0.04-0.4. The quantum wells were deposited into the intrinsic region of two separate wafers, a p-i-n (NU2620) and n-i-p (NU2621) structure that were fabricated into mesa devices with annular gold contacts on the top and contacts at the base. By using both n-i-p and p-i-n samples it was possible to apply the electric field in both directions with respect to the asymmetry.

6.1.1 Electric field

In order to convert the applied voltages to electric fields, the built-in electric field had to be calculated. As in chapter 5, the electric field is given by,

$$\epsilon_{total} = \epsilon_{built-in} - \frac{V_{ext}}{l} = \frac{\phi/e - V_{ext}}{l} \tag{6.1}$$

The doping levels in the samples were similar to NU2307 (see figure 6.1); however the thinner intrinsic region (290 nm) meant there was a greater variation in the electric field with applied bias and a larger built-in electric field (see appendix C). The built-in field for both samples were 59 kV/cm at 80 K and 55 kV/cm at 300 K.

6.1.2 I-V measurements

Current voltage measurements were taken both in the dark and under illumination from the CW output of the MIRA with power 25 μW and wavelength 822 nm (figure 6.2). Both samples displayed diode like behaviour in the dark, with minimal current in reverse bias and an exponential increase at a positive voltage. Under illumination, both samples displayed peculiar behaviour with large currents at low voltages.

For the p-i-n sample (figure 6.2a) even under a positive bias there was a large current that increased at more negative voltages. The electric field in this sample will push holes towards the graded interface and electrons towards the abrupt. It therefore appears that with only the built-in electric field holes were able to overcome the graded barrier and migrate towards the p-doped AlGaAs layer and that this tendency increases in reverse bias.

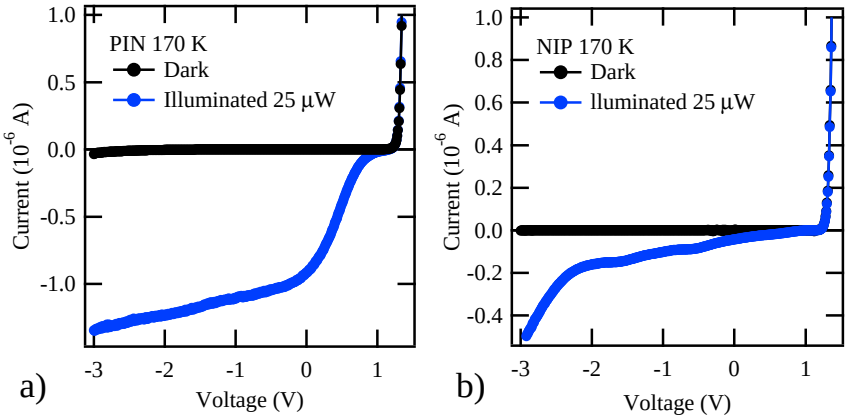

Figure 6.2: Current voltage measurements at 170 K for the MESA devices studied in this chapter from the a) p-i-n (NU2620) and b) n-i-p (NU2621) samples. In the dark both samples have diode like behaviour, whilst under illumination of 25 μW both samples show poor carrier retention. There is a distinct difference in the measurements for the different samples suggesting different causes for the large currents.

For the n-i-p sample (figure 6.2b), the electric field will push electrons towards the graded barriers and holes towards the abrupt. For this sample the increase in the current with reverse bias was more gradual. A more gradual onset of current from electrons overcoming the graded barrier is expected as the conduction band discontinuity is larger than that in the valence band.

These currents are comparable to that seen in chapter 5 for the symmetric quantum well p-i-n device, however with around 20 times less optical power. For these asymmetric quantum wells under 25 μW of illumination, a current of 1 μA corresponds to around 40% of the injected carriers being spilled out of the wells. Such a large current would complicate spin dynamics measurements as there are few carriers to contribute to the $\Delta\theta$ and ΔR signals and carrier escape represents an additional decay channel for the signals. These carriers are also likely to create complications in the calculation of the electric field as the non-uniform charge distribution would give rise to a Hartree potential.

As NU2621 demonstrated better confinement of the carriers to the quantum wells layers, it was investigated further but at only 100 K to further reduce the number of photoexcited carriers that escape the wells.

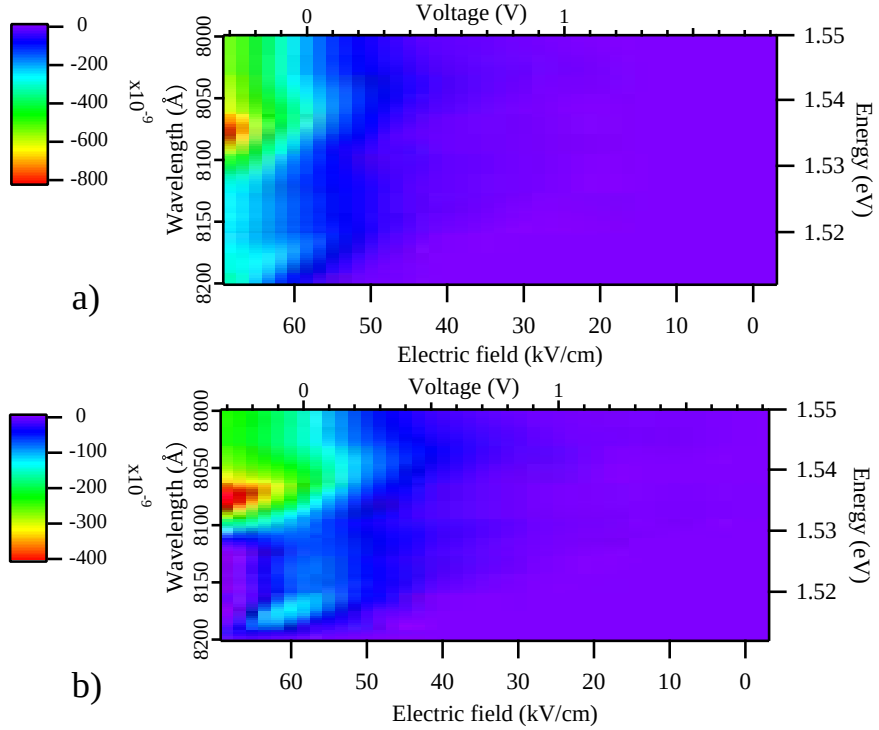

Figure 6.3: a) The current whilst illuminated with 500 μW of light as a function of both illumination wavelength and electric field at 100 K b) As above but with the measurement taken at 8200 Å treated as a background and therefore subtracted from the other data.

6.1.3 Wavelength I-V

Figure 6.3a shows the shows the variation in the current under 500 μW of illumination as a function of both electric field and wavelength for NU2621 at 100 K. At high fields there is a region of high current around 8080 Å and a second region around 8180 Å. These become better defined when the current recorded at the longest wavelength (8200 Å) is subtracted from the other measurements (figure 6.3b). The thick barriers in the sample $30 + 12 = 42$ nm (see figure 6.1) meant that tunnelling between wells is extremely unlikely, so these areas of high current are most likely the spilling of carriers from two different quantum well states. Both of the high current regions shift to longer wavelengths with increasing electric field consistent with the quantum confined Stark effect.

6.1.4 Spin measurements

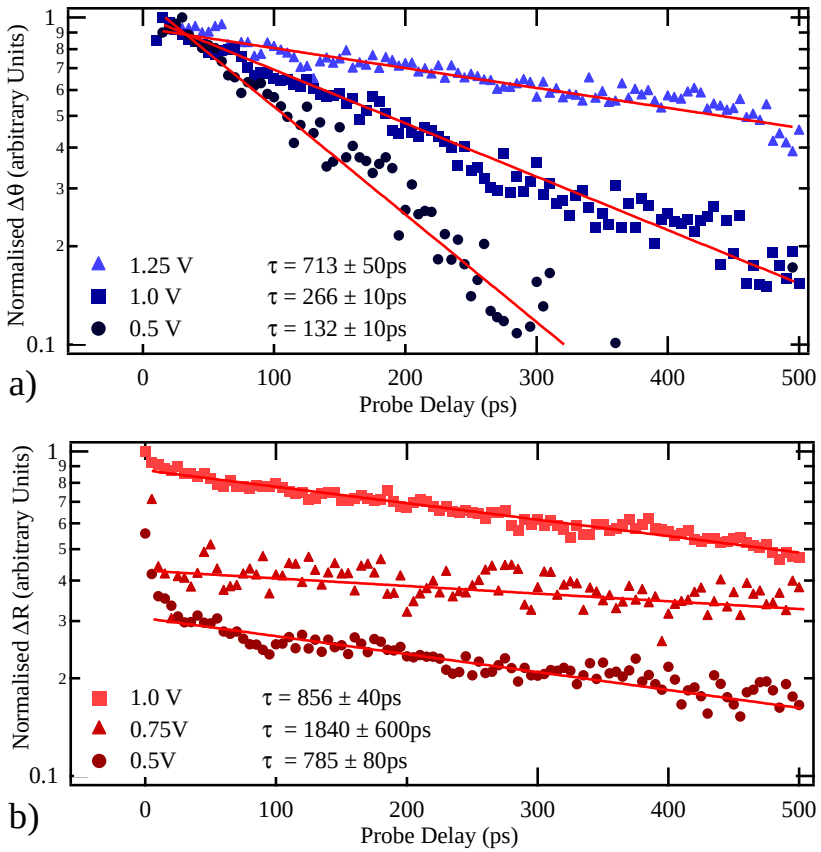

Figure 6.4: Measurements on NU2621 at 100 K. a) $\Delta\theta$ time-resolved for different values of voltage. b) ΔR time-resolved for different voltages.

Spin dynamics measurements were carried out on NU2621 at 100 K. Once the variation of the $\Delta\theta$ and ΔR with wavelength were determined for each voltage, time-resolved measurements were taken for a few wavelengths at each voltage. A selection of the measurements is shown in figure 6.4. As these measurements are taken in forward bias, where the applied voltage reduces the built-in electric field, larger values of voltage correspond to smaller values of electric field. There is a decrease in the decay times of the $\Delta\theta$ measurements with decreasing voltage (increasing electric field), consistent with observations in chapter 5. ΔR measurements generally decayed on a shorter time scale than in the symmetric quantum wells, consistent with

the observation of the poor carrier retention of the wells. In this asymmetric sample the decay times of the $\Delta\theta$ and ΔR signals were closer than in the symmetric sample of chapter 5. The similar decay times result in larger uncertainties in the calculation of the spin lifetime.

6.1.5 Electric field correction

With measurements of the current at different wavelengths and electric fields it should be possible to check the calibration of the applied voltage to electric field. The white circles in figure 6.5 are wavelengths at which the peak in the

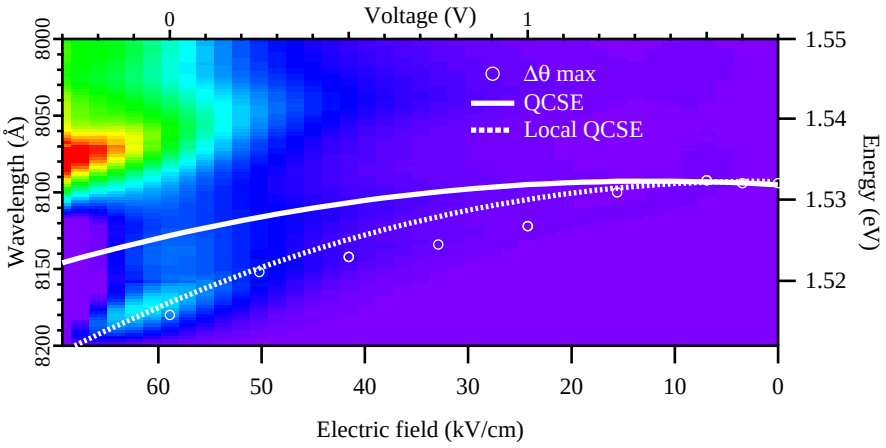

Figure 6.5: A comparison of where the $\Delta\theta$ peaks occurred (white circles) to the current recorded at 100 K. The solid white line is the calculated QCSE for asymmetric quantum wells. White dotted line is the electric field used for each voltage.

$\Delta\theta$ were located for different electric fields. These wavelengths agree well with the wavelength at which the lower energy peak current was observed. It appears that this current is from the n=1 heavy hole to conduction band transition and corresponds to electrons escaping from the n=1 level. As can been seen by the non-parabolic change in the white circles with electric field, the positions of the $\Delta\theta$ peaks are complicated by the change in absorption (see also section 5.3.1). However the position of the peak of the $\Delta\theta$ at low fields and the position of the peak current at high fields can be used to estimate the shift in the n=1 heavy hole to conduction band transition with electric field. The shift in energy with electric field can then be used as a measure of the actual electric field present.

As one cannot assume that optical transitions in asymmetric quantum wells would have the same shift to longer wavelengths with electric fields as symmetric quantum wells, the optical transitions under an electric field for this sample were calculated by Tim Liew from the University of Southampton.

Using the transfer matrix method to calculate the solutions to the Schrödinger equation in the asymmetric potential under an applied electric field[91], it was possible to calculate the quantum confined Stark effect for the asymmetric quantum wells. Assuming the n=1 heavy hole to conduction band transition matches the white circles at low fields, the solid white line in figure 6.5 shows the calculated shift with electric field. The calculated shift in energy for the asymmetric quantum wells is again parabolic. However, the parabola is not centred at zero electric field as for symmetric quantum wells, but instead at around 10 kV/cm.

As the solid white line does not coincide with the area of high current at around 70 kV/cm, it is likely the non-uniform distribution of carriers increases the electric field in the quantum wells. Assuming the transfer matrix calculation was correct, the electric field was scaled up to give a better agreement with the current at high fields. The electric field given by the dashed white line was used instead of the solid white line as a calibration of the electric field as a function of voltage.

6.1.6 Comparison with NU2307

Using the calibrated electric field from above it is possible to compare the effect of an electric field on spin dynamics in the asymmetric quantum wells (NU2621) with the symmetric quantum wells from chapter 5 (NU2307). Figure 6.6 shows the spin relaxation rate variation with electric field for both NU2307 and NU2621 at 100 K. The spin relaxation rates for NU2621 have considerably larger error bars as the measurements contained more noise. There is no distinct minimum in the spin relaxation rate with applied field. The points at $\sim$ 10 kV/cm and at $\sim$ 67 kV/cm are unreliable as they respectively correspond to voltages where the current is beginning to exponentially increase and where there is a large reverse current (see below). A linear fit to the remaining points (dashed blue line) that passes through the origin gives a good representation of the data. Assuming the built-in spin-splitting is independent of electric field, the spin precession vector can

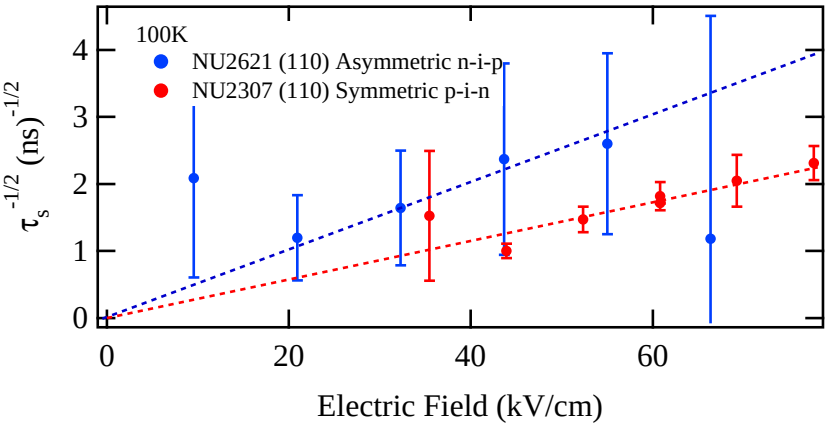

Figure 6.6: Square root of the spin relaxation rate against electric field for both NU2307 and NU2621 at 100 K.

be written

$$\mathbf{\Omega_{SIA}} = \frac{e}{\hbar}\left(\alpha\langle\epsilon_z^v\rangle + \eta\right)\begin{pmatrix} k_y \\ -k_x \\ 0 \end{pmatrix} \tag{6.2}$$

where η is a constant that represents the spin-splitting from the alloy engineering. For a thermalised population this would give a square root of the spin relaxation rate of the form

$$\left(\frac{1}{\tau_s}\right)^{1/2} = \frac{e}{\hbar}(\alpha\langle\epsilon_z^v\rangle + \eta)\left(\frac{2m_e k_B T}{\hbar^2}\right)^{1/2}(\tau_p^*)^{1/2} \tag{6.3}$$

The best fit line in the figure, aside from the points at either end, appears to go through the origin suggesting any built-in spin-splitting very small. The deviation from the line at low fields is not unexpected, as at this electric field the device is starting to exhibit an exponential increase in the current. The presence of these extra charges will complicate the electric field seen by the carriers. Then at high fields the signal becomes very small as there are fewer carriers in the quantum well and the graded barrier would allow the electron and hole wavefunction overlap and hence oscillator strength to reduce more than in symmetric quantum wells. The reduction in the signal is reflected in the large error bars at around 65 kV/cm.

It is worth noting that the large error bars for the measurements taken on NU2621 does mean that a built-in spin-splitting equivalent to an electric

field around 10 kV/cm cannot be ruled out. But even with this taken into account, the presence of the built-in asymmetry appears to have very little effect on the spin dynamics of electrons in the quantum wells.

6.2 Undoped asymmetric quantum wells

Results from the previous section show that a graded interface in the presence of an electric field leads to poor carrier confinement. To circumvent this problem, spin dynamics were studied in undoped wells with a graded interface in the absence of an electric field and comparison was made with symmetric wells.

Four samples were studied (figure 6.7), two symmetric quantum wells grown on both (100) NU2281 and (110)-oriented substrates NU2284, and two asymmetric quantum wells grown on both (100) NU2662 and (110)-oriented substrates NU2654. Spin dynamics were measured at different wavelengths and temperatures for all four samples. As the asymmetric samples only contained 5 quantum wells, the signals were correspondingly small. As (110) quantum wells show power dependence of the spin relaxation rate [16, 25], the excitation power was set as low as possible (pump 800 μW) at room temperature and was kept constant for measurements taken at lower temperatures.

6.2.1 Mobilities

Transient spin grating measurements were carried out on the four samples by Will Leyland and Jonathan Mar from Cambridge University. By combining these measurements with the spin relaxation measurements (section 6.2.2), it was possible to calculate the mobilities in the two (110) samples (figure 6.8)[1]. Both samples show a decrease in the mobility with temperature that is close to (temperature)$^{-1}$ indicating that the electron mobilities are limited by phonon scattering [83]. The solid red line shows the best fit of an inverse temperature fit that was used to give smoothed mobilities for the two samples. Comparison with figure 5.7 shows that the mobility of these samples is very similar to that of sample NU2307.

[1]Unfortunately, the presence of the BIA precession vector in the quantum well plane complicates spin diffusion in (100) quantum wells [92]. Consequently the mobility cannot be determined by the combination of the spin relaxation and spin grating measurements.

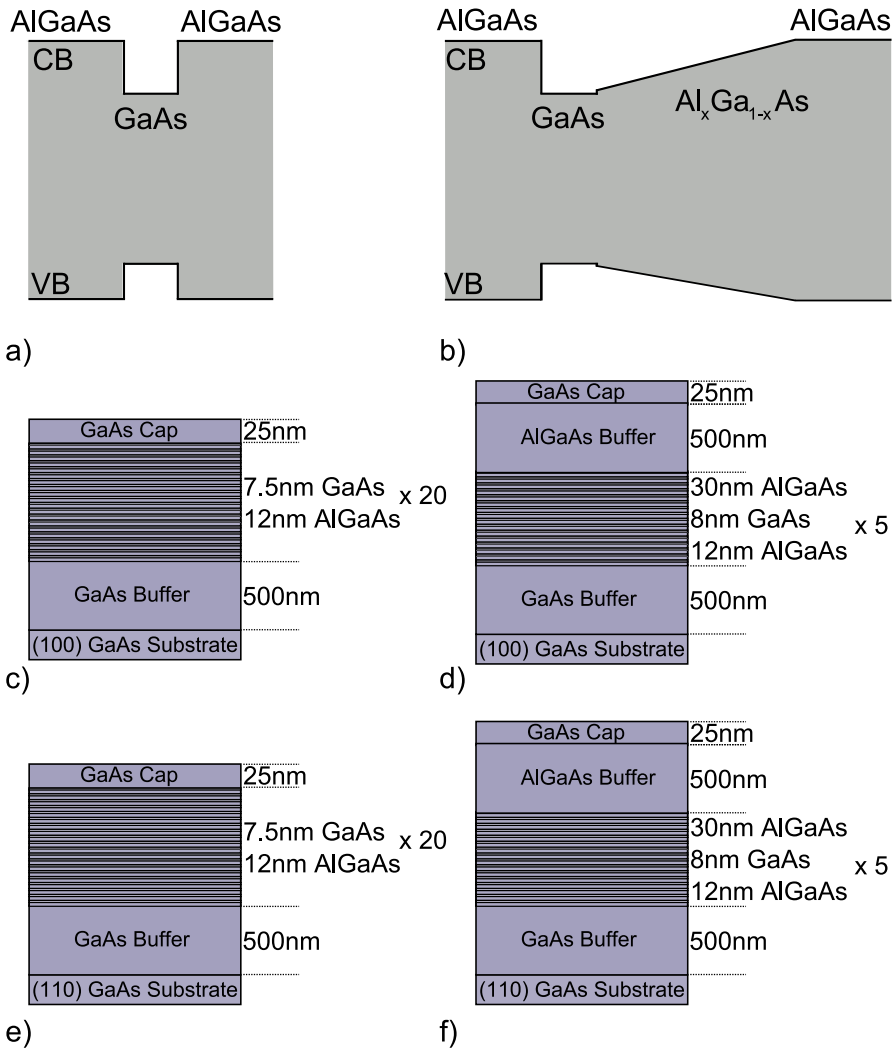

Figure 6.7: Potentials of the a) symmetric and the b) asymmetric QWs studied. The structures of the c) symmetric (100) quantum well sample NU2281, d) asymmetric (100) quantum well sample NU2662, e) symmetric (110) quantum well sample (NU2284) and f) asymmetric (110) quantum well sample (NU2654).

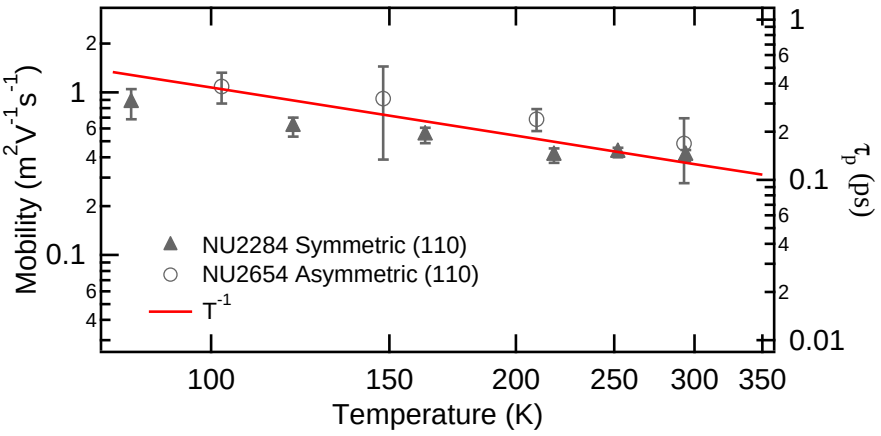

Figure 6.8: The calculated mobilities and electron scattering times for the asymmetric (open circles) and the symmetric (solid triangles) (110) quantum wells. The solid line represents the expected change for a two dimensional system with a constant density of states.

6.2.2 Spin lifetime measurements

Figure 6.9a shows the time-resolved $\Delta\theta$ measurements for the four different samples at 200 K. The decay of the $\Delta\theta$ signals for the two (100) samples are shorter consistent with the fact that (100) quantum wells have a component of the BIA effective magnetic field perpendicular to spin alignment that can cause Dyakonov-Perel spin relaxation. For both the (100) and the (110) asymmetric samples have the longer $\Delta\theta$ decay times. This is a first indication that the presence of the graded interface does not induce additional spin-splitting and corresponding spin relaxation.

The ΔR measurements are shown at 200 K in figure 6.9b. The measured decay times for each sample are around 5 times longer than the $\Delta\theta$ decay times measured. Therefore, the calculated spin lifetimes will not differ greatly from the $\Delta\theta$ decay times measured in 6.9b.

6.2.3 Spin relaxation rates

Measurements were taken at different wavelengths and temperatures for all four samples. The weighted mean of the spin lifetime measurements ($\bar{\tau_s}$) taken at different wavelengths was calculated for each sample at a particular

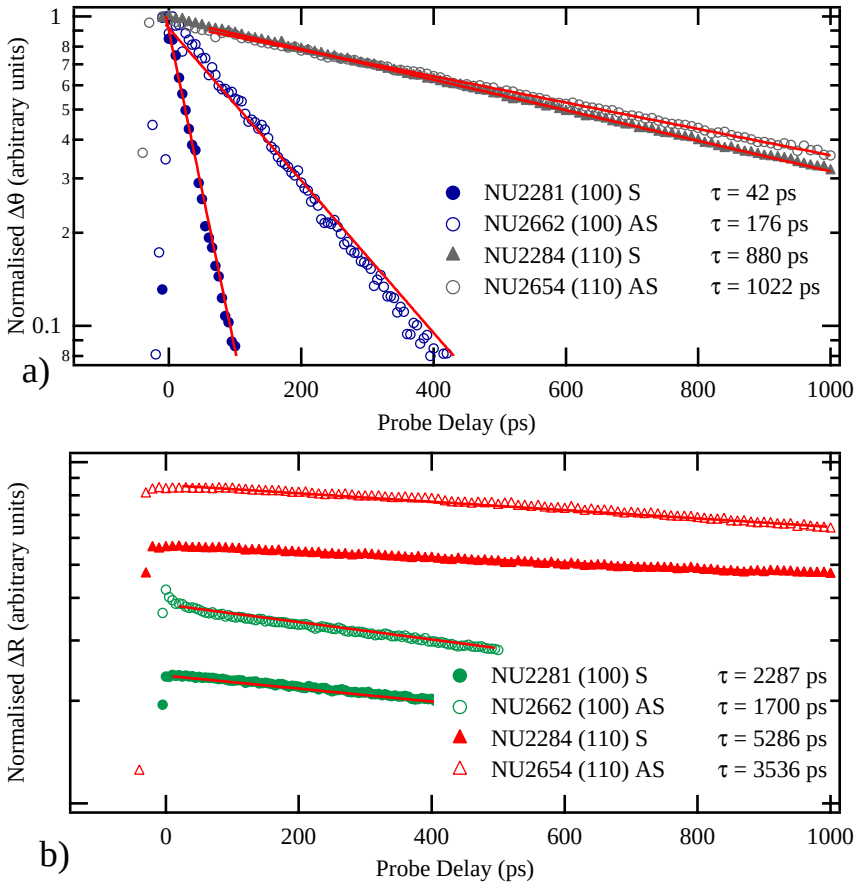

Figure 6.9: a) Time-resolved measurements of the $\Delta\theta$ and ΔR for the four different samples at 200 K. Where S and AS refer to symmetric and asymmetric alloy composition respectively.

temperature using

$$\bar{\tau_s} = \frac{\sum_{i=1}^{n} \left(\frac{1}{\delta\tau_s}\right)_i^2 (\tau_s)_i}{\sum_{i=1}^{n} \left(\frac{1}{\delta\tau_s}\right)_i^2} \tag{6.4}$$

where $\delta\tau_s$ corresponds to the error in the spin relaxation rate. The results for the different samples are shown in figure 6.10a. Across all temperatures the spin relaxation rates determined for the asymmetric quantum wells were smaller than the rates determined for the symmetric quantum wells.

As the spin relaxation rate is proportional to the confinement energy

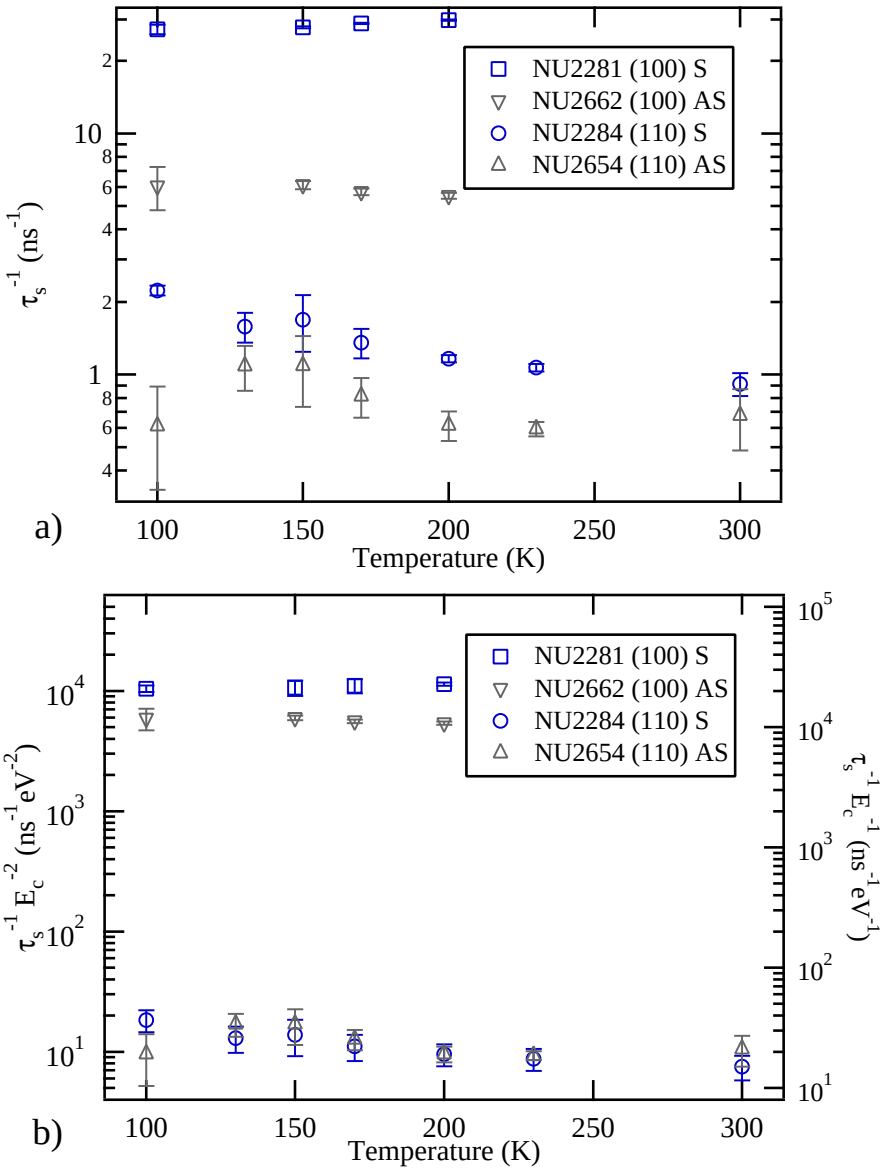

Figure 6.10: a) The measured spin relaxation rates for the four different samples at different temperatures. b) The spin relaxation rates normalised by confinement energy ((110) quantum wells) and confinement energy squared ((100) quantum wells) to compensate for known variations in the spin relaxation times with quantum well width. (S and AS correspond to symmetric and asymmetric alloy variations respectively.)

squared for (100) quantum wells[36] and has been observed to scale with the confinement energy in (110) quantum wells [16], the spin relaxation rates may be scaled accordingly and the points should lie on a mutual curve for each substrate orientation. Figure 6.10b is a plot of the spin-relaxation rate normalised by the confinement energy squared for the (100) quantum wells and the confinement energy for the (110) quantum wells. This normalisation brings the data for the (110) quantum wells to an agreement. For the (100) quantum wells, the agreement isn't as good, however, the normalised spin relaxation rate is still smaller in the asymmetric quantum well.

As the mobilities in the (110)-oriented samples (NU2284 and NU2654) have been measured to be similar, the coincidence of the points in figure 6.10b supports the conclusion from the measurements on the n-i-p and p-i-n devices that any built-in spin-splitting from the asymmetry is very small. So small that the actual spin relaxation mechanism in (110) quantum wells [16] is always dominant over any SIA induced Dyakonov-Perel spin relaxation.

As the BIA effective magnetic field does not contribute to spin relaxation in (110) quantum wells, it is possible to combine the measurements of the spin relaxation rate with electron scattering time measurements to determine the SIA spin-splitting for the (110) samples.

6.2.4 Spin splittings

The measurements of the electron scattering time were combined with the spin relaxation rates to determine the spin-splitting that would produce the measured spin relaxation rates on the assumption of Dyakonov-Perel spin relaxation. The results are shown in figure 6.11. Values for NU2284 (open blue squares) and NU2654 (solid grey squares) are essentially the same. For the symmetric quantum well the values are upper limits of the spin-splitting as there is no Dyakonov-Perel spin relaxation for spin aligned normal to the quantum well and observed relaxation is due to some other mechanism. The measured upper limit is larger than that measured for NU2654, so the presence of the asymmetry clearly does not produce a measureable spin-splitting. The average spin-splitting in NU2654 is less than the upper limit in a symmetric quantum well as a result of the different confinement energies of the two samples, as shown in section 6.2.3.

To demonstrate the effect of an electric field on the spin-splitting in a quantum well, the spin-splitting calculated for NU2307 at both the built-in

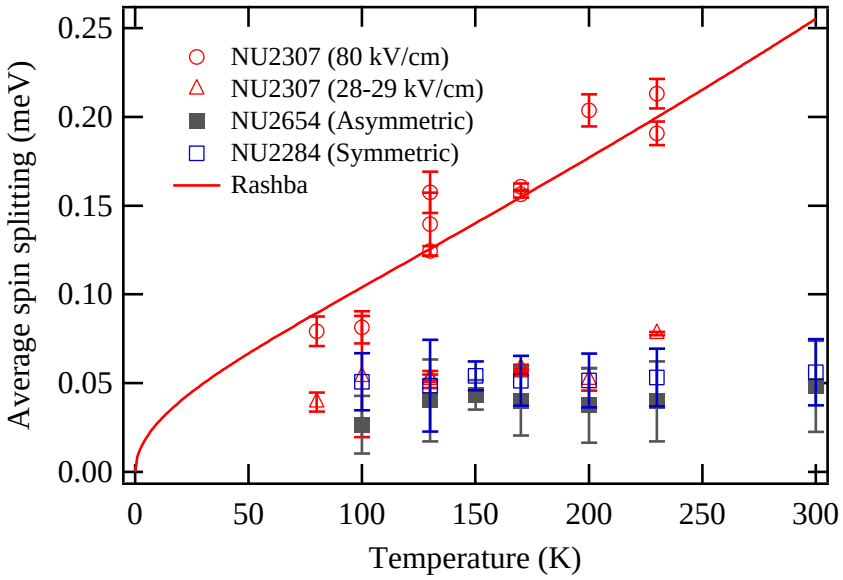

Figure 6.11: The calculated spin splitting for (110) quantum wells. The solid grey squares are those measured in the asymmetric quantum well, whilst the blue open squares are those measured in a symmetric (110) quantum well. The open triangles are the spin-splitting calculated at the built-in field for NU2307. The open circles are the spin-splittings measured at 80 kV/cm in NU2307 and the red line is the calculated spin splitting calculated at 80 kV/cm using the value of the Rashba coefficient measured in chapter 5.

field (27-28 kV/cm) and 80 kV/cm are plotted in figure 6.11. The coincidence of the points measured at the built-in field with the two other (110) samples suggest that the spin lifetimes in this sample are not limited by Dyakonov-Perel spin relaxation. The spin-splittings measured at 80 kV/cm are clearly larger than those measured in the asymmetric quantum wells. There is an increase in the spin-splitting with temperature as higher momentum states are occupied.

The clear conclusion from the data in figure 6.11 is that the asymmetry built into sample NU2654 induces almost no spin-splitting in comparison with that induced by an electric field of 80 kV/cm. This is despite of the fact that the potential gradient represented by the alloy gradient is equivalent to $\sim$ 100 kV/cm.

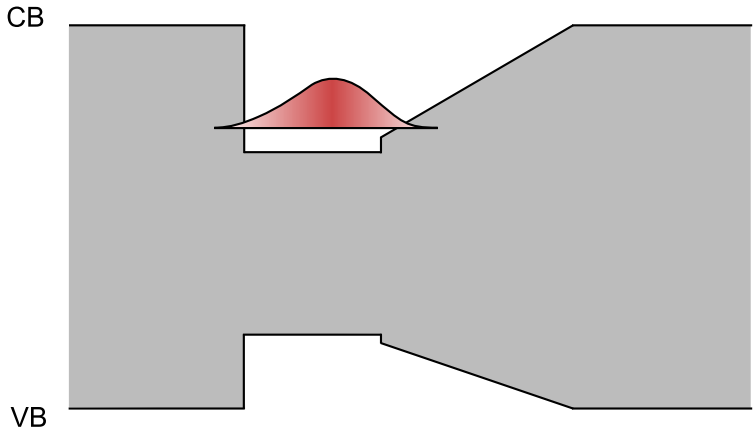

Figure 6.12: A schematic of the asymmetric quantum wells potential profile studied for both the conduction (CB) and valence bands (VB). The shaded red area is a schematic of the n=1 electron wavefunction within the envelope function approximation.

6.2.5 Interpretation

The observation that asymmetric quantum wells without an electric field do not produce measureable spin-splittings can be understood within the envelope function approximation covered in Winkler[53]. An important aspect is the difference between the valence and conduction band electric fields.

For undoped quantum wells, the conduction band electric field (ϵ_z^c) can be broken down into contributions from the conduction band edge potential (V_z^c) and an externally applied field (ϵ_{ext}) giving

$$\epsilon_z^c = \epsilon_{ext} + \frac{1}{e}\frac{\partial}{\partial z}V_z^c. \tag{6.5}$$

For the case of the quantum wells with asymmetric alloy composition (figure 6.12), ϵ_{ext} is zero and the expectation value of the electric field for the conduction band state $|\psi_c\rangle$ is given by

$$\langle\psi_c|\,\frac{1}{e}\frac{\partial}{\partial z}V_z^c\,|\psi_c\rangle = 0. \tag{6.6}$$

So in order to satisfy Ehrenfest's theorem (equation 2.11), the contribu-

tion to the electric field from the first abrupt interface must be equal to the contribution from the graded interface. The electron wavefunction adjusts so that the expectation value of the electric field is zero.

The expectation value of the valence band electric field $\langle \epsilon_z^v \rangle$ for conduction electrons in the asymmetric quantum well potential in figure 6.12 is not required to be zero and is similarly given by

$$\langle \epsilon_z^v \rangle = \langle \psi_c | \frac{1}{e} \frac{\partial}{\partial z} V_z^v | \psi_c \rangle \tag{6.7}$$

where V_z^v is the valence band edge potential. For AlGaAs/GaAs quantum wells, the conduction band edge potential is related to the valence band edge potential by

$$\langle \psi_c | \frac{1}{e} \frac{\partial}{\partial z} V_z^v | \psi_c \rangle = -\frac{\Sigma_v}{\Sigma_c} \langle \psi_c | \frac{1}{e} \frac{\partial}{\partial z} V_z^c | \psi_c \rangle \tag{6.8}$$

where Σ_c, Σ_v are the conduction and valence band offsets respectively. Now combining equations 6.8 and 6.7 for the asymmetry potential shown in figure 6.12 we get

$$\langle \epsilon_z^v \rangle = -\frac{\Sigma_v}{\Sigma_c} \langle \psi_c | \frac{1}{e} \frac{\partial}{\partial z} V_z^c | \psi_c \rangle \,. \tag{6.9}$$

That is the expectation value of the valence band electric field is proportional to the expectation value of the conduction band. As the expectation value of the conduction band is zero, to first order the expectation value of the valence band electric field and therefore the Rashba spin-splitting is zero. Higher order terms give rise to only a very small valence band electric field that would give rise to a spin splitting smaller than the upper limit measured in symmetric (110) quantum wells.

To produce a measureable spin-splitting requires that the conduction and valence bands are not just related to each other by a scalar constant. This is because the expectation value of the conduction band electric field has to be zero and therefore any scaled field experienced by the conduction electrons will also be zero. One way to produce a non-zero valence band electric field is to apply an external electric field (as shown in chapter 5). Now the electric field is non-zero and is given by (see appendix A)

$$\langle \epsilon_z^v \rangle = (1.67) \langle \epsilon_{ext} \rangle. \tag{6.10}$$

Doping quantum wells can produce a non-uniform distribution of charge and hence a Hartree potential. Therefore the electric field can be external or internal. Another means to produce a measureable Rashba spin-splitting is to use material systems where equation 6.8 does not hold, for example in quaternary alloy systems such as aluminium indium gallium arsenide (AlInGaAs)[93, 94].

Although these results agree with the theoretical predictions of Winkler [53], there is an apparent contradiction to the results obtained by Averkiev et al [19], who measured a ratio of the BIA to the SIA in (100) quantum wells similar to NU2662, but with slightly smaller barrier heights. Measuring a ratio of 1 : 4, they assumed that the SIA was bigger. It is likely that the ratio they measured was in fact the SIA to the BIA. The long spin lifetimes measured in NU2662 in comparison to NU2281 suggest the BIA effective field is reduced as the asymmetric wells have a smaller confinement energy (see equation 2.13). This suggests a small SIA effective magnetic field and spin-splitting. However, the measurement of a ratio suggests a larger SIA type effective magnetic field than that measured in this work. This is because even in (110) quantum wells, where BIA spin relaxation is suppressed, the effect of the asymmetry on spin relaxation was not detectable.

One possible explanation for this is the presence of strain. When samples are mounted into a cryostat at room temperature and then cooled it is quite possible that the sample becomes exerted to shear strain. In order to minimise the effect of strain in the work presented in this thesis, the samples were mounted onto samples sticks with polytetrafluoroethylene (PTFE) tape. The use of the tape would prevent unequal thermal contractions in the sample mount and the quantum well sample from producing strain.

For (100) quantum wells, in the presence of strain, there is a strain induced effective magnetic field of the form[95],

$$\mathbf{\Omega_{STR}} = C_3 \epsilon_{xy} \begin{pmatrix} -k_y \\ k_x \\ 0 \end{pmatrix} \tag{6.11}$$

where C_3 is a constant and ϵ_{xy} corresponds to an in-plane shear strain. It can be seen that strain in a (100) quantum well produces an effective magnetic field that has the same form as the SIA effective magnetic field. It is possible it was a combination of the SIA and STR effective magnetic

fields that Averkiev et al. measured.

6.2.6 Conclusion

By studying spin dynamics in quantum wells with one abrupt and one graded interface, it was possible to examine the influence of the inversion asymmetry of the potential on the conduction band spin splitting. The time-resolved measurements in a (110) n-i-p structure hinted that any spin-splitting from the asymmetry of the band-edge potential profile must be very small. Then measurements of spin relaxation rate in asymmetric (100) and (110) quantum wells demonstrated that the spin relaxation rate is smaller than that in similar, but symmetric quantum wells.

When the spin relaxation rates in (110) quantum wells were combined with electron scattering time measurements to get the spin-splittings, the measured spin splittings for the asymmetric potential was no larger than that found in a symmetric quantum well which was itself an upper limit. These results agree with a theoretical treatment that takes into consideration the effect of both the conduction and valence bands in the calculation of the Rashba spin-splitting.

Therefore to produce measureable changes in electron spin lifetimes through the Rashba spin-orbit interaction requires either an electric field, built-in or applied or a quaternary alloy system.

Chapter 7

Conclusion

This thesis has presented optical studies of non-equilibrium electron spin dynamics in GaAs quantum wells in the presence of asymmetry. Most of the work focused on (110) quantum wells as these allow a study of the Rashba spin-orbit interaction without influence of the bulk inversion asymmetry effective magnetic field.

As the growth axis of (110) quantum wells have lower rotational symmetry than the growth axis in (100) quantum wells, the time-resolved Kerr rotation technique used to study electron spin dynamics had to be modified to accurately measure electron spin lifetimes normal to the plane. The effect of the lower symmetry could be compensated for by taking measurements with both opposite circular polarisations of the pump that were then combined.

Utilising the insensitivity to the bulk inversion asymmetric effective magnetic field for spin aligned normal to the plane in (110) quantum wells, the first measurement of the Rashba coefficient was obtained. There was good agreement with k.p theory at low temperatures but with increasing temperature there was a deviation from the theoretical value. The most likely cause is the influence of higher order terms of the Rashba spin-orbit interaction, only recently calculated[89].

The study of spin dynamics in quantum wells with one abrupt and one graded interface have highlighted the importance of producing valence and conduction bands that are different by more than a scalar constant to induce a measurable spin-splitting. For quantum wells with asymmetric potential profiles but 'congruent' conduction and valence bands, spin-splittings that

are allowed by pure symmetry arguments, will be very small and uninfluential to electron spin dynamics.

7.1 Future work

Following the work in chapter 4, it would be interesting to see if other systems that possess lower symmetry have similar effects on the reflected probe beam in the time-resolved Kerr rotation technique.

As semiconductor heterostructures grown on (100) with no common atom have reduced symmetry (C_{2v}) from that of standard (100) quantum wells (D_{2d}), they possess optical linear anisotropy[96]. The effect of the reduced symmetry on spin dynamics has been investigated [97] but not on the time-resolved Kerr rotation technique. Therefore, as (110) quantum wells possess the same symmetry (C_{2v}), the technique developed in this work should allow accurate optical measurements of spin dynamics in no common atom quantum well systems.

Following a measurement of the Rashba coefficient in chapter 5, the effect of electric fields on spin dynamics are becoming better understood. The next step would be to investigate the effect of electric fields on spin dynamics in (111) quantum wells. One approach would be to grow p-i-n and n-i-p devices with quantum wells embedded in the intrinsic region. This would allow the application of an electric field in both directions ensuring the cancellation of the BIA and SIA terms for all electron momenta.

There was an attempt to grow such samples during the course of this work; however the PL from the unprocessed samples displayed very broad PL indicating poor carrier confinement. This suggests further optimisation of the growth conditions are needed to obtain better quality (111) samples. An aspect not taken into account whilst measuring the PL was the presence of the large piezoelectric effect present in (111) quantum wells that can produce electric field of around 100 kV/cm [98] normal to the quantum well plane. The samples were mounted to the closed-cycle cryostat using silver paint that could induce strain at low temperatures and combined with the built-in electric field from the doping, could result in poor carrier confinement.

The large piezoelectric field normal to the quantum well plane that is not present in (100) or (110) quantum wells [99], could be used in engineering

latticed mismatched quantum wells with adequate strain-induced electric field to compensate for the BIA. The measurement of the Rashba coefficient will help with the estimation of the size of the electric field and hence lattice mismatch necessary. Furthermore, the temperature dependence of the relative sizes of the two effective magnetic fields could provide further support for the influence of higher order terms in the SIA effective magnetic field not usually considered.

The results in chapter 6 were on quantum wells where the asymmetry was in the barrier. An investigation in the effect of a grade in the quantum well would be the next logical step. Effects of quaternary alloy systems should also be investigated, as a large spin splitting should be producible.

This also highlights the importance of experimental observations; something that is allowed by symmetry doesn't necessarily have a large (or easily measurable) effect. Other interesting effects have been proposed by further breaking of asymmetry. One that has not been reported experimentally is the control of electron spin relaxation in quantum wells using strain. Strain can produce spin-relaxation by producing a spin-splitting[14] in the conduction band of GaAs. The form of the effective magnetic fields is the same as the SIA for (100) quantum wells, whilst in (110) quantum wells it has the same form as BIA[95]. So for (110) quantum wells under strain, there is the possibility of a total suppression of Dyakonov-Perel spin relaxation for all electron momenta.

Appendix A

Valence band electric field

The difference between conduction and valence band electric fields can be understood within the theoretical framework covered in Winkler's book[53] based on the envelope function approximation (EFA).

For undoped quantum wells, the conduction band electric field (ϵ_z^c) can be broken down into contributions from the conduction band edge potential (V_z^c) and an externally applied field (ϵ_{ext}) giving

$$\epsilon_z^c = \epsilon_{ext} + \frac{1}{e}\frac{\partial}{\partial z}V_z^c. \tag{A.1}$$

Figure A.1 shows a schematic of the profile of a quantum well under an externally applied electric field and the wavefunction of an electron within the EFA. The contribution to the electric field from the first interface will be greater than that from the second interface. This negative contribution to the electric field will be equal to combined positive contributions from the second interface and the gradient in the quantum well region. This would result in an expectation value of the electric field that is zero, thus satisfying Ehrenfest's theorem that for a stationary state the net force on the state must be zero. Taking the expectation value of equation A.1 one obtains,

$$\langle\psi_c|\,\epsilon_{ext}\,|\psi_c\rangle = -\,\langle\psi_c|\,\frac{1}{e}\frac{\partial}{\partial z}V_z^c\,|\psi_c\rangle \tag{A.2}$$

where ψ_c is the electron wavefunction in the conduction band. So in order to satisfy Ehrenfest's theorem in the presence of an electric field, the spatial distribution of the electron wavefunction changes so as to feel no net force.

In a similar manner to above, the expectation value of the valence band

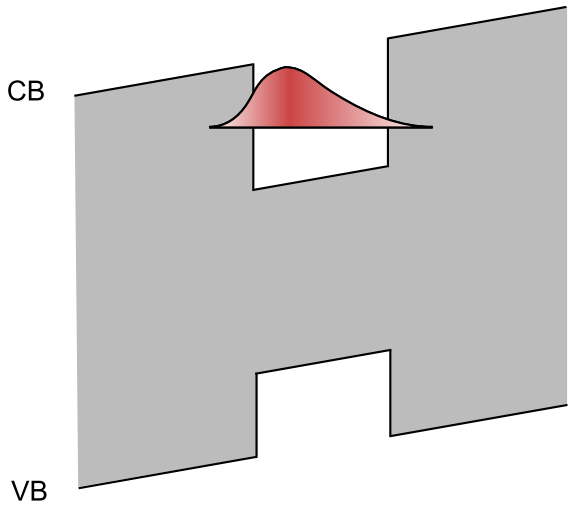

Figure A.1: A schematic of a quantum well potential profile under the influence of an electric field and the first bound state of an electron.

electric field, which isn't required to be zero, is given by

$$\langle \epsilon_z^v \rangle = \langle \psi_c | \, \epsilon_{ext} \, | \psi_c \rangle + \langle \psi_c | \, \frac{1}{e} \frac{\partial}{\partial z} V_z^v \, | \psi_c \rangle \tag{A.3}$$

For a conduction band offset of Σ_c and a valence band offset of Σ_v, we are able to write

$$\langle \psi_c | \, \frac{1}{e} \frac{\partial}{\partial z} V_z^v \, | \psi_c \rangle = -\frac{\Sigma_v}{\Sigma_c} \langle \psi_c | \, \frac{1}{e} \frac{\partial}{\partial z} V_z^c \, | \psi_c \rangle \tag{A.4}$$

Putting this all together, one obtains an expectation value of the valence band given by

$$\langle \epsilon_z^v \rangle = \langle \psi_c | \, \epsilon_{ext} \, | \psi_c \rangle - \frac{\Sigma_v}{\Sigma_c} \langle \psi_c | \, \frac{1}{e} \frac{\partial}{\partial z} V_z^c \, | \psi_c \rangle = \left(1 - \frac{\Sigma_v}{\Sigma_c} \right) \langle \epsilon_{ext} \rangle \tag{A.5}$$

The ratio of the conduction to valence band discontinuities is 0.67 [100], using this we obtain the following equation for the valence band electric field

$$\langle \epsilon_z^v \rangle = (1.67) \langle \epsilon_{ext} \rangle. \tag{A.6}$$

Appendix B

Rashba coefficient units

The experimentally determined Rashba coefficient was calculated using the following equation from chapter 5

$$\alpha = \frac{\hbar^2}{e\langle\epsilon_z^v\rangle}\frac{1}{(2m_e k_B T\tau_p^*\tau_s)^{1/2}} \tag{B.1}$$

Using standard SI units gives

$$\frac{(J.s)^2}{C(V/m)}\frac{1}{(kg(JK^{-1})Ks^2)^{1/2}} = \frac{J^2sm}{CV}\frac{1}{(kgJ)^{1/2}}. \tag{B.2}$$

Using the equivalence of a volt to a Joule per Coulomb (C=JV^{-1}) and the Joule to m^{2}kgs^{-2}

$$\frac{J^2sm}{(JV^{-1})V}\frac{1}{(kgJ)^{1/2}} = \frac{Jsm}{(kgJ)^{1/2}} = \frac{(m^2kgs^{-2})sm}{(kg(m^2kgs^{-2}))^{1/2}} = m^2. \tag{B.3}$$

Therefore the Rashba coefficient has units of length squared.

Appendix C

Built-in electric field

C.1 NU2307

A schematic of the energy levels in the NU2307 for degenerate p and n regions used in the calculation of the built in electric field. At low tem-

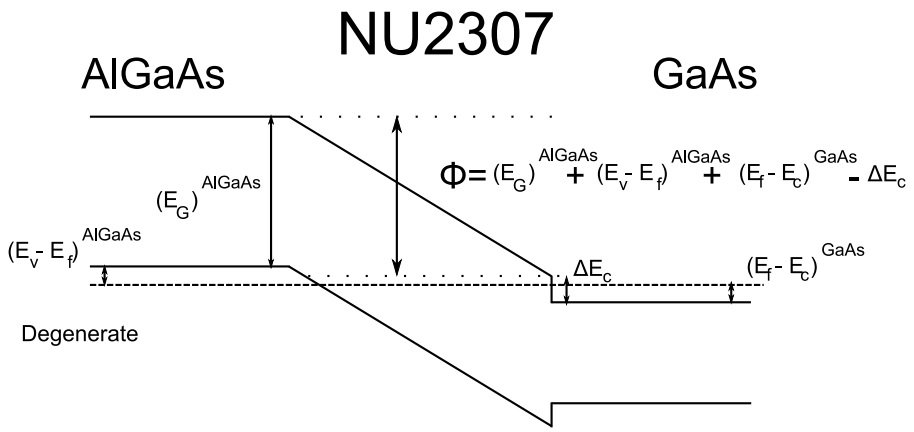

Figure C.1: Built-in electric field for NU2307.

peratures both the n and the p regions are degenerate. Whilst at higher temperatures the p-region becomes non-degenerate. The equation for determination of the Fermi energy in degenerate semiconductors was still used, as determining the Fermi energy for a non-degenerate semiconductor has little effect on the built-in electric field

C.2 NU2621

Schematic of the band edges and Fermi level for NU2621 for in the p^+ GaAs and n^+ AlGaAs used in the calculation of the built in electric field. The

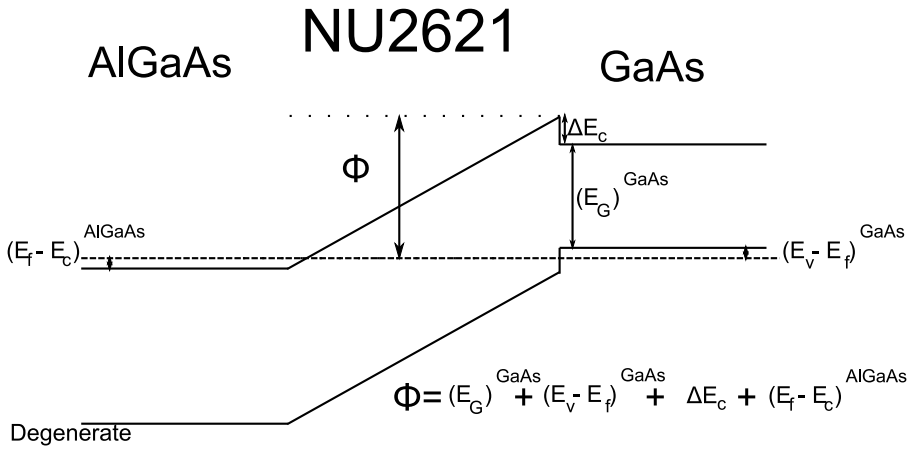

Figure C.2: Built-in electric field for NU2307.

electric field for sample NU2620 can be calculated using a similar equation.

Appendix D

Rashba coefficient for quantum wells

In Winkler[53], the Rashba coefficient for quantum wells using 8×8 subband k.p method is given by

$$\begin{aligned}\alpha =&\frac{2ieP^2}{3}\left[\sum_{\beta}\frac{\langle c_\alpha|\, z\,|l_\beta\rangle\,\langle l_\beta|\, k_z\,|c_\alpha\rangle-\langle c_\alpha|\, k\,|l_\beta\rangle\,\langle l_\beta|\, k_z\,|c_\alpha\rangle}{(E^c_\alpha-E^l_\alpha)(E^c_\alpha-E^l_\beta)}\right.\\&\left.-\sum_{\beta}\frac{\langle c_\alpha|\, k_z\,|l_\beta\rangle\,\langle l_\beta|\, k\,|c_\alpha\rangle-\langle c_\alpha|\, k_z\,|l_\beta\rangle\,\langle l_\beta|\, k\,|c_\alpha\rangle}{(E^c_\alpha-E^l_\alpha)(E^c_\alpha-E^l_\beta)}\right]\end{aligned}\tag{D.1}$$

where P is Kane's momentum matrix element, α,β are subband indices, $|c_\alpha\rangle, |l_\alpha\rangle, |s_\alpha\rangle$ are the conduction, light-hole and split-off band states with energies $E^c_\alpha, E^l_\alpha, E^s_\alpha$.

Bibliography

[1] G. Lampel, Physical Review Letters **20**, 491 (1968).

[2] G. Schmidt, D. Ferrand, L. W. Molenkamp, A. T. Filip, and B. J. van Wees, Physical Review B **62**, R4790 (2000).

[3] M. Wang *et al.*, Applied Physics Letters **93**, 132103 (2008).

[4] S. Datta and B. Das, Applied Physics Letters **56**, 665 (1990).

[5] Y. Acremann *et al.*, Applied Physics Letters **93**, 102513 (2008).

[6] Y. Nishikawa, A. Tackeuchi, S. Nakamura, S. Muto, and N. Yokoyama, Applied Physics Letters **66**, 839 (1995).

[7] D. D. Awschalom, D. Loss, and N. Samarth, *Semiconductor Spintronics and Quantum Computation*, NanoScience and Technology Vol. 5 (Springer, Berlin, 2002).

[8] I. Appelbaum, B. Q. Huang, and D. J. Monsma, Nature **447**, 295 (2007).

[9] A. M. Tyryshkin, S. A. Lyon, A. V. Astashkin, and A. M. Raitsimring, Physical Review B **68**, 193207 (2003).

[10] A. M. Tyryshkin, S. A. Lyon, W. Jantsch, and F. Schaffler, Physical Review Letters **94**, 126802 (2005).

[11] B. Huang, D. J. Monsma, and I. Appelbaum, Physical Review Letters **99**, 177209 (2007).

[12] A. Malinowski *et al.*, Physical Review B **62**, 13034 (2000).

[13] Y. A. Bychkov and E. I. Rashba, Journal of Physics C-Solid State Physics **17**, 6039 (1984).

[14] G. E. Pikus, V. A. Marushchak, and A. N. Titkov, Soviet Physics, Semiconductors **22**, 115 (1988).

[15] T. Adachi, Y. Ohno, F. Matsukura, and H. Ohno, Physica E-Low-Dimensional Systems and Nanostructures **10**, 36 (2001).

[16] Y. Ohno, R. Terauchi, T. Adachi, F. Matsukura, and H. Ohno, Physical Review Letters **83**, 4196 (1999).

[17] S. D. Ganichev *et al.*, Nature **417**, 153 (2002).

[18] Y. K. Kato, R. C. Myers, A. C. Gossard, and D. D. Awschalom, Science **306**, 1910 (2004).

[19] N. S. Averkiev *et al.*, Physical Review B **74**, 033305 (2006).

[20] W. J. H. Leyland *et al.*, Physical Review B **76**, 033305 (2007).

[21] V. V. Bel'kov *et al.*, Physical Review Letters **100**, 176806 (2008).

[22] S. D. Ganichev *et al.*, Physical Review Letters **92**, 256601 (2004).

[23] L. Meier *et al.*, Nature Physics **3**, 650 (2007).

[24] G. M. Muller *et al.*, Physical Review Letters **101**, 206601 (2008).

[25] O. Z. Karimov *et al.*, Physical Review Letters **91**, 246601 (2003).

[26] W. J. H. Leyland *et al.*, Physical Review B **75**, 165309 (2007).

[27] L. Brillouin, *Wave Propagation in Periodic Structures*, 2nd ed. (Dover, New York, 1963).

[28] D. D. Sell, Physical Review B **6**, 3750 (1972).

[29] D. G. C. Jones, *Atomic physics*Physics and its applications (Chapman and Hall, London, 1997).

[30] R. P. Feynman, R. B. Leighton, and M. Sands, *The Feynman lectures on physics* (Addison-Wesley, Reading, MA, 1963).

[31] O. Madelung, *Semiconductors*, Landolt-Bornstein, New Series III Vol. 17a (Springer, Berlin, 1982).

[32] G. Dresselhaus, Physical Review **100**, 580 (1955).

[33] M. I. Dyakonov and V. I. Perel, Soviet Physics, Solid State **13**, 3023 (1972).

[34] M. I. Dyakonov and V. I. Perel, Soviet Physics, JETP **33**, 1053 (1971).

[35] M. I. Dyakonov and V. I. Perel, Jetp Letters-Ussr **13**, 467 (1971).

[36] M. I. Dyakonov and V. I. Perel, Theory of optical spin orientation of electrons and nuclei in semiconductors, in *Optical Orientation*, edited by F. Meier and B. Zakharchenya, , Modern Problems in Condensed Matter Sciences Vol. 8, pp. 11–72, North-Holland Physics Publishing, Amsterdam, (1984).

[37] F. Meier and B. Zakharchenya, *Optical Orientation*, Modern Problems in Condensed Matter Science Vol. 8 (North-Holland Physics Publishing, Amsterdam, 1984).

[38] D. J. Hilton and C. L. Tang, Physical Review Letters **89**, 146601 (2002).

[39] G. L. Bir, A. G. Aronov, and G. E. Pikus, Zhurnal Eksperimentalnoi I Teoreticheskoi Fiziki **69**, 1382 (1975).

[40] G. L. Bir, A. G. Aronov, and G. E. Pikus, Soviet Physics, JETP **42**, 705 (1976).

[41] R. J. Elliott, Physical Review **96**, 266 (1954).

[42] Y. Yafet, Solid State Physics **14**, 1 (1963).

[43] M. A. Brand *et al.*, Physical Review Letters **89**, 236601 (2002).

[44] F. Bloch, Zeitschrift fr Physik A Hadrons and Nuclei **52**, 555 (1929).

[45] G. Bastard, *Wave mechanics applied to semiconductor heterostructures*Monograpies de Physique (Les Editions de Physique, Les Ulis, 1988).

[46] C. Weisbuch and B. Vinter, *Quantum semiconductor structures, Fundamentals and applications* (Academic Press, INC., San Diego, USA, 1991).

[47] B. Baylac *et al.*, Solid State Communications **93**, 57 (1995).

[48] J. Zhou and M. W. Wu, Physical Review B **77**, 075318 (2008).

[49] E. Ivchenko, *Optical Spectroscopy of Semiconductor Nanostructures* (Alpha Science International Ltd, Harrow, UK, 2005).

[50] N. S. Averkiev and L. E. Golub, Physical Review B **60**, 15582 (1999).

[51] X. Cartoixa, D. Z. Y. Ting, and Y. C. Chang, Physical Review B **71**, 045313 (2005).

[52] M. Flatt, J. M. Byers, and W. H. Lau, Chapter 4, in *Semiconductor Spintronics and Quantum Computation*, edited by D. D. Awschalom, D. Loss, and N. Samarth, Springer, Berlin, (2002).

[53] R. Winkler, *Spin-orbit Coupling Effects in Two-Dimensional Electron and Hole Systems*, Springer Tracts in Modern Physics Vol. 191 (Springer, Berlin, 2003).

[54] J. J. Sakurai, *Modern Quantum Mechanics*, Revised ed. (Addison-Wesley, Redwood City, 1994).

[55] A. Darr, T. Kotthaus, and T. Ando, Electron-spin resonance in an inversion layer on InSb, in *13th International Conference on the Physics of Semiconductors, Rome, Italy*, edited by F. Fumi, p. 774, North-Holland, (1976).

[56] R. Lassnig, Physical Review B **31**, 8076 (1985).

[57] R. Winkler, Physica E-Low-Dimensional Systems and Nanostructures **22**, 450 (2004).

[58] M. I. Dyakonov and V. Y. Kachorovskii, Soviet Physics, Semiconductors **20**, 110 (1986).

[59] R. S. Britton *et al.*, Applied Physics Letters **73**, 2140 (1998).

[60] N. S. Averkiev, L. E. Golub, and M. Willander, Journal of Physics-Condensed Matter **14**, R271 (2002).

[61] E. I. Rashba, Soviet Physics, Solid State **2**, 1109 (1960).

[62] Y. Varshni, Physica **34**, 149 (1967).

[63] N. I. Zheludev *et al.*, Solid State Communications **89**, 823 (1994).

[64] Y. K. Kato, R. C. Myers, A. C. Gossard, and D. D. Awschalom, Physical Review Letters **93**, 4 (2004).

[65] M. J. Snelling, P. Perozzo, D. C. Hutchings, I. Galbraith, and A. Miller, Physical Review B **49**, 17160 (1994).

[66] R. E. Worsley, N. J. Traynor, T. Grevatt, and R. T. Harley, Physical Review Letters **76**, 3224 (1996).

[67] W. J. H. Leyland, *Spin Transport and Relaxation in Semiconductor Heterostructures, Cambridge University*, PhD thesis, (2007).

[68] A. R. Cameron, P. Riblet, and A. Miller, Physical Review Letters **76**, 4793 (1996).

[69] J. J. Baumberg, D. D. Awschalom, N. Samarth, H. Luo, and J. K. Furdyna, Physical Review Letters **72**, 717 (1994).

[70] U. Schmid, N. E. Christensen, M. Cardona, F. Lukes, and K. Ploog, Physical Review B **45**, 3546 (1992).

[71] D. Gershoni *et al.*, Physical Review B **44**, 1930 (1991).

[72] S. M. Sze and K. N. Kwok, *Physics of Semiconductor Devices*, 3rd ed. (John Wiley and Sons, Hoboken, New Jersey, USA, 2006).

[73] J. Nitta, T. Akazaki, H. Takayanagi, and T. Enoki, Physical Review Letters **78**, 1335 (1997).

[74] S. Dohrmann *et al.*, Physical Review Letters **93**, 147405 (2004).

[75] M. Fox, *Optical Properties of Solids* (Oxford University Press, Oxford, 2001).

[76] D. A. B. Miller *et al.*, Applied Physics Letters **41**, 679 (1982).

[77] G. Bastard, E. E. Mendez, L. L. Chang, and L. Esaki, Physical Review B **28**, 3241 (1983).

[78] D. A. B. Miller *et al.*, Physical Review Letters **53**, 2173 (1984).

[79] D. A. B. Miller *et al.*, Physical Review B **32**, 1043 (1985).

[80] D. C. Hutchings, M. Sheikbahae, D. J. Hagan, and E. W. Vanstryland, Optical and Quantum Electronics **24**, 1 (1992).

[81] K. Lai and J. C. Campbell, Ieee Journal of Quantum Electronics **30**, 108 (1994).

[82] P. S. Eldridge *et al.*, Physical Review B **77**, 125344 (2008).

[83] J. M. Ziman, Chapter 10, in *Electrons and Phonons*, Oxford University Press, New York, (1972).

[84] I. Vurgaftman, J. R. Meyer, and L. R. Ram-Mohan, Journal of Applied Physics **89**, 5815 (2001).

[85] D. E. Aspnes, Physical Review B **14**, 5331 (1976).

[86] M. Oestreich *et al.*, Physical Review B **53**, 7911 (1996).

[87] W. Zawadzki *et al.*, Physical Review B **78**, 245203 (2008).

[88] J. Hubner, S. Dohrmann, D. Hagele, and M. Oestreich, Physical Review B **79**, 193307 (2009).

[89] X. Cartoixa, L. W. Wang, D. Z. Y. Ting, and Y. C. Chang, Physical Review B **73**, 205341 (2006).

[90] M. A. Hopkins *et al.*, Semiconductor Science and Technology **2**, 568 (1987).

[91] B. Jonsson and S. T. Eng, IEEE Journal of Quantum Electronics **26**, 2025 (1990).

[92] C. P. Weber *et al.*, Physical Review Letters **98**, 076604 (2007).

[93] D. Olego, T. Y. Chang, E. Silberg, E. A. Caridi, and A. Pinczuk, Applied Physics Letters **41**, 476 (1982).

[94] J. R. Jensen, J. M. Hvam, and W. Langbein, Journal of Applied Physics **86**, 2584 (1999).

[95] S. W. Chang and S. L. Chuang, Physical Review B **72**, 115429 (2005).

[96] O. Krebs and P. Voisin, Physical Review Letters **77**, 1829 (1996).

[97] K. C. Hall *et al.*, Physical Review B **68**, 115311 (2003).

[98] D. L. Smith, Solid State Communications **57**, 919 (1986).

[99] D. L. Smith, Piezoelectric effects in strained layer heterostructures grown on novel index substrates, in *2nd International Workshop on Growth, Characterization and Exploitation of Epitaxial Compound Semiconductor on Novel Index Surfaces (NIS 96)*, pp. 707–715, Lyon, France, (1996), Elsevier Advanced Technology.

[100] J. Batey, S. L. Wright, and D. J. Dimaria, Journal of Applied Physics **57**, 484 (1985).